1993

Phase Transitions and Flux Distributions of SU(2) Lattice Gauge Theory.

Yingcai Peng
Louisiana State University and Agricultural & Mechanical College

INFORMATION TO USERS

This manuscript has been reproduced from the microfilm master. UMI films the text directly from the original or copy submitted. Thus, some thesis and dissertation copies are in typewriter face, while others may be from any type of computer printer.

The quality of this reproduction is dependent upon the quality of the copy submitted. Broken or indistinct print, colored or poor quality illustrations and photographs, print bleedthrough, substandard margins, and improper alignment can adversely affect reproduction.

In the unlikely event that the author did not send UMI a complete manuscript and there are missing pages, these will be noted. Also, if unauthorized copyright material had to be removed, a note will indicate the deletion.

Oversize materials (e.g., maps, drawings, charts) are reproduced by sectioning the original, beginning at the upper left-hand corner and continuing from left to right in equal sections with small overlaps. Each original is also photographed in one exposure and is included in reduced form at the back of the book.

Photographs included in the original manuscript have been reproduced xerographically in this copy. Higher quality 6" x 9" black and white photographic prints are available for any photographs or illustrations appearing in this copy for an additional charge. Contact UMI directly to order.

U·M·I

University Microfilms International
A Bell & Howell Information Company
300 North Zeeb Road, Ann Arbor, MI 48106-1346 USA
313/761-4700 800/521-0600

Order Number 9405415

Phase transitions and flux distributions of $SU(2)$ lattice gauge theory

Peng, Yingcai, Ph.D.

The Louisiana State University and Agricultural and Mechanical Col., 1993

U·M·I
300 N. Zeeb Rd.
Ann Arbor, MI 48106

PHASE TRANSITIONS AND FLUX DISTRIBUTIONS OF $SU(2)$ LATTICE GAUGE THEORY

A Dissertation

Submitted to the Graduate Faculty of the
Louisiana State University and
Agricultural and Mechanical College
in partial fulfillment of the
requirements for the degree of
Doctor of Philosophy

in

The Department of Physics and Astronomy

by
Yingcai Peng
B.S., Tsinghua University, Beijing, 1986
M.S., Louisiana State University, 1987
August 1993

ACKNOWLEDGEMENTS

I am indebted to my advisor, Professor Richard W. Haymaker for his continuous patient advisory and valuable guidance during my dissertation research. Without his helps this work would not have been possible. I am also happy to thank Profs. A.R.P. Rau, J. Callaway, W. Metcalf, L.H. Chan and D. Koester for their introducing me atomic physics, solid state physics, high energy physics, field theory and general relativity theory.

It is a pleasure to thank Drs. H. Chen, V. Singh, C.H. Lee, L. Zhang and K. Yee, and my friends H. Zheng, X. Zhang, C. Bahri, V. Poduri, J. Vijapurkar, L. Bi for many helps and interesting discussions. I am grateful to Prof. R.W. Haymaker and the Physics Department for the financial support. I also want to extend my appreciations to all members of the Department for their kindness and helps throughout my graduate study period.

Finally I want to thank Monika Lee and Hortensia T. Valdes for their many helps in using computing facilities. This dissertation was also supported in part by the U.S. Department of Energy.

TABLE OF CONTENTS

PAGE

ACKNOWLEDGEMENTS ii

LIST OF TABLES v

LIST OF FIGURES vii

ABSTRACT xi

CHAPTER

1 INTRODUCTION 1

2 LATTICE GAUGE THEORY BASICS 14

2.1 Introduction of LGT 14

2.2 Interpretation of Some Physical Quantities 20

2.3 The Scaling Relation $a(\beta)$ Of $SU(2)$ LGT 23

2.4 Transfer Matrix and Temperatures on Lattices 25

3 CALCULATION METHODS AND NUMERICAL RESULTS 29

3.1 Calculation Methods of LGT 29

3.2 Numerical Results 31

4 FINITE TEMPERATURE PHASE TRANSITION 39

4.1 Basic Theory 39

4.2 Data Analysis 43

5 FLUX DISTRIBUTIONS 53

5.1 Motivations 53

5.2 Flux Distributions at Finite Temperatures 57

5.3 Implementation to Finite Volumes 69

6 MICHAEL SUM RULES AND FINITE SIZE EFFECTS 74

6.1 Review and Generalizations of Michael Sum Rules 74
6.2 Analysis of Flux Data 86
SUMMARY 93
REFERENCES 95
APPENDICES
A MONTE CARLO METHODS IN LGT 98
A.1 Metropolis Algorithm 99
A.2 Heat Bath Algorithm 104
A.3 Over-Relaxation Algorithm 104
B PROOF OF A RELATION 110
VITA 112

LIST OF TABLES

TABLE		PAGE
1	The correspondence of the lattice spacing a and the coupling constant β for the $SU(2)$ LGT.	25
2	The statistics of data on the lattice $4 \cdot 11^2 \cdot 65$.	32
3	The measured values of $< \|P\| >$ on lattices $4 \cdot 9^2 \cdot 65$, $4 \cdot 11^2 \cdot 65$, $6 \cdot 7^2 \cdot 65$ and $6 \cdot 11^2 \cdot 37$.	33
4	The raw string tension data κ extracted from the correlation $< P(0)P^{\dagger}(z) >_c$ at different distance z, they were measured on the lattice $4 \cdot 11^2 \cdot 65$ with $\beta = 2.25$.	34
5	The string tension data κ measured in lattice units on lattices of the size $4 \cdot 9^2 \cdot 65$, $4 \cdot 11^2 \cdot 65$, $6 \cdot 7^2 \cdot 65$ and $6 \cdot 11^2 \cdot 37$.	35
6	The string tension data κ measured in physical units on lattices of the size $4 \cdot 9^2 \cdot 65$, $4 \cdot 11^2 \cdot 65$, $6 \cdot 7^2 \cdot 65$ and $6 \cdot 11^2 \cdot 37$.	48
7	The typical measured flux density values (errors) of ρ_E and ρ_A in the region of $\beta > \beta_c$ on the edges of the transverse plane midway between the $q\bar{q}$, as shown in Fig. 5.2. The flux data are in the physical unit Gev/fm^3.	60
8	The correspondence of the two parameters z_g and z_κ.	70
9	The values of the string tension data and z_κ on lattices of size $4 \cdot N_s^2 \cdot 64$ with N_s =4, 6, 8 and $\beta = 2.36$, 2.38 and 2.41. The data are quoted from ref.[18].	71

10 Our string tension data κ and the values of the z_κ parameter on lattices of the size $4 \cdot N_s^2 \cdot 65$ with N_s =5, 7, 9, 11 and $\beta = 2.25$ and 2.28. 72

11 The center slice flux energies and action of a $q\bar{q}$ pair at various separations r/a in the confined phase, which were calculated from the flux data on the lattice $4 \cdot 11^2 \cdot 65$ with $\beta = 2.25$ ($\beta_c \approx 2.30$). The data are in the physical unit Gev/fm. 88

12 The comparison of the predictions of generalized Michael sum rules and the data of center slice action σ_A. 89

13 The σ_A data in the unconfined phase ($\beta < \beta_c$), which were measured on lattices, $4 \cdot 9^2 \cdot 65$ and $4 \cdot 11^2 \cdot 65$. The data are in the physical unit Gev/fm..... 92

LIST OF FIGURES

FIGURE		PAGE
1	(a) Screening of electric charge as a consequence of vacuum polarisation of QED. (b) Antiscreening of color charge as a consequence of vacuum polarisation of QCD.	7
2	The conjectured $q\bar{q}$ flux distribution in the confined phase, which has the string-like flux tube form.	9
3	The properties of QCD can be shown diagrammally by the 'phase diagram' on the plane of T and $1/V$.	12
4	(a). The link variable U_μ; (b). The plaquette variable U_P	17
5	(a) The Wilson loop W on the z-t plane, (b) The Polyakov loop P along the time direction.	22
6	Monte Carlo data for $< \|P\| >$ vs. β, calculated from lattices of size $4 \cdot 9^2 \cdot 65$ (circles), $4 \cdot 11^2 \cdot 65$ (squares), $6 \cdot 7^2 \cdot 65$ (triangles) and $6 \cdot 11^2 \cdot 37$ (diamonds).	44
7	Monte Carlo data of $< P(0)P(r) >$ vs. r/a in the confined phase, calculated on the lattice of size $4 \cdot 11^2 \cdot 65$ with $\beta = 2.25$ (squares), $\beta = 2.28$ (triangles) and $\beta = 2.29$ (diamonds). (a). linear axies, (b). logarithmic y axes and linear x axes.	46
8	Monte Carlo data of $< P(0)P(r) >$ vs. r in the unconfined phase, calculated on the lattice $4 \cdot 9^2 \cdot 65$ with $\beta = 2.36$ (squares) and $\beta = 2.40$ (triangles). (a). linear axies, (b). logarithmic y axes and linear x axes.	47

9 The plot of κ vs. T near the transition point T_c. The data were calculated on lattices, $4 \cdot 9^2 \cdot 65$ (circles), $4 \cdot 11^2 \cdot 65$ (squares) and $6 \cdot 7^2 \cdot 65$ (triangles). The solid line is the fitting function in Eq. (4.12) with $\alpha = 0.35 \pm 0.04$. The string tension κ is in the physical unit Gev/fm. 50

10 κ vs. β for $N_t = 4$, the transition point $\beta_c \sim 2.2985$. The data were calculated on lattices, $4 \cdot 9^2 \cdot 65$ (squares), $4 \cdot 11^2 \cdot 65$ (triangles). The solid line is the fitting function in Eq. (4.14) with $\delta = 0.22 \pm 0.03$. The string tension κ is in the physical unit Gev/fm. 52

11 The $q\bar{q}$ color sources in a long rectangular box. The flux lines between the $q\bar{q}$ pair are confined by side walls and have a flux tube form. 56

12 The energy density ρ_E flux distributions in the region of $\beta > \beta_c$. The flux data were measured on lattices $4 \cdot N_s^2 \cdot 65$ with $\beta = 2.40$ for various spatial sizes, (a) $N_s = 5$, (b) $N_s = 7$, (c) $N_s = 9$, and (d) $N_s = 11$. The data are in the physical unit Gev/fm^3. 59

13 The action density ρ_A flux distributions in the region $\beta > \beta_c$, with the $q\bar{q}$ separations, (a) $r = 3a$, (b) $r = 4a$, (c) $r = 5a$ and (d) $r = 6a$. The data were measured on lattices $4 \cdot 5^2 \cdot 65$ with $\beta = 2.40$, and in the physical unit Gev/fm^3. 61

14 The center slice energy σ_E and action σ_A versus the $q\bar{q}$ separation r in the region of $\beta > \beta_c$, (a) σ_E vs. r, (b) σ_A vs. r. The data were measured on lattices $4 \cdot N_s^2 \cdot 65$ with $\beta = 2.36$ for various spatial sizes, $N_s = 5$ (circles), $N_s = 7$ (squares), $N_s = 9$ (triangles), $N_s = 11$ (diamonds). The data are in the physical unit Gev/fm.. 62

15 The plot of σ_E in the region of $\beta > \beta_c$ versus the transverse size N_s at large $q\bar{q}$ separation $r = 6a$. The solid line is the Coulomb behavior $(N_s a)^{-2}$, the dashed line is the inverse quartic behavior $(N_s a)^{-4}$, both are normalized to the data at $N_s = 5$. 65

16 The action density ρ_A flux distributions in the region of $\beta < \beta_c$ for various separations (a) $r = 3a$, (b) $r = 4a$, (c) $r = 5a$ and (d) $r = 6a$. The flux data were measured on lattices $4 \cdot 11^2 \cdot 65$ with $\beta = 2.25$, and measured in the physical unit Gev/fm^3. 67

17 The center slice energy σ_E and action σ_A versus the $q\bar{q}$ separation r in the region of $\beta < \beta_c$, (a) σ_E vs. r, (b) σ_A vs. r. The data were measured on lattices $4 \cdot N_s^2 \cdot 65$ with $\beta = 2.28$ for various spatial size, $N_s = 5$ (circles), $N_s = 7$ (squares), $N_s = 9$ (triangles), $N_s = 11$ (diamonds); and are in the physical unit Gev/fm. 68

18 The Wilson loop W of the temporal size na and the spatial size r. The plaquette P_1 is outside the Wilson loop W, and the plaquette P_2 is inside the Wilson loop W. 76

19 The plot of the predictions of σ_A vs. β of Eq.(6.46) (solid lines), and Eq.(6.51) (dashed lines). The two solid lines represent the upper and lower limits of the predictions of Eq.(6.46). The data of σ_A were measured from lattices $4 \cdot 9^2 \cdot 65$ (squares) and $4 \cdot 11^2 \cdot 65$ (triangles), which have the physical unit Gev/fm. 91

20 The weight function $p(x)$ vs. x, which is in the interval $[a, b]$. x_i is some accepted x value..... 100

21 The locus of the minimum of the action $S(U)$ in the phase space of the link variable U. Here ω_U is the phase factor of the link value U to be updated, ω' is the phase factor of the trial value U', and ω_g is the phase factor of the element g_0 which minimizes the action S. 106

22 One 'staple' M_{jkli} that couples with the link U_{ij}, where $M_{jkli} = U_{jk}U_{kl}U_{li}$. 108

ABSTRACT

The strong interactions between quarks are believed to be described by *Quantum Chromodynamics* (QCD), which is a non-abelian $SU(3)$ gauge theory. It is known that QCD undergoes a deconfining phase transition at very high temperatures, that is, at low temperatures QCD is in a confined phase, at sufficient high temperatures it is in a unconfined phase. Also, quark confinement is believed to be due to the string formation.

In this dissertation we studied $SU(2)$ gauge theory using numerical methods of LGT, which will provide some insights about the properties of QCD because $SU(2)$ is similar to $SU(3)$. We measured the flux distributions of a $q\bar{q}$ pair at various temperatures in different volumes. We find that in the limit of infinite volumes the flux distribution is different in the two phases. In the confined phase strong evidence is found for the string formation, however, in the unconfined phase there is no string formation. On the other hand, in the limit of zero temperature and finite volumes we find clear signal for string formation in the large volume region, however, the string tension measured in intermediate volumes is due to finite volume effects, there is no intrinsic string formation.

The color flux energies (action) of the $q\bar{q}$ pair are described by Michael sum rules, The original Michael sum rules deal with a static $q\bar{q}$ pair at zero temperature in infinite volumes. To check these sum rules with our flux data at finite temperatures, we present a complete derivation for the sum rules, then generalize them to account for finite temperature effects. We find that our flux data are consistent with the prediction of generalized sum rules.

Our study elucidate the rich structures of QCD, and provide evidences for the quark confinement and string formation. This supports the belief that QCD is a correct theory for strong interactions, and quark confinement can be explained by QCD.

CHAPTER 1

INTRODUCTION

There is strong evidence that particles, such as nucleons and mesons, are made of quarks, although no free isolated quark has yet been found[1]. One way out of this dilemma is to conjecture that quarks can not exist in the free state, but only exist in bound states. For example, nucleons are bound states of three quarks (qqq), mesons are those of a quark and an antiquark ($q\bar{q}$). This is known as 'quark confinement'. The interactions between quarks are the strong interactions, which are believed to be described by quantum chromodynamics (QCD). According to QCD the interactions between quarks become weak at short distances, however, with the increase of the distance it becomes strong. This is called 'asymptotic freedom'[2]. It was also proposed that QCD undergoes a deconfining phase transition at very high temperatures[3, 4], that is, quarks are confined at low temperatures, however, at sufficiently high temperatures they are in the unconfined state. These results show that there are rich structures of QCD to be studied. In this thesis we will consider QCD in finite volumes and at finite temperatures, to study the quark confinement problem and other properties of QCD in different phases using numerical methods of lattice gauge theory (LGT). To motivate this we first review the introduction of the quark model and QCD theory, and explain why we need a numerical approach to this problem. Then we will summarise our main results and explain the organization of this thesis.

Particles are classified according to their interactions, those with strong interactions are called *hadrons*. The hadron fermions are called *baryons*, such as p, n and Λ, which have spin $\frac{1}{2}$. The hadron bosons are called *mesons*, such as π and K, which have spin 0. By the early 1960s hundreds of particles and resonant states belong to the hadron category have been discovered. To solve the problem of the large number of "elementary particles", people began to suggest that all hadrons have a common underlying substructure, in a manner analogous to the atomic theory explanation of the profusion of elements in the periodic table.

In 1964, Gell-Mann [5] and independently Zweig [6], proposed that hadrons were composed of fractionally charged sub-particles called quarks. All baryons are bound states of three quarks (qqq), and all mesons are composed of a quark and an antiquarks ($q\bar{q}$). At that time they proposed that there are three kinds (or flavors) of quarks, named u, d and s. Later more flavors of quarks were discovered. According to this model a proton is composed of two 'up' quarks and a 'down' quarks, (uud), and a π^+ meson is ($u\bar{d}$), other hadrons have similar quark compositions. This quark model works very successfully in explaining why the vast number of hadrons can be arranged into some supermultiplets, and in predicting the hadron masses. Also the prediction of the ratio of neutron and proton magnetic moments from this quark model are in excellent agreement with experimental results [1].

Strong evidence for the quark model came from experiments carried out in the 1960's [7]. High energy electrons (7-17 Gev) were made to collide with protons, and 'deep inelastic' events were selected, i.e. $ep \rightarrow eX$ where X indicates all final states. These events involve a large amount of momentum

and energy transfer to the proton. It was observed that some incident electrons were scattered at much larger angles than expected if the proton was a continuous charge distribution. This shows that the electron is scattered from pointlike constituents of the proton. The situation is similar to the Rutherford's atomic scattering experiment, which uncovered the nuclear structure of atoms. Detailed analysis of the experiments strongly suggest that nucleons contain pointlike constituents, which have spin $\frac{1}{2}$ and fractionally charges.

The success of the quark model spurred a number of experiments to search for free quarks [1, 8]. However, no evidence is seen for the existence of free quarks in terrestrial conditions. This supports the idea of quark confinement.

So far all experimental evidence supports the quark model. However, a problem arises when one considers the Δ^{++} particle, which is composed of three u quarks, and has spin $J = 3/2$ with zero orbital angular momentum, $L = 0$. This is a system with three identical spin $\frac{1}{2}$ fermions u. The total wave function of the system is

$$\begin{aligned} \psi(\Delta^{++}) &= \psi_{spin}\psi_{flavor}\psi_{space} \\ &= (\uparrow\uparrow\uparrow)(uuu)\psi_{space}. \end{aligned} \tag{1.1}$$

One can immediately see that the spin part and flavor part of the wave function, ψ_{spin} and ψ_{flavor}, are symmetric under the interchange of any two quarks. Since the orbital angular momentum L is zero, the space part ψ_{space} must also be symmetric. So the overall wave function $\psi(\Delta^{++})$ is symmetric. This appears to violate the Pauli exclusion principle, which requires that a composite state of identical fermions should have an antisymmetric wave function.

To solve this problem one can assume that quarks possess another degree of freedom, described by a new quantum number called *color*, which can take three values, say R (red), B (blue) and G (green). Then one can construct a color wave function ψ_{color} which is antisymmetric under quark interchange. The overall wave function $\psi(\Delta^{++})$ in Eq. (1.1) should be replaced by

$$\psi(\Delta^{++}) = (\uparrow\uparrow\uparrow)(uuu)\psi_{space}\psi_{color}, \tag{1.2}$$

$$\text{with} \quad \psi_{color} = \frac{1}{\sqrt{6}}(RGB + GBR + BRG - RBG - BGR - GRB). \tag{1.3}$$

where ψ_{color} is antisymmetric under quark interchange. Then the problem of quark statistics is solved with the introduction of the color quantum number. There also exist some other rather convincing experimental evidence for the color hypothesis, which are discussed in ref. [1]. What is very interesting is that ψ_{color} in Eq. (1.3) is a singlet representation of the $SU(3)$ group, i.e. it is invariant under permutation of color variables. By extension, it was found that all hadrons are color singlets. Quarks carry the color indices, R, B or G, which form a triplet representation of the $SU(3)$ group. This seems to imply that only color singlets are not confined, and quark confinement is simply color confinement.

If color is confined, there must be a force, or a field, associated with color, so that any particles with color would be confined by the force, then only "colorless" (or color singlet) particles can exist freely. It is believed that the strong interactions between quarks are due to this color force, and this force can be described by quantum chromodynamics (khroma=color), or QCD. The QCD theory says that like electric and weak charges, the color charge is also associated with a gauge field whose quanta mediate the strong interactions

between quarks. Since there are three color charges, i.e. R, B or G, which form a triplet representation of a $SU(3)$ group, the color gauge field preserves the local $SU(3)$ gauge symmetry. This is different from quantum electrodynamics (QED), which has a local $U(1)$ gauge symmetry because there is only one electric charge. The quanta of the color field are called gluons, which have $J^P = 1^-$ and $m = 0$. There are eight gluons, forming an 8 dimensional representation (the octet) of the $SU(3)$ color gauge group. Since gluons themselves carry color charges, they can couple to each other.

Because of the gluon-gluon coupling, QCD has different features from QED. According to QED a real electron is surrounded by clouds of virtual e^+e^- pairs due to *vacuum polarisation.* This leads to the *screening* of the electric charge. So when one measures the charge of the electron by the Coulomb force on a test charge, the effective electric charge measured by the test charge at large distances is less than what it is at small distances, as shown in Fig. 1(a) below. The situation in QCD is similar, a quark with color charge is surrounded by a cloud of virtual $q\bar{q}$ pairs and gluons. But there is an additional feature that gluons couple to themselves, which makes a crucial difference. The effect is to make a R color charge (say) attract preferentially other R charges (not B or G) to itself. This differs from QED and results in the *antiscreening* of color charges. So the effective color charge of the quark measured by a test color charge at large distances is greater than that at small distances, as shown in Fig. 1(b) below. This peculiar property of QCD is known as *asymptotic freedom.* From this behaviour one can see that the coupling between quarks becomes strong with the increase of their separation, which supports the quark confinement hypothesis.

The asymptotic freedom of QCD has been confirmed by the deep inelastic scattering experiments [1]. In these experiments the nucleons were found to be a loosely bound collection of quarks and gluons. At high energies (corresponding to short distances) the coupling between quarks becomes weak, and the higher the energy, the weaker the coupling. This agrees with asymptotic freedom.

The usual analytical approach to solve field theories is perturbation theory, which involves an expansion in the coupling constant. This method is extremely successful in calculating properties of QED at low energies (i.e. large distances), because the dimensionless coupling, $\alpha = e^2/(4\pi\hbar c)$, of QED is very small ($\ll 1$) in this case. However, to study the low-energy properties of QCD this method can not be used, because the coupling constant of QCD is large at low energies. One must search for some nonperturbative methods.

The most productive nonperturbative approach is lattice gauge theory (LGT), proposed by K. Wilson in 1974 [9]. This is a formulation of quantum field theory on a Euclidean spacetime grid, which in our study is a four-dimensional hypercube. We will discuss the details of LGT in next chapter. One advantage of LGT is that one can avoid the infinity problems arising in a continuum field theory. Another motivation for LGT is that it takes advantage of the deep connections between quantum field theories and statistical mechanics. Thus many methods in statistical mechanics, such as Monte Carlo techniques and high temperature expansions, can be applied to LGT. Now by using these techniques one can study the properties of QCD even in the strong coupling region.

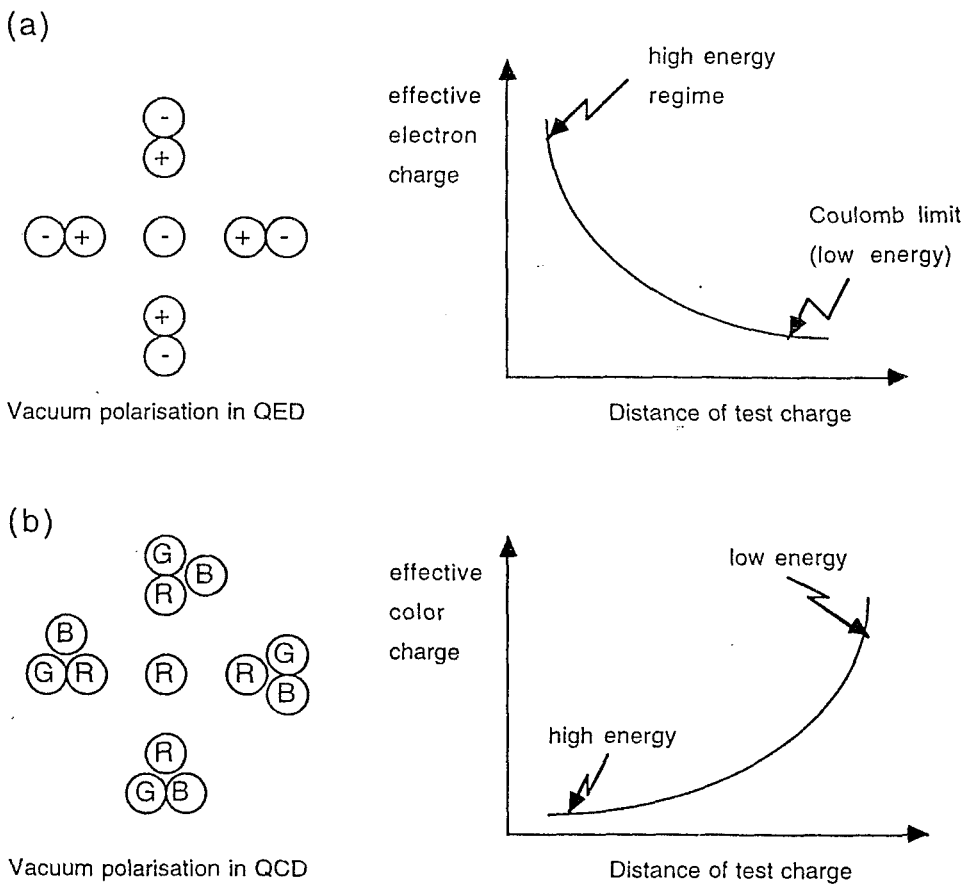

Figure 1. (a) Screening of electric charge as a consequence of vacuum polarisation of QED. (b) Antiscreening of color charge as a consequence of vacuum polarisation of QCD.

Although some results of QCD support the quark confinement hypothesis, no proof of this hypothesis from QCD has been found yet. To understand how quarks can be permanently confined, it was conjectured that the color field lines between quarks have a string-like flux tube form, as shown in Fig. 2 below. And the energy stored in the flux tube per unit length is a constant, κ, called the string tension. Consider the quark-antiquark bound state $(q\bar{q})$, the meson. If string formation occurs, the potential energy $V(r)$ of the $q\bar{q}$ pair would increases linearly with the $q\bar{q}$ separation r, $V(r) \sim \kappa r$. This results in the permanent confinement of the $q\bar{q}$ pair.

By using LGT techniques one can calculate the potential energy $V(r)$ and the flux distributions of a $q\bar{q}$ pair. Some results have shown clear evidence that in the limit of large volumes and zero temperature the potential energy $V(r)$ is linear for large r [10], and the flux lines form a string-like flux tube between the $q\bar{q}$ pair[11].

In 1978 A.M. Polyakov[3] and L. Susskind[4] proposed independently that QCD undergoes a phase transition at a very high temperatures (T_c). For $T < T_c$, quarks and gluons are in confined bound states; however, For $T > T_c$, they are in a plasma-like state. This has also been confirmed by many LGT results[12, 13]. The study of QCD at high temperatures is of many important significances. High energy heavy ion collisions can produce hadronic matters at high temperatures, if the colliding energy is high enough one expects that the quark-gluon plasma would form in the process. Such experiments could provide further tests of QCD as being the correct theory describing the strong interactions. Also, such hadronic matter at very high temperatures and densities was surely present in the early stages of the big-bang universe, and

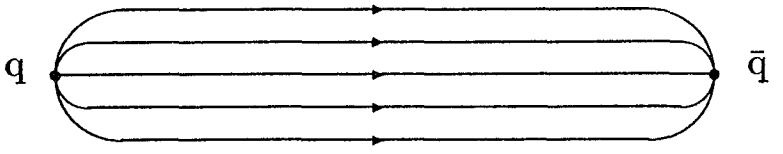

Figure 2. The conjectured $q\bar{q}$ flux distribution in the confined phase, which has the string-like flux tube form.

may be encountered in neutron stars. Hence it is important to study QCD at very high temperatures for constructing models of the universe and neutron stars.

Another way to study QCD is to take advantage of the *asymptotic freedom* character of QCD. As we discussed above, the coupling between quarks is weak at small distances, this opens the possibility to solve QCD analytically. M. Luscher considered the $SU(N)$ gauge theory ($SU(3)$ for QCD) in small volumes[14], and derived an effective hamiltonian for the theory. Subsequently the lowest energy levels of $SU(2)$[15] and $SU(3)$[16] gauge theories in small volumes were computed by using Luscher's hamiltonian. He also introduced a dimensionless variable[15],

$$z_g \equiv m(0^+)L, \tag{1.4}$$

to characterize the physical size of the volume. Where $m(0^+)$ is the lowest glueball mass, which is the energy gap or the inverse of the correlation length; and L is the linear size of the box. The small volumes are defined as those with with $z_g \leq 1$. In this domain the string tension is found to be zero [15, 18], which is consistent with asymptotic freedom. To compare with physics of real world, one must extend these results to large volumes. Later P. van Baal and J. Koller[17, 18] generalized Luscher's analytical calculations to the intermediate volumes, i.e. $1 \leq z_g \leq 5$, in which LGT calculations are also accessible. B.A. Berg and A.H. Billoire [19] carried out a thorough LGT study in the intermediate volume region. Their results are in good agreement with the analytical results of van Baal and Koller. In this domain they did not find evidence for string formation, although they did find a string tension. It is suspected that the string tension is not due to the intrinsic string formation,

but to finite volume effects. Intrinsic string formation is expected to occur in large volumes, i.e. $z_g \geq 5$.

Now we can summarize the properties of QCD clearly on the plane of the temperature (T) and the inverse volume ($1/V$), as shown in Fig. 3. This figure takes liberties, because there is no true phase transition in finite volumes. This figure shows that in the infinite volume limit ($V \to \infty$), QCD has a phase transition at the finite temperature, T_c. At zero temperature the system has no string formation in small and intermediate volumes, and the string formation is expected to occur in large volumes. In this figure for cases of finite volume 'confinement' only means string formation, 'unconfinement' only represents that there is no string formation.

Pure $SU(2)$ gauge theory contains already essential features of full QCD, but it is much simpler to study than $SU(3)$, and takes much less computer time for Monte Carlo simulations. So in this work we shall only consider the pure $SU(2)$ gauge theory, which corresponds to the case of static quark sources. We wish to answer the question of the volume at which the intrinsic string formation occurs in the zero temperature limit, and understand the properties of QCD in both phases in the infinite volume limit. We measured the flux distributions of a static $q\bar{q}$ pair in various volumes and temperatures, which covers the finite temperature phase transition region, and the region from intermediate volumes to large volumes in the zero temperature limit. Our results provide evidence that string formation occurs in the confined phase, but does not occur in the unconfined phase. We then measured the string tension κ at various temperatures in the confined phase, and studied its behaviour with temperature. For cases of finite volumes our results verified the expectation

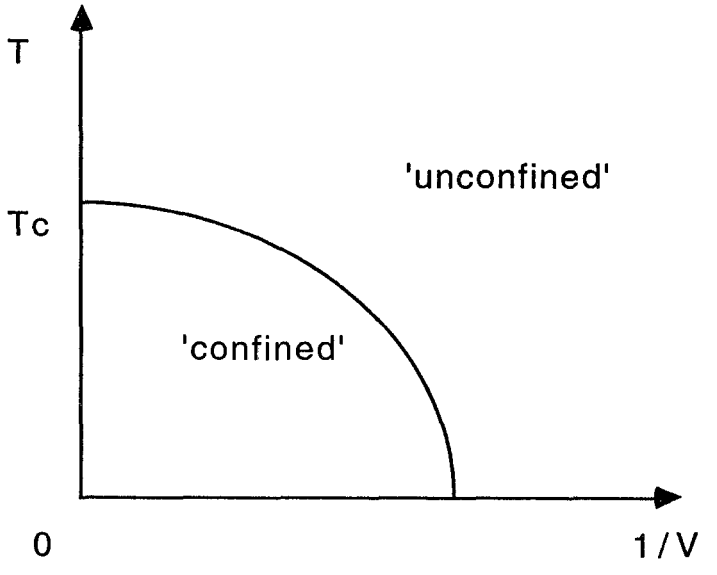

Figure 3. The properties of QCD can be shown diagrammally by the 'phase diagram' on the plane of T and $1/V$.

that the string tension in intermediate volumes are just due to finite volume effects, and we also found some evidences for string formation in large volumes.

For a $q\bar{q}$ pair the color flux energies are related to the potential energy $V(r)$ by some identities called Michael sum rules[20]. To analyse our flux data measured on finite lattices using the sum rules, we generalized these sum rules to account for the finite size effects. Our flux data support this generalization.

This dissertation is organized as follows. Chapter 2 gives a brief introductory review of LGT and some basic concepts. The implementations and interpretations of LGT will be discussed. In Chapter 3 we describe the calculation methods on lattices, and the measured quantities and their interpretations. Then we present our numerical results. In Chapter 4 we discuss some results of the finite temperature phase transition from our LGT calculations, In Chapter 5 we then present detailed analysis of the $q\bar{q}$ flux distributions measured on various lattices. In Chapter 6 we shall review the derivation of Michael sum rules, and generalize these sum rules to include finite size effects. Then we apply the sum rules to analyse our flux data. Finally, we present the summary and conclusions. A detailed discussion of Monte Carlo methods used in LGT calculations are presented in Appendix A. Also the proof of a relation used in the derivation of Michael sum rules is given in Appendix B.

CHAPTER 2

LATTICE GAUGE THEORY BASICS

In this chapter we review the introduction of lattice gauge theory, and discuss in general terms how a lattice calculation is performed and interpreted.

2.1 Introduction of LGT

In four-dimensional Euclidean space the action of the full QCD theory is given by[10]

$$\begin{aligned} S &= S_G + S_F \\ &= \frac{1}{2}\int d^4x Tr(F_{\mu\nu}F_{\mu\nu}) + \int d^4x \bar{\psi}(x)(\gamma_\mu D_\mu + M)\psi(x). \end{aligned} \tag{2.1}$$

where S_G represents the gauge field part of the action, and S_F the fermion field (quarks) part. the color field strength tensor is defined as

$$F_{\mu\nu} = \partial_\mu A_\nu - \partial_\nu A_\mu + ig[A_\mu, A_\nu], \tag{2.2}$$

with the gauge field A_μ which can be expanded in terms of the generators τ_i of the $SU(N)$ gauge group, i.e.

$$A_\mu(x) = \frac{1}{2}\tau_i A_\mu^i \qquad (i = 1, 2, \cdots, n_g). \tag{2.3}$$

For QCD the gauge group is $SU(3)$ which has eight generators, i.e. $n_g = 8$. The fermion field $\psi(x)$ describes the quarks of the theory, $D_\mu = \partial_\mu + igA_\mu$, M is the mass matrix for quarks.

In the static quark limit ($M \to \infty$), one can show that the effective action of the theory is only the gauge field part[10],

$$S = S_G = \frac{1}{2} \int d^4x Tr(F_{\mu\nu} F_{\mu\nu}). \tag{2.4}$$

Fortunately, the fundamental problems of QCD, such as quark confinement, can be studied without the introduction of dynamical quarks. It can also be argued that the static quark approximation is good to describe real heavy quarks such as the b-quark. In the following we shall only consider the theory in this limit.

In field theory all physical information about the system can be extracted from a correlation function, e.g. $< C >$, where C represents a product of operators. The correlations can be calculated from the following path integral expression,

$$< C >= \frac{\int [DA_\mu] C e^{-S}}{\int [DA_\mu] e^{-S}}. \tag{2.5}$$

As we mentioned before, the renormalized coupling constant of QCD becomes strong in the low energy region because of asymptotic freedom. One can not calculate the quantity in Eq. (2.5) analytically in this case. However, LGT opens the way to solve the problem using numerical methods.

Let us now turn to the lattice formulation of quantum field theory[9, 21, 10]. In this formalism spacetime is represented by a discrete, hypercubical grid. The gauge fields, which mediate the interactions between quarks, are defined on the links (strictly speaking, gauge group elements exist on links), while matter fields like quarks exist on the sites of the lattice. On a finite lattice the system has a finite number of degrees of freedom, which enable us to do numerical calculations. Then the lattice spacing is supposed to be

taken to zero, and the LGT calculated results approach those in the continuous Euclidean space.

For the pure $SU(N)$ LGT the fundamental variable is the link variable, which is the group element associated with the link, i.e. $U_\mu(n)$, as shown in Fig. 4 (a). The link variable can be written as,

$$U_\mu(n) = exp(iB_\mu(n)), \tag{2.6}$$

with $B_\mu(n) = \frac{1}{2}ag\tau_i A^i_\mu(n)$ $(i = 1, 2, \cdots, n_g)$, and a the lattice spacing. The index n denotes the site of the link, μ is the direction of the link. If the link takes the opposite direction $-\mu$, it is associated with the inverse group element, $U^{-1}_\mu(n)$, that is,

$$U_{-\mu}(n+\mu) \equiv U^{-1}_\mu(n). \tag{2.7}$$

Any physical gauge field theory should be locally gauge invariant, that is, physical quantities are invariant under local gauge transformations. At each lattice site we define an arbitrary group element,

$$g(n) = \exp[-i\frac{1}{2}\tau_i\chi_i(n)], \tag{2.8}$$

where $\chi_i(n)$ is a function of the lattice site n, and $i = 1, 2, \cdots, n_g$. The local gauge transformation for the link variable $U_\mu(n)$ (gauge field) is defined as

$$U_\mu(n) \rightarrow U'_\mu(n) = g(n)U_\mu(n)g^{-1}(n+\mu). \tag{2.9}$$

Then in LGT the simplest quantity which is locally gauge invariant is the plaquette variable, which is the product of link variables $U_\mu(n)$ around the plaquette, i.e.

(a)

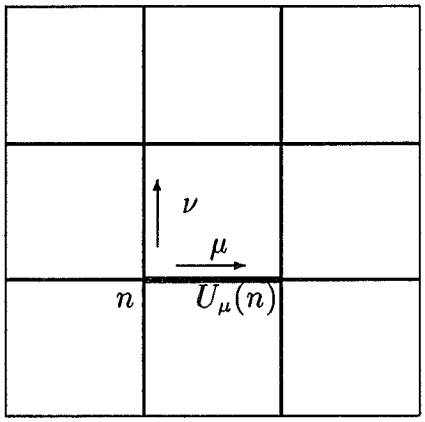

(b)

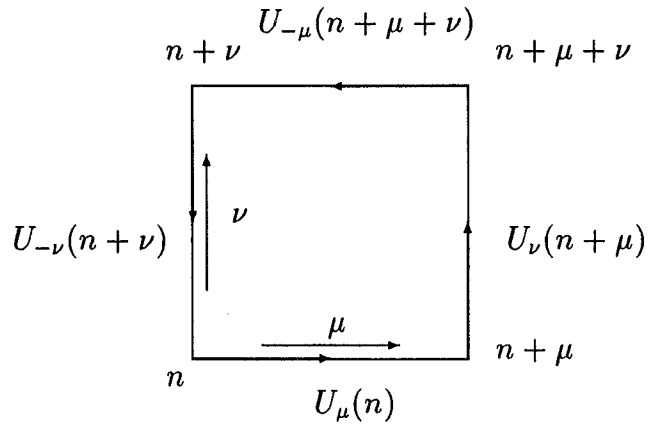

Figure 4: (a). The link variable U_μ; (b). The plaquette variable U_P.

$$\begin{aligned} U_P(n,\mu,\nu) &= U_\mu(n)U_\nu(n+\nu)U_{-\mu}(n+\mu+\nu)U_{-\nu}(n+\nu) \\ &= U_\mu(n)U_\nu(n+\mu)U_\mu^{-1}(n+\nu)U_\nu^{-1}(n), \end{aligned} \tag{2.10}$$

as shown in Fig. 4 (b). So in LGT the physical quantities of local gauge invariance can be built from the plaquette variables U_P.

The standard Wilson action of the $SU(N)$ LGT is constructed from the plaquette variables as[21],

$$S = \beta \sum_{n,P} [1 - \frac{1}{N} Re(TrU_P(n,\mu,\nu))], \tag{2.11}$$

with the sum over all lattice sites n and the plaquette orientations P, and $\beta = 2N/g^2$, which is analogous to $1/kT$ in statistical mechanics. In the following we shall show that in the naive continuum limit, $a \to 0$, this action becomes that of the continuous $SU(N)$ gauge theory in Eq. (2.4).

In the limit of $a \to 0$, the field variables $B_\mu(n+\nu)$ and $B_\nu(n+\mu)$ associated with the link variables $U_\mu(n+\nu)$ and $U_\nu(n+\mu)$ can be Taylor expanded as

$$\begin{aligned} B_\nu(n+\mu) &\approx B_\nu(n) + a\partial_\mu B_\nu(n) + O(a^2), \\ B_\mu(n+\nu) &\approx B_\mu(n) + a\partial_\nu B_\mu(n) + O(a^2). \end{aligned} \tag{2.12}$$

Then the plaquette variable becomes,

$$\begin{aligned} U_P(n,\mu,\nu) &= U_\mu(n)U_\nu(n+\mu)U_\mu^{-1}(n+\nu)U_\nu^{-1}(n), \\ &\approx \exp[iB_\mu(n)]\exp[i(B_\nu(n) + a\partial_\mu B_\nu(n))] \\ &\quad \times \exp[-i(B_\mu(n) + a\partial_\nu B_\mu(n))]\exp[-iB_\nu(n)]. \end{aligned} \tag{2.13}$$

After using the operator identity,

$$e^A e^B = \exp(A + B + \frac{1}{2}[A, B] + \cdots), \tag{2.14}$$

we get

$$\begin{aligned} U_P(n, \mu, \nu) &\approx \exp(ia(\partial_\mu B_\nu - \partial_\nu B_\mu) - [B_\mu, B_\nu]) \\ &\approx \exp(ia^2 g(\partial_\mu A_\nu - \partial_\nu A_\mu + ig[A_\mu, A_\nu])) \\ &\approx \exp[ia^2 g F_{\mu\nu}(n)]. \end{aligned} \tag{2.15}$$

Therefore, one has

$$\begin{aligned} Tr(U_P(n, \mu, \nu)) &\approx Tr(\exp[ia^2 g F_{\mu\nu}(n)]) \\ &\approx Tr(1 + ia^2 g F_{\mu\nu}(n) - \frac{1}{2}a^4 g^2 F_{\mu\nu}^2(n) + \cdots) \\ &\approx N - \frac{1}{2}a^4 g^2 Tr(F_{\mu\nu}^2(n)) + \cdots. \end{aligned} \tag{2.16}$$

So the Wilson action in Eq. (2.11) becomes,

$$S \approx \beta \sum_{n,P} \frac{1}{2N} a^4 g^2 ReTr(F_{\mu\nu}^2(n)). \tag{2.17}$$

If we apply the replacement to Eq. (2.17),

$$\sum_{n,P} \rightarrow \int \frac{d^4x}{a^4} \frac{1}{2} \sum_{\mu,\nu}, \tag{2.18}$$

we get

$$\begin{aligned} S &\approx \sum_P \int d^4x Tr(F_{\mu\nu}^2), \\ &= \frac{1}{2} \sum_{\mu,\nu} \int d^4x Tr(F_{\mu\nu} F_{\mu\nu}). \end{aligned} \tag{2.19}$$

This is just the action S in Eq. (2.4), which is the gauge field action of QCD in the continuous Euclidean space.

We now have a Euclidean statistical mechanical system in the canonical ensemble with partition function

$$\begin{aligned} Z &= \int [dU] e^{-S(U)} \\ &= \int \prod_{n,\mu} [dU_\mu(n)] e^{-S(U)}. \end{aligned} \tag{2.20}$$

This is a multi-dimensional integration over all link variables $U_\mu(n)$ on the lattice. As the gauge groups are compact, the group volumes are finite, such integrals are well defined and have simple invariance properties. With this definition the path integral formalism of Eq. (2.5) can be transformed into the following form. If H is some physical quantity, which is a local gauge invariant function of the link variables $U_\mu(n)$, then the expectation value can be calculated as

$$< H >= Z^{-1} \int (dU) H(U) e^{-S(U)}. \tag{2.21}$$

This expression can be calculated by Monte Carlo simulation methods in LGT, which will be discussed in Appendix A. In the following I proceed to discuss the interpretations of a few important physical quantities in LGT.

2.2 Interpretation of Some Physical Quantities

(1). The Wilson Loop W

Static quark sources were first introduced by Wilson[9] in his original formulation of LGT, via the Wilson loop. To understand this[22], consider a $q\bar{q}$ pair to be created at the time $t = 0$, and kept at a distance R for a time T, then brought together and annihilated. The world line of such a $q\bar{q}$ pair would form a closed loop in spacetime. The Euclidean amplitude for this process is

given by the matrix element,

$$< i|e^{-HT}|f >, \tag{2.22}$$

where $|i>$, $|f>$ represent the initial and final states, i.e. the $q\bar{q}$ pair a distance R apart, and H is the hamiltonian. The transition amplitude can be written as the path integral form similar to Eq. (2.5),

$$< i|e^{-HT}|f >= \frac{\int [DA_\mu] exp[-S + ig \int d^4x A_\mu J_\mu]}{\int [DA_\mu] e^{-S}}, \tag{2.23}$$

where J_μ is an external current density describing the world lines of the $q\bar{q}$ pair. For a point source current loop the term $A_\mu J_\mu d^4x$ becomes $A_\mu dx_\mu$. Since $|i>$, $|f>$ are identical and because this is a static process, the above equation reduces to,

$$exp(-E(R)T) =< trPexp[ig \oint A_\mu dx_\mu] > \tag{2.24}$$

where $E(R)$ is the color field energy of the $q\bar{q}$ pair[20], and P stands for path ordering. The quantity on the R.H.S. of Eq. (2.24) is called the Wilson loop correlation function. On the lattice the Wilson loop can be defined as the product of link variables U along a closed path[22],

$$W = \frac{1}{N} tr \prod_C U_\mu(n), \tag{2.25}$$

where N is for $SU(N)$, In Figure 5 (a) we show such a Wilson loop on the z-t plane of a lattice. From Eq. (2.24) one can see that the expectation of the Wilson loop is associated with the energy E(R) of a static $q\bar{q}$ pair,

$$< W >\sim e^{-TE(R)}. \tag{2.26}$$

The expectation $< W >$ is given by Eq. (2.21) in LGT, which can be calculated by numerical methods and other techniques.

(a)

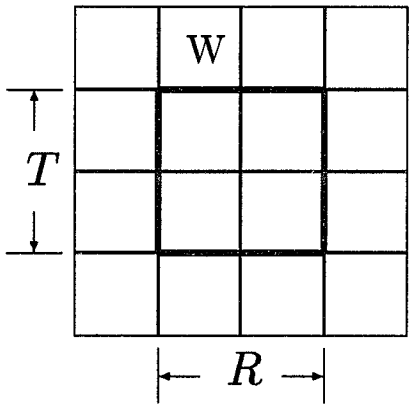

(b)

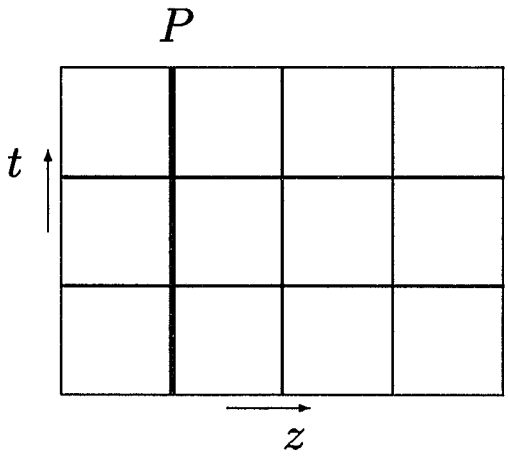

Figure 5. (a) The Wilson loop W on the z-t plane, (b) The Polyakov loop P along the time direction.

(2). The Polyakov Loop P

In LGT the Polyakov loop along the time direction is defined to be the product of all links along a path in that direction. Since the lattice has periodic boundary conditions, the path forms a closed loop, that is,

$$P(\vec{x}) = \frac{1}{N} tr \prod_{\tau=1}^{N_t} U_t(\vec{x}, \tau), \tag{2.27}$$

where N is for $SU(N)$, and N_t is the lattice size in the time direction, as shown in Fig. 5 (b). As we discussed above, a time directed line on the lattice represents a color charge source (or a quark), thus one can show that the expectation value of $P(\vec{x})$ is associated with the free energy F_q of an isolated quark q in the limit of infinite volume[23],

$$< P(\vec{x}) > \sim e^{-L_t F_q}, \tag{2.28}$$

where $L_t = N_t a$ is the temporal size of the lattice in physical units.

For two Polyakov loops $P(0)$ and $P(\vec{r})$, the correlation of them, $< P(0)P^\dagger(\vec{r}) >$, is related to the free energy $V(\vec{r})$ of a $q\bar{q}$ pair,

$$< P(0)P^\dagger(\vec{r}) > \sim e^{-L_t V(\vec{r})}, \tag{2.29}$$

where $P^\dagger(\vec{r})$ is the hermitian conjugate of $P(\vec{r})$, and $\vec{r}$ is the separation of the $q\bar{q}$. Usually, $V(\vec{r})$ is identified to be the potential energy of the $q\bar{q}$ pair.

2.3 The Scaling Relation $a(\beta)$ Of $SU(2)$ LGT

In LGT physical quantities are calculated in unit of the lattice spacing a. To obtain values of physical quantities in physical units one needs to know the lattice spacing a in physical units. In $SU(N)$ LGT there exists a scaling

relation $a(\beta)$ between the lattice spacing a and the lattice coupling constant $\beta = \frac{2N}{g^2}$ in the continuum limit ($a \to 0$)[21],

$$a = \Lambda_L^{-1}(\frac{2Nb_0}{\beta})^{-b_1/(2b_0^2)} exp(-\frac{\beta}{4Nb_0})(1 + O(g^2)), \tag{2.30}$$

with $b_0 = \frac{1}{16\pi^2}\frac{11N}{3}$, and $b_1 = (\frac{1}{16\pi^2})^2\frac{34N^2}{3}$, and Λ_L is the lattice scaling constant, which can be determined from experimental data.

This relation was derived from the requirement that physical quantities should approach their physical values in the continuum limit ($a \to 0$)[21]. From the scaling relation $a(\beta)$ in Eq. (2.30) one can see that as the lattice spacing $a \to 0$, $\beta \to \infty$. This implies that the coupling constant $g \to 0$ at small length scales for the $SU(N)$ gauge theory, which agrees with *asymptotic freedom.*

For $SU(2)$ LGT Eq. (2.30) becomes,

$$a = \Lambda_L^{-1}(\frac{6}{11}\pi^2\beta)^{\frac{51}{121}} exp(-\frac{3}{11}\pi^2\beta)(1 + O(g^2)). \tag{2.31}$$

To calculate the lattice scaling constant Λ_L^{-1}, we follow refs.[25, 26] to choose a scale such that the string tension κ_0 at zero temperature ($T = 0$) in infinite volume is given by

$$\sqrt{\kappa_0} = 0.44 \quad Gev, \tag{2.32}$$

which can be determined from the Regge trajectory[27]. Here we take the string tension data from the real world as that of $SU(2)$ gauge theory for definiteness. From the data in refs.[24, 25] one can extract the following relation between the lattice spacing a and the lattice coupling constant β, as shown in Table 1, which is consistant with the similar result in ref.[28]. The values of Λ_L^{-1} were calculated from the scaling relation in Eq. (2.31) by substituting the values of a and β.

Table 1. The correspondence of the lattice spacing a and the coupling constant β for the $SU(2)$ LGT.

β	$a(\beta)\ fm$	$\Lambda_L^{-1}\ fm$
2.22	0.1981 (61)	27.41 (84)
2.30	0.1616 (47)	27.32 (79)
2.40	0.1210 (5)	26.30 (11)
2.50	0.0843 (8)	23.57 (22)

From Table 1 one can see that the values of Λ_L^{-1} changes slowly with β in the region, $2.22 \leq \beta \leq 2.5$. This implies that the perturbative asymptotic scaling relation in Eq. (2.31) is not exactly valid in this region. To study the non-perturbative physics and obtain the relation $a(\beta)$ for other β values in this region, we use the function in Eq. (2.31) to fit the data of Table 1, with Λ_L^{-1} considered as a function of β. For simplicity, we chose a quadratic function to fit the Λ_L^{-1} values. The result is,

$$a(\beta) = \Lambda_L^{-1}(\beta)(\frac{6}{11}\pi^2\beta)^{\frac{51}{121}} exp[-\frac{3}{11}\pi^2\beta] = \Lambda_L^{-1}(\beta)f(\beta), \tag{2.33}$$

with

$$\Lambda_L^{-1}(\beta) = d_1 + d_2\beta + d_3\beta^2 \quad fm, \tag{2.34}$$

where the coefficients $d_1 = 59.37 \pm 0.86$, $d_2 = -5.96 \pm 0.39$ and $d_3 = -3.28 \pm 0.17$. Using this scaling relation $a(\beta)$ one can transform the calculated values of physical quantities in $SU(2)$ LGT from the lattice units to physical units.

2.4 Transfer Matrix and Temperatures on Lattices

The path integral formulation of LGT reveals deep connections between field theories and statistical mechanics. Starting with the path integral formulation one can construct another formulation of LGT, i.e. the transfer

matrix formalism[21, 22], which resembles Hamiltonian quantum mechanics and exposes some of the physical properties of LGT quite simply.

For simplicity, let us introduce the transfer matrix formalism by first considering a one-dimensional quantum mechanical problem, a particle of mass m moving in the potential $V(r)$. In Euclidean space the Lagrangian of this particle is

$$L(x,\dot{x}) = \frac{1}{2}m\dot{x}^2 + V(x), \tag{2.35}$$

and the action is

$$S = \int d\tau L(x(\tau),\dot{x}(\tau)). \tag{2.36}$$

In the path integral formalism the path integral corresponding to the partition function of the system is

$$Z = \int [dx(\tau)]e^{-S}. \tag{2.37}$$

To calculate the above path integral one makes the time axis discrete and consider the total length to be finite (after calculations we then take the limit of continnum and infinite length,), that is, one introduces a one-dimensional time like lattice of size N_t,

$$\tau_n = na \qquad (n = 0,1,2,\cdots,N_t), \tag{2.38}$$

where a is the lattice spacing, and we assume that the lattice has the periodic boundary condition, i.e. $\tau_0 = \tau_{N_t}$. Then the action of Eq. (2.36) can be reduced to a sum

$$S = a\sum_{i=0}^{N_t-1}\left[\frac{1}{2}m\left(\frac{x_{i+1}-x_i}{a}\right)^2 + V(x_i)\right], \tag{2.39}$$

and the partition function of Eq. (2.37) can be written as

$$Z = \int (\prod_i dx_i)e^{-S}$$

$$= \int (\prod_i dx_i) < x_{N_t}|\mathcal{T}|x_{N_t-1} > \cdots < x_1|\mathcal{T}|x_0 >, \qquad (2.40)$$

with $< x'|\mathcal{T}|x >= exp[-\frac{m}{2a}(x'-x)^2 - \frac{a}{2}(V(x')+V(x))]$. The operator $\mathcal{T}$ is called the transfer matrix operator. From the completeness relation of the basis states $\{|x_i>\}$, i.e.

$$\int dx_i |x_i >< x_i| = 1, \qquad (2.41)$$

and the periodic boundary condition, $|x_{N_t} >= |x_0 >$, one can rewrite the partition function of Eq. (2.40) in the compact form,

$$Z = \int dx_0 < x_0|\mathcal{T}^N|x_0 >= Tr(\mathcal{T}^{N_t}). \qquad (2.42)$$

The key to the transfer matrix formalism of $SU(N)$ LGT in four-dimensional Euclidean lattices is to note that the plaquettes in the action of Eq. (2.11) can be classified into two types, the time-like plaquettes with a link along the time direction, and the space-like plaquettes without a time link. The time-like plaquettes are special, we can reorganize the plaquettes in the action so that the partition function of this theory in Eq. (2.20) can be written in the form[22]

$$\begin{aligned} Z &= \int < \{U_{N_t}\}|\mathcal{T}|\{U_{N_t-1}\} > [\prod dU_{N-1}] \cdots < \{U_1\}|\mathcal{T}|\{U_0\} > [\prod dU_0] \\ &= Tr(\mathcal{T}^{N_t}), \end{aligned} \qquad (2.43)$$

where $\{U_i\}$ represents all link variables at a given time τ_i. In Eq. (2.43) we have used the completeness relation and the periodic boundary condiction of the basis states $|\{U_i\}>$. Clearly, the transfer matrix $\mathcal{T}$ evolves the system one link in the time direction, which is similar to the Hamiltonian operator $\hat{H}$ in quantum mechanics.

Consider a four-dimensional Euclidean lattice of the size $N_t \times N_x \times N_y \times N_z$, if one chooses the direction of N_t to be the time direction, then one can write the transfer matrix $\mathcal{T}$ in this direction as[19], $\mathcal{T} = \mathcal{T}(N_x, N_y, N_z)$. And the eigenstates and eigenvalues of $\mathcal{T}$ are defined by means of

$$\mathcal{T}|n>=\lambda_n|n>, \tag{2.44}$$

with the eigenvalue $\lambda_n = e^{-m_n}$, and the eigenstate $|n>$ $(n \geq 0)$, the state $|0>$ denotes the vacuum. Where m_n is the energy difference between the eigenstate $|n>$ and the vacuum, then one has, $\lambda_0 = 1$.

With the definition of transfer matrix $\mathcal{T}$ we can rewrite the partition function Z of Eq. (2.43) as

$$Z = Tr(\mathcal{T}^{N_t}) = \sum_n e^{-m_n a N_t}, \tag{2.45}$$

and the expectation of a physical quantity $< H >$ in Eq. (2.21) becomes

$$< H >= Z^{-1} \sum_n < n|H|n > e^{-m_n a N_t}. \tag{2.46}$$

Comparing this equation with the expectation of a physical quantity in statistical mechanics, one can see that the quantity $1/(N_t a)$ plays the role of the temperature. More strictly one can show that in LGT the temperature T is related to the inverse temporal size of the lattice[29], i.e.

$$T = \frac{1}{N_t a}, \tag{2.47}$$

with N_t to be temporal size of the lattice, if the spacial sizes of the lattice N_x, N_y, N_z are all large compared to N_t.

CHAPTER 3

CALCULATION METHODS AND NUMERICAL RESULTS

In this chapter we shall discuss the calculation methods in LGT, and describe our measurements and present the raw data.

3.1 Calculation Methods of LGT

To perform a numerical study of the $SU(N)$ LGT, we choose a four-dimensional Euclidean lattice of the size, $N_t \times N_x \times N_y \times N_z$. As we discussed before the fundamental degree of freedom is the link variable. The configuration of the lattice system is determined by the values of each link. Since the lattice is finite, we impose boundary conditions, usually, periodic boundary conditions are applied. However, for convenience in programming we choose our lattices with helical boundary conditions[30]. We characterize the lattice sites by a set of integer coordinates (x,y,z,t), which correspond to N_x, N_y, N_z, N_t respectively. Then the helical boundary conditions implies that if we start along the N_x direction, after going through N_x sites, say, the link $U_x(N_x+1,1,1,1)$ is equal to the link $U_x(1,2,1,1))$, but not $U_x(1,1,1,1))$ as it is for periodic boundary conditions. Similar results hold for other links. With this boundary condition a site at the integer coordinates (x,y,z,t) can be uniquely associated with the integer,

$$j = x + N_x((y-1) + N_y((z-1) + N_z(t-1))). \tag{3.1}$$

To update the lattice configuration, the links in any given direction were updated in a checkerboard style. In order to get a four-dimensional "checkerboard" three dimensions must be of odd sizes, and the fourth even. All links emanating in a positive direction from odd sites are updated first followed by those from even sites[30]. We chose N_x, N_y, N_z odd, and N_t even. The lattice is truely periodic only in the N_t direction. We use the Metropolis algorithm alternated with the over-relaxation algorithm to update lattice configurations. The details of these algorithms will be discussed in Appendix A.

The lattice system is a statistical system. Before we make measurements, we must thermalize this system. The expectation of a quantity H in LGT, such as that in Eq. (2.21), can be calculated by the lattice average. That is, in a particular thermalized configuration we make one measurement, say H_1, then we update the lattice configuration with a number of sweeps and make another measurement, H_2. By repeating this process many times (e.g. N_m) we can obtain the lattice average,

$$< H >= \frac{1}{N_m} \sum_{i=1}^{N_m} H_i. \tag{3.2}$$

The statistical error of this measurement can be calculated as

$$\Delta H = \sqrt{\frac{< H^2 > - < H >^2}{N_m}}. \tag{3.3}$$

where $< H^2 >$ can be calculated in the same manner as $< H >$ in Eq. (3.2).

3.2 Numerical Results

In our study of the $SU(2)$ LGT we used the standard Wilson action defined in Eq. (2.11), i.e.

$$S(U) = \beta \sum_P (1 - \frac{1}{2} Tr U_P), \tag{3.4}$$

where $\beta = 4/g^2$ with g to be the lattice coupling constant, and U_P is the plaquette variable defined in Eq. (2.10).

To study the finite temperature phase transition and the physics in finite volumes at zero temperature (which will be explained in detail in next Chapter), we follow ref.[19] to choose our lattices of the geometry $N_t \cdot N_s^2 \cdot N_z$, with $N_t < N_s \ll N_z$. In our measurements we choose $N_t = 4$ and 6, $N_s = 5, 7, 9, 11$, and $N_z = 65$ in most cases, $N_z = 37$ in a few cases with $N_t = 6$. The lattice coupling constant β is in the range $2.25 \leq \beta \leq 2.40$ for $N_t = 4$, and $2.30 \leq \beta \leq 2.50$ for $N_t = 6$. We updated the lattice configurations by using the standard Metropolis algorithm alternated with overrelaxation methods. We typically thermalized the lattice configurations for 4000 sweeps, and made one measurement every 10 sweeps. The total number of measurements for each data set is about 2000. The actual number may vary by a small amount in each case. Table 2 gives an overview of the typical statistics of our measurements, which were performed on the lattice $4 \times 11^2 \times 65$. The label 'ovr' in the table represents the overrelaxation updating, and 'met' means Metropolis updating, 'mhit' means using multihit techniques, N_{therm} is the number of sweeps dropped for thermalization, N_{btw} is the number of sweeps between two measurements, $N_{mea.}$ means the number of total measurements. All calculations were done on LSU's IBM 3090 mainframe. In the following we proceed to discuss our measurements on lattices and present some raw data.

Table 2: The statistics of data on the lattice $4 \cdot 11^2 \cdot 65$.

$4 \cdot 11^2 \cdot 65$				
β	$mhit$	N_{therm}	N_{btw}	$N_{mea.}$
2.25	N	2000 ovr, 2000 met	2 ovr, 2 met	2100
2.25	Y	10000 ovr, 10000 met	5 ovr, 5 met	1800
2.28	N	1800 ovr, 1800 met	2 ovr, 2 met	1900
2.28	Y	5600 ovr, 5600 met	5 ovr, 5 met	2080
2.29	N	2000 ovr, 2000 met	2 ovr, 2 met	2300
2.29	Y	6600 ovr, 6600 met	5 ovr, 5 met	2000
2.30	N	2000 ovr, 2000 met	2 ovr, 2 met	2200
2.30	Y	6000 ovr, 6000 met	5 ovr, 5 met	2000
2.34	N	2000 ovr, 2000 met	2 ovr, 2 met	2300
2.34	Y	6000 ovr, 6000 met	5 ovr, 5 met	2000
2.36	N	2000 ovr, 2000 met	2 ovr, 2 met	2300
2.36	Y	6600 ovr, 6600 met	5 ovr, 5 met	2000
2.40	N	1800 ovr, 1800 met	2 ovr, 2 met	2200
2.40	Y	6400 ovr, 6400 met	5 ovr, 5 met	2000

(1). The Order Parameter $< |P| >$

On each lattice we measured the expectation of the modulus of the Polyakov loop $< |P| >$, which plays the role of the order parameter for the finite temperature phase transition on lattices[13, 23], where P is closed in the time direction, as defined in Eq. (2.27). We shall discuss this further in the next chapter. In Table 3 we show the measured values of $< |P| >$ on lattices $4 \cdot 9^2 \cdot 65$, $4 \cdot 11^2 \cdot 65$, $6 \cdot 7^2 \cdot 65$ and $6 \cdot 11^2 \cdot 37$. Here all data were measured by using multihit techniques.

(2). The Correlation $< P(0)P^{\dagger}(z) >$ and String Tension κ

We also measured the correlation function $< P(0)P^{\dagger}(z) >$, which enables us to study the $q\bar{q}$ potential $V(r)$ at various temperatures. In the

Table 3. The measured values of $< |P| >$ on lattices $4 \cdot 9^2 \cdot 65$, $4 \cdot 11^2 \cdot 65$, $6 \cdot 7^2 \cdot 65$ and $6 \cdot 11^2 \cdot 37$.

$N_t = 4$	$4 \cdot 9^2 \cdot 65$	$4 \cdot 11^2 \cdot 65$	$N_t = 6$	$6 \cdot 7^2 \cdot 65$	$6 \cdot 11^2 \cdot 37$
β	$< \|P\| >$	$< \|P\| >$	β	$< \|P\| >$	$< \|P\| >$
2.25	0.02638 (44)	0.02124 (38)	2.30	0.01269 (20)	0.01074 (18)
2.28	0.04009 (62)	0.03746 (56)	2.36	0.02214 (34)	0.01930 (30)
2.29	0.04655 (78)	0.04684 (74)	2.40	0.03921 (58)	0.03142 (58)
2.30	0.04443 (80)	0.04856 (78)	2.42	0.03476 (56)	0.05433 (76)
2.32	0.08365 (126)		2.45	0.04326 (72)	0.08517 (94)
2.34		0.17156 (160)	2.50	0.08406 (90)	0.14275 (48)
2.36	0.23603 (36)	0.23772 (32)			
2.40	0.27094 (30)	0.27182 (26)			

measurements we chose the correlation along the longest extent of the lattice, N_z.

As we mentioned in Chap. 1, in the confined phase the potential $V(r)$ of a $q\bar{q}$ pair is linear. The proportionality constant is the string tension κ, which can be extracted from the correlation, $< P(0)P^\dagger(z) >$, as follows[19],

$$< P(0)P^\dagger(z) >_c = const.(e^{-L_t\kappa z} + e^{-L_t\kappa(L_z - z)}), \tag{3.5}$$

where on the L.H.S. of this equation the connected correlation $< P(0)P^\dagger(z) >_c$ is defined as, $< P(0)P^\dagger(z) > - < P >^2$. So the dependence on the coordinates t, x, y can be suppressed, and one can extract the effective string tension. On the R.H.S. the new term $e^{-L_t\kappa(L_z - z)}$ accounts for the finite size effects along the correlation direction N_z, where $L_z = N_z a$.

From Eq. (3.5) we can calculate the string tension κ from the measured correlations $< P(0)P^\dagger(z) >_c$. In fact, one can obtain a string tension data at each separation z, as z is large enough. Table 4 gives an example of the measured data for various separations z. To get an estimate of the asymptotic

Table 4. The raw string tension data κ extracted from the correlation $< P(0)P^{\dagger}(z) >_c$ at different distance z, they were measured on the lattice $4 \cdot 11^2 \cdot 65$ with $\beta = 2.25$.

$4 \cdot 11^2 \cdot 65, \quad \beta = 2.25$	
z/a	$\sqrt{\kappa}a$
3	0.429 (3)
4	0.379 (7)
5	0.347 (12)
6	0.328 (20)
7	0.313 (32)
8	0.307 (48)
9	0.324 (68)
10	0.327 (103)

string tension ($z \rightarrow \infty$), we need to choose a data at appropriately large z, because as z becomes too large the data have very large uncertainties.

We find the measured string tension data are consistent within errors over a "relevant distance" range. Usually, the end of this range can be determined as following[19], if the data at a distance z is larger than its preceding one, i.e. the data at the distance $z-1$, then $z-1$ is a natural choice of the last relevant distance. For example, in Table 4 the last relevant distance is $8a$. The reason for such a choice is that the increase of data at large distances is in contradiction with general principles and here reflects that the inaccuracy of the data has become larger than the correction effects we would like to see. We then choose one of the first string tension data (and its error bar) in the "relevant distance" range as estimate of the asymptotic string tension κ ($z \rightarrow \infty$). In this range we usually choose the data with relatively small error bar. For instance, from Table 4 we extract the asymptotic string tension to be, $\sqrt{\kappa}a$ =0.313 (32), on the lattice $4 \cdot 11^2 \cdot 65$ with $\beta = 2.25$.

Table 5. The string tension data κ measured in lattice units on lattices of the size $4 \cdot 9^2 \cdot 65$, $4 \cdot 11^2 \cdot 65$, $6 \cdot 7^2 \cdot 65$ and $6 \cdot 11^2 \cdot 37$.

$N_t = 4$	$4 \cdot 9^2 \cdot 65$	$4 \cdot 11^2 \cdot 65$	$N_t = 6$	$6 \cdot 7^2 \cdot 65$	$6 \cdot 11^2 \cdot 37$
β	$\sqrt{\kappa}a$	$\sqrt{\kappa}a$	β	$\sqrt{\kappa}a$	$\sqrt{\kappa}a$
2.25	0.301 (38)	0.313 (32)	2.30	0.310 (48)	0.377 (27)
2.28	0.242 (33)	0.243 (29)	2.36	0.248 (21)	0.284 (13)
2.29	0.224 (17)	0.181 (33)	2.40	0.172 (30)	0.217 (17)
2.30	0.216 (19)	0.203 (17)	2.42	0.200 (17)	0.177 (41)

In Table 5 we list the extracted asymptotic string tension data κ measured in lattice units on lattices of the size $4 \cdot 9^2 \cdot 65$, $4 \cdot 11^2 \cdot 65$, $6 \cdot 7^2 \cdot 65$ and $6 \cdot 11^2 \cdot 37$. Again the multihit techniques were used.

In this table some string tension data were measured in the transition region, e.g. $\beta = 2.30$ for $(N_t = 4)$ (we shall explain this further in Chapter 4,), in this case we assume Eq. (3.5) is still valid. Since our lattices have the geometry, $N_z \gg N_s > N_t$, we find that finite size effects are small as $N_s/N_t \geq 2$ in the limit of $N_z \to \infty$. The detailed analysis of finite size effects is presented in Chapter 5. The results also agree with those of refs.[19, 31]. Therefore, we expect that the data measured on lattices $4 \cdot 9^2 \cdot 65$ and $4 \cdot 11^2 \cdot 65$ can be viewed as the string tension in the large volume limit. However, the data from the lattice $6 \cdot 7^2 \cdot 65$ might have some large finite size effects because $N_s = 7$ is not large enough (for $N_t = 6$). For data measured on the lattice $6 \cdot 11^2 \cdot 37$ the transverse size $N_s = 11$ may be large enough, but some large finite size effects may arise due to the relatively small N_z (i.e. $N_z = 37$). In the next Chapter we will discuss these finite size effects further.

(3). $q\bar{q}$ Flux Distributions

To measure the flux distributions of a $q\bar{q}$ pair, we calculated the quantity[24, 32],

$$f_{\mu\nu}(\vec{r},\vec{x}) = \frac{\beta}{a^4}\Big[\frac{< P(0)P^{\dagger}(\vec{r})\Box_{\mu\nu} >}{< P(0)P^{\dagger}(\vec{r}) >} - < \Box_{\mu\nu} >\Big], \tag{3.6}$$

where the Polyakov loop $P(\vec{r})$ is defined in Eq. (2.27), with N_t chosen to be the time direction. In this case the Polyakov loops P and $P^{\dagger}$ represent the $q\bar{q}$ sources. The plaquette is, $\Box_{\mu\nu} = \frac{1}{2}Tr(U_P)$, with U_P defined in Eq. (2.10), which plays the role of a 'test charge'. The plaquette has 6 different orientations, (μ,ν)=(2,3), (1,3), (1,2), (1,4), (2,4), (3,4).

Using Eq. (2.16) in the continuum limit ($a \rightarrow 0$), the plaquette $\Box_{\mu\nu}$ becomes,

$$\begin{aligned} \Box_{\mu\nu}(\vec{x},0) &= \frac{1}{2}trU_P(\vec{x},0), \\ &\approx \frac{1}{2}(2 - \frac{1}{2}a^4 g^2 Tr[F_{\mu\nu}^2]), \\ &\approx \frac{1}{2}(2 - \frac{1}{4}a^4 g^2 \sum_i (F_{\mu\nu}^i)^2), \end{aligned} \tag{3.7}$$

where $F_{\mu\nu}^i$ are the color components of the field strangth tensor, $F_{\mu\nu}$, defined in Eq. (2.2) with the color index $i = 1,2,3$ for $SU(2)$. Therefore, Eq. (3.6) becomes,

$$f_{\mu\nu} \xrightarrow{a\rightarrow 0} -\frac{1}{2} < \sum_i (F_{\mu\nu}^i)^2 >_{q\bar{q}-vac} . \tag{3.8}$$

with *vac* representing the vacuum. The R.H.S. of this equation is just the energy density of the color field $F_{\mu\nu}$ for the $q\bar{q}$ sources relative to the vacuum.

To decrease statistical noise and save CPU time three enhancements of the measurements were used in our calculations.

The first enhancement is that we measure the quantity[32]

$$f'_{\mu\nu}(\vec{r},\vec{x}) = \frac{\beta}{a^4}\left[\frac{< P(0)P^\dagger(\vec{r})\Box_{\mu\nu}(\vec{x}) > - < P(0)P^\dagger(\vec{r})\Box_{\mu\nu}(\vec{x}_R) >}{< P(0)P^\dagger(\vec{r}) >}\right], \qquad (3.9)$$

as the flux distribution instead of Eq. (3.6), where the reference point $\vec{x}_R$ was chosen to be far from the $q\bar{q}$ sources. This replacement does not change the measured average due to the cluster decomposition theorem[32]. Nevertheless the main fluctuations of the quantity $PP^\dagger\Box$, which are caused by the $PP^\dagger$ itself, cancel when the difference in Eq. (3.9) is computed configuration by configuration.

The second enhancement is to use the multihit technique[32] to improve the statistical accuracy. That is, we make the replacement for Polyakov loops in Eq. (3.9),

$$P(\vec{r}) \rightarrow \bar{P}(\vec{r}) = \frac{1}{2}Tr\prod_{\tau=1}^{N_t}\bar{U}_t(\vec{r},\tau), \qquad (3.10)$$

where $\bar{U}_t(\vec{r},\tau)$ is given by

$$\begin{aligned}\bar{U}_t &= \frac{\int U_t \exp[\beta tr(U_t X_t^\dagger + h.c.)]dU_t}{\int \exp[\beta tr(U_t X_t^\dagger + h.c.)]dU_t} \\ &= X_t\frac{I_2(\beta\lambda)}{\lambda I_1(\beta\lambda)}, \qquad (3.11)\end{aligned}$$

with $X_t^\dagger$ to be the neighborhood of U_t, i.e. $U_t X_t^\dagger = \sum \Box_P$, the sum extends over all plaquettes containing U_t. And $\lambda = \sqrt{det(X_t)}$, I_1 and I_2 are the modified Bessel functions.

The third enhancement was to use the vectorized fast Fourier transforms[33] in order to compute the convolutions implied by Eq. (3.9). In this way we have reduced the measurement time which was the major fraction of the required CPU time.

The six components of $f'_{\mu\nu}$ in Eq. (3.9) correspond to the components of the chromo-electric and chromo-magnetic fields $(\vec{\mathcal{E}}, \vec{\mathcal{B}})$ in Minkowski space, i.e.

$$\begin{aligned}
f_{23} &\rightarrow -\frac{1}{2} < \sum_i (\mathcal{B}_1^i)^2 > = -\frac{1}{2} < \mathcal{B}_1^2 >, \\
f_{13} &\rightarrow -\frac{1}{2} < \sum_i (\mathcal{B}_2^i)^2 > = -\frac{1}{2} < \mathcal{B}_2^2 >, \\
f_{12} &\rightarrow -\frac{1}{2} < \sum_i (\mathcal{B}_3^i)^2 > = -\frac{1}{2} < \mathcal{B}_3^2 >, \\
f_{14} &\rightarrow \frac{1}{2} < \sum_i (\mathcal{E}_1^i)^2 > = \frac{1}{2} < \mathcal{E}_1^2 >, \\
f_{24} &\rightarrow \frac{1}{2} < \sum_i (\mathcal{E}_2^i)^2 > = \frac{1}{2} < \mathcal{E}_2^2 >, \\
f_{34} &\rightarrow \frac{1}{2} < \sum_i (\mathcal{E}_3^i)^2 > = \frac{1}{2} < \mathcal{E}_3^2 > .
\end{aligned} \tag{3.12}$$

with $i = 1, 2, 3$ for $SU(2)$.

The total electric and magnetic energy densities are defined as

$$\begin{aligned}
\rho_{el} &= \frac{1}{2} < \mathcal{E}^2 > = \frac{1}{2}[< \mathcal{E}_1^2 > + < \mathcal{E}_2^2 > + < \mathcal{E}_3^2 >], \\
\rho_{ma} &= \frac{1}{2} < \mathcal{B}^2 > = \frac{1}{2}[< \mathcal{B}_1^2 > + < \mathcal{B}_2^2 > + < \mathcal{B}_3^2 >].
\end{aligned} \tag{3.13}$$

In the following we will concentrate on studying the total energy and action densities ρ_E and ρ_A, which are the combinations of ρ_{el} and ρ_{ma}, The total energy density is

$$\rho_E = \rho_{el} + \rho_{ma}, \tag{3.14}$$

The total action density is

$$\rho_A = \rho_{el} - \rho_{ma}. \tag{3.15}$$

We measured the flux distributions $f'_{\mu\nu}$ on various lattices, which cover the regions of both confined and unconfined phases. In Chapter 5 we will present the analysis our flux data.

CHAPTER 4

FINITE TEMPERATURE PHASE TRANSITION

In this chapter we shall review some propertities of the finite temperature phase transition for the $SU(2)$ gauge theory. Then we discuss some results of our data.

4.1 Basic Theory

The finite temperature physics of $SU(N)$ gauge theory can be studied very conveniently on the lattice. On a four-dimensional Euclidean lattice of the size, $N_t \cdot N_s^2 \cdot N_z$, the temperature T is related to the temporal extent of the lattice, as we described in Section 2.4. If one chooses N_t as the time direction, then the temperature can be defined by Eq. (2.47), i.e.

$$T = \frac{1}{N_t a}. \tag{4.1}$$

where a is the lattice spacing, which is a function of the lattice coupling constant β.

It is known for pure $SU(N)$ gauge theory that the expectation value of the Polyakov loop $< P >$ plays the role of an order parameter[13] for the finite temperature phase transition. Here the Polyakov loop P is closed in the time direction, as defined in Eq. (2.27). That is, in the infinite volume limit one has

in the confined phase, $T < T_c$, $< P >= 0$;

in the unconfined phase, $T > T_c$, $< P > \neq 0$;

because of the spontaneous breaking of the global Z_N symmetry[23], where T_c is the transition temperature. The global Z_N symmetry can be described as follows. Under the transformation of the Polyakov loop,

$$P(\vec{r}) \rightarrow e^{i2\pi k/N} P(\vec{r}), \tag{4.2}$$

the action of the $SU(N)$ gauge theory is invariant. Here $e^{i2\pi k/N}$ is an element of the Z_N group, with $k = 0, 1, \cdots, N-1$. This symmetry is spontaneously broken if $< P > \neq 0$.

The expectation value $< P >$ is associated with the free energy F_q of an isolated quark q in the infinite volume limit, as we discussed in section 2.2, the relation is given by Eq. (2.28), i.e.

$$| < P > | \sim e^{-L_t F_q}, \tag{4.3}$$

where $L_t = N_t a$, which is the inverse temperature. Further, the correlation function $< P(0)P^\dagger(r) >$ is related to the potential energy $V(r)$ of a $q\bar{q}$ pair, as shown in Eq. (2.29), i.e.

$$< P(0)P^\dagger(r) >= const.exp[-L_t V(r)]. \tag{4.4}$$

In the confined phase, $T < T_c$, one expects Eq. (4.4) becomes as $r \rightarrow \infty$[12],

$$\begin{aligned} \lim_{r\to\infty} < P(0)P^\dagger(r) > &= \lim_{r\to\infty} const.exp[-L_t \kappa r] \\ &= < P >^2 = 0, \end{aligned} \tag{4.5}$$

because of $< P >= 0$ in the confined phase, where κ is the string tension. Eq. (4.5) implies that the $q\bar{q}$ potential in the confined phase is linear, e.g. $V(r) \sim \kappa r$. This causes quark confinement in the confined phase.

In the unconfined phase, $T > T_c$, one has that for $SU(2)$ gauge theory Eq. (4.4) becomes as $r \to \infty$[12],

$$\begin{aligned} \lim_{r\to\infty} < P(0)P^{\dagger}(r) > &= \lim_{r\to\infty} const.[1 + L_t \frac{3}{\beta 4\pi r} exp(-mr)] \\ &\approx < P >^2 \neq 0, \end{aligned} \tag{4.6}$$

for $< P > \neq 0$ in the unconfined phase. Eq. (4.6) implies that the $q\bar{q}$ potential in the unconfined phase is a screened Coulomb potential, e.g. $V(r) \sim \frac{e^{-mr}}{r}$ with m^{-1} the Debye screening length. To the lowest order of perturbation theory one has[12]

$$m^2 = \frac{2}{3} g^2 T^2. \tag{4.7}$$

Ref.[34] gives a detailed discussion about the $q\bar{q}$ potential in the unconfined phase. We shall not discuss it in the following.

The transition temperature T_c can be determined by Monte Carlo calculations. For $SU(2)$ one recent result is[35, 36],

$$\beta_c = 2.2985 \pm 0.0006. \qquad (\text{for } N_t = 4) \tag{4.8}$$

This transition point β_c was calculated on large lattices (e.g. 4×26^3), on which finite size effects are small, the result can be considered to be the transition point in the infinite volume limit.

By using the scaling relation in Eqs. (2.33) and (2.34) one can calculate the transition temperature T_c in physical units from Eqs. (4.1) and (4.8).

The result is,

$$\begin{aligned} T_c\Lambda_L^{-1} &= \frac{1}{N_t f(\beta_c)}, \\ &= 42.11 \pm 0.06. \end{aligned} \tag{4.9}$$

This is consistent with the result of ref.[19]. If we substitute the value of $\Lambda_L^{-1}(\beta_c)$ in Eq. (2.34), we can obtain the transition temperature T_c in physical units,

$$T_c = 1.487 \pm 0.140 \quad (1/fm), \tag{4.10}$$

which corresponds to $T_c = 293 \pm 28\ Mev$. This result was calculated in the static quark approximation. If we consider the effects of dynamical quarks, this result will change[10].

From the scaling relation $a(\beta)$ of Eqs. (2.33) and (2.34) one can also estimate the transition point β_c on lattices of any temporal size N_t for $SU(2)$ gauge theory, if we assume the transition temperature T_c in Eq. (4.9) is independent of the lattice size, for example, the estimated value of β_c for $N_t = 6$ and 8 are

$$\begin{aligned} \beta_c &\simeq 2.42 \qquad (\text{for } N_t = 6), \\ \beta_c &\simeq 2.50 \qquad (\text{for } N_t = 8). \end{aligned} \tag{4.11}$$

In the following we proceed to discuss some results in our study of the finite temperature phase transition on lattices.

4.2 Data Analysis

(1). Results of The Order Parameter $< |P| >$

As we discussed above, the expectation $< P >$ plays the role of an order parameter in the infinite volume limit. However, on a finite lattice this quantity is always zero if the computation time is taken to be infinite, because the system would flip between two ordered states, and the values of the Polyakov loop P would flip sign after some iterations. Therefore, one chooses the expectation value of the modulus of the Polyakov loop $< |P| >$ as the "order parameter" on finite lattices[13, 23].

The measured data of $< |P| >$ are listed in Table 3. We then plotted $< |P| >$ versus β in Fig. 6, which shows that there is a rapid increase of $< |P| >$ at $\beta \approx 2.30$ for $N_t = 4$, and another rapid increase at $\beta \approx 2.42$ for $N_t = 6$. This implies that a phase transition occurs at $\beta_c \approx 2.30$ for $N_t = 4$, or $\beta_c \approx 2.42$ for $N_t = 6$, in the infinite volume limit. These results agree with Eqs. (4.8) and (4.11). For cases of $N_t = 4$ the data measured on the lattice $4 \cdot 9^2 \cdot 65$ agree very well with those from $4 \cdot 11^2 \cdot 65$, both approach the infinite volume limit. However, for cases of $N_t = 6$ the data from the lattice $6 \cdot 7^2 \cdot 65$ have some discrepencies with the data from $6 \cdot 11^2 \cdot 37$. This may be due to finite-volume effects, as discussed in ref. [35], because in these cases N_s (or N_z) are not large enough to approach the infinite volume limit.

(2). Results of The Correlation $< P(0)P^\dagger(z) >$

Since the correlation $< P(0)P^\dagger(z) >$ is related to the $q\bar{q}$ potential energy $V(r)$, as shown in Eq. (4.4), we then measured the correlation on each

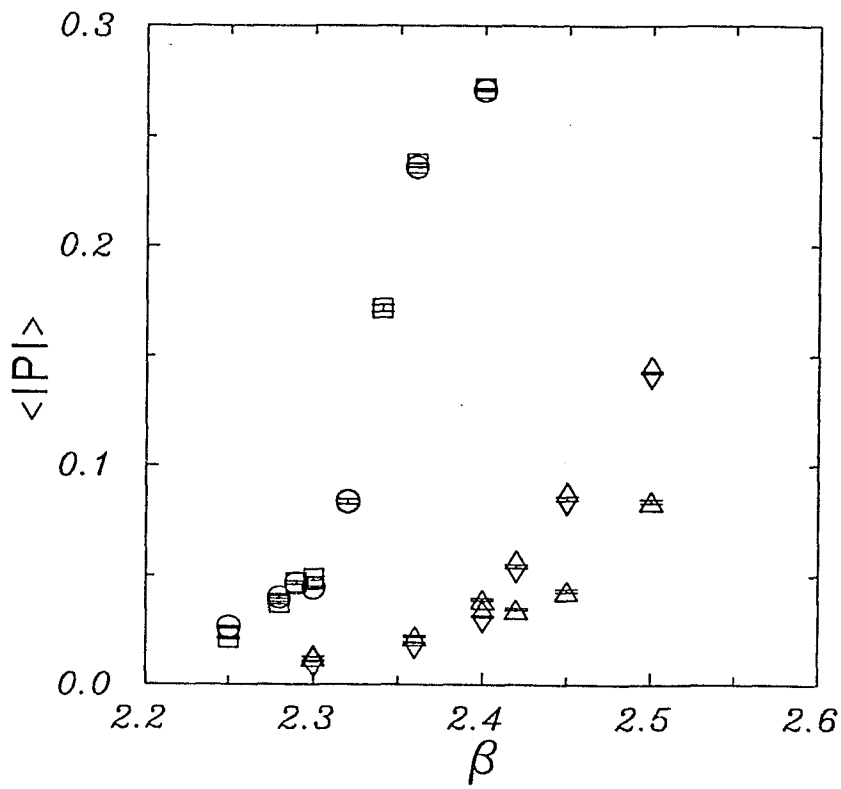

Figure 6. Monte Carlo data for $< |P| >$ vs. β, calculated from lattices of size $4 \cdot 9^2 \cdot 65$ (circles), $4 \cdot 11^2 \cdot 65$ (squares), $6 \cdot 7^2 \cdot 65$ (triangles) and $6 \cdot 11^2 \cdot 37$ (diamonds).

lattice. Some typical results are shown in Figs. 7 and 8. Fig. 7 shows $< P(0)P^{\dagger}(r) >$ versus r in the confined phase, Fig. 7 (a) shows the results in a linear plot. Fig. 7 (b) was drawn as a logarithmic plot. Fig. 8 is similar to Fig. 7, but in the unconfined phase. From Fig. 7 one can see that the correlation $< P(0)P^{\dagger}(r) > \rightarrow 0$ as $r \rightarrow \infty$, and $ln < P(0)P^{\dagger}(r) >$ is linear with r. This implies that the $q\bar{q}$ potential $V(r)$ is linear in the confined phase, as predicted by Eq. (4.5). The slope of the straight lines in Fig. 7 (b) corresponds to the string tension κ, which shows that the string tension decreases with β (or temperature). Fig. 8 shows that in the unconfined phase the correlation $< P(0)P^{\dagger}(r) > \not\rightarrow 0$ as $r \rightarrow \infty$, which is consistent with the prediction of Eq. (4.6).

(3). Behaviour of κ with Temperature

The measured string tension data are listed in Table 5, which are in lattice units. We can use the scaling relation of of Eqs. (2.33) and (2.34) to transform the string tension data from lattice units to physical units. The results are shown in Table 6. From this table one can see that the string tension κ decreases with the temperature T (or β) in the confined phase. If we assume that κ is a continous function of T (or β), one has

$$\begin{aligned} &\frac{\partial \kappa}{\partial T} < 0 \qquad (\text{for } T < T_c), \\ &\frac{\partial \kappa}{\partial \beta} < 0 \qquad (\text{for } \beta < \beta_c). \end{aligned} \tag{4.12}$$

This behavior is also confirmed by some recent works[37, 38]. In the following we proceed to study this behaviour of κ in further detail.

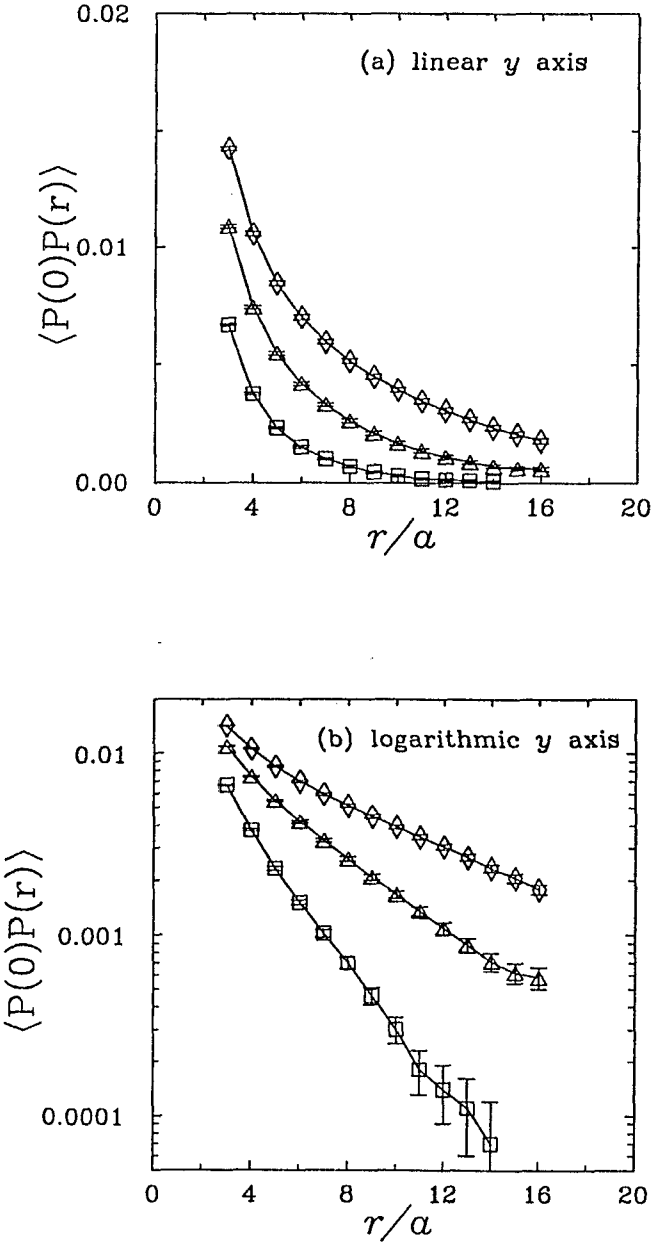

Figure 7. Monte Carlo data of $< P(0)P(r) >$ vs. r/a in the confined phase, calculated on the lattice of size $4 \cdot 11^2 \cdot 65$ with $\beta = 2.25$ (squares), $\beta = 2.28$ (triangles) and $\beta = 2.29$ (diamonds). (a). linear axies, (b). logarithmic y axes and linear x axes.

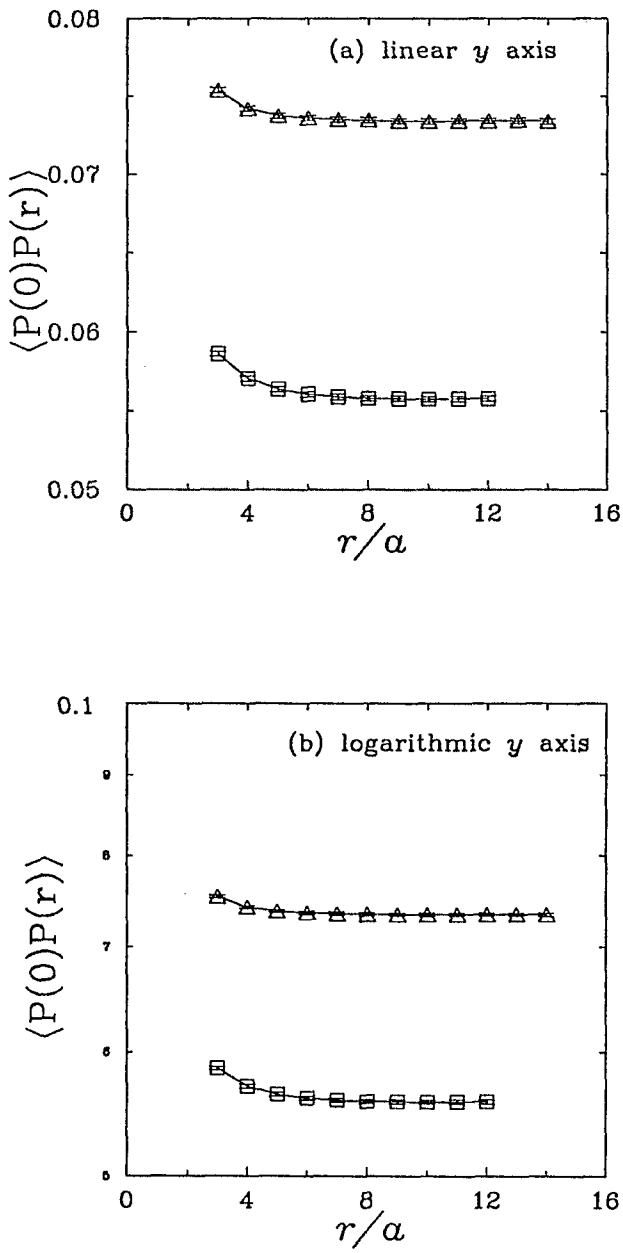

Figure 8. Monte Carlo data of $< P(0)P(r) >$ vs. r in the unconfined phase, calculated on the lattice $4 \cdot 9^2 \cdot 65$ with $\beta = 2.36$ (squares) and $\beta = 2.40$ (triangles). (a). linear axies, (b). logarithmic y axes and linear x axes.

Table 6. The string tension data κ measured in physical units on lattices of the size $4 \cdot 9^2 \cdot 65$, $4 \cdot 11^2 \cdot 65$, $6 \cdot 7^2 \cdot 65$ and $6 \cdot 11^2 \cdot 37$.

$N_t = 4$			$4 \cdot 9^2 \cdot 65$	$4 \cdot 11^2 \cdot 65$
β	$T\Lambda_L^{-1}$	$T\ (1/fm)$	$\kappa\ (Gev/fm)$	$\kappa\ (Gev/fm)$
2.25	37.29	1.271	0.462 (117)	0.499 (102)
2.28	40.20	1.401	0.362 (99)	0.365 (87)
2.29	41.22	1.447	0.331 (50)	0.216 (79)
2.30	42.27	1.494	0.328 (58)	0.290 (49)
$N_t = 6$			$6 \cdot 7^2 \cdot 65$	$6 \cdot 11^2 \cdot 37$
β	$T\Lambda_L^{-1}$	$T\ (1/fm)$	$\kappa\ (Gev/fm)$	$\kappa\ (Gev/fm)$
2.30	28.18	0.996	0.677 (210)	1.001 (143)
2.36	32.76	1.213	0.642 (109)	0.842 (77)
2.40	36.23	1.386	0.403 (141)	0.641 (100)
2.42	38.10	1.482	0.623 (106)	0.488 (226)

Since the string tension κ decreases with the temperature T in the confined phase and vanishes in the unconfined phase, we expect that in the confined phase κ approach zero as $T \rightarrow T_c$. For simplicity, we then use the simple function with power behavior to fit the string tension near T_c, that is,

$$\kappa(T) = \kappa_0(1 - \frac{T}{T_c})^{\alpha} \qquad (\text{for } T < T_c). \tag{4.13}$$

This is a simplified form of the fitting function used in ref. [38]. Here the constant κ_0 corresponds to the string tension κ in the limit of zero temperature and infinite volumes, which is given by Eq. (2.32), i.e. $\kappa_0 \approx 0.981\ Gev/fm$. The transition temperature T_c is given by Eq. (4.10) in physical units.

As we discussed in section 3.2, the string tension data measured on lattices $6 \cdot 7^2 \cdot 65$ and $6 \cdot 11^2 \cdot 37$ may have large finite size effects. By viewing the data in Table 6 we find that the string tension data from the lattice $6 \cdot 7^2 \cdot 65$ are consistent with the data from lattices $4 \cdot 9^2 \cdot 65$ and $4 \cdot 11^2 \cdot 65$, on which finite size effects can be neglected[39]. However, data from the lattice $6 \cdot 11^2 \cdot 37$ have

large discrepancies from the above data. This shows that finite size effects on string tension data are sensitive to the longitudinal size N_z, but not as much to the transverse size N_s.

We then use the string tension data from lattices of small finite size effects (i.e. $4 \cdot 11^2 \cdot 65$ and $6 \cdot 7^2 \cdot 65$), to fit the function in Eq. (4.13). The only fitting parameter is the exponential index α, the best fit result is,

$$\alpha = 0.35 \pm 0.04. \tag{4.14}$$

Fig. 9 shows this fitting function and the measured string tension data of small finite size effects. In this figure one can see that a few data point very close to the transition point T_c have large discrepancies from the fitting function, because fluctuations are large in the transition region. We then excluded these data at, $T \approx 1.48$ (1/fm), from our fitting process. Also all other data above T_c were excluded because they would correspond to complex values for the fitting function. Below the transition region our data agree very well with the conjectured behavior in Eq. (4.13).

To get the relation between κ and β with fixed N_t, we also fit the string tension data with the following function similar to Eq. (4.13),

$$\kappa(\beta) = \kappa_0(1 - \frac{\beta}{\beta_c})^\delta \qquad (\text{for } \beta < \beta_c). \tag{4.15}$$

We then choose the transition point $\beta_c = 2.2985 \pm 0.0006$ for $N_t = 4$ from Eq. (4.8), and $\beta_c = 2.42 \pm 0.01$ for $N_t = 6$ from Eq. (4.11). We find that the best fit for the exponential index δ in Eq. (4.15) is

$$\begin{aligned} \delta &= 0.22 \pm 0.03 \qquad (\text{for } N_t = 4), \\ \delta &= 0.14 \pm 0.04 \qquad (\text{for } N_t = 6). \end{aligned} \tag{4.16}$$

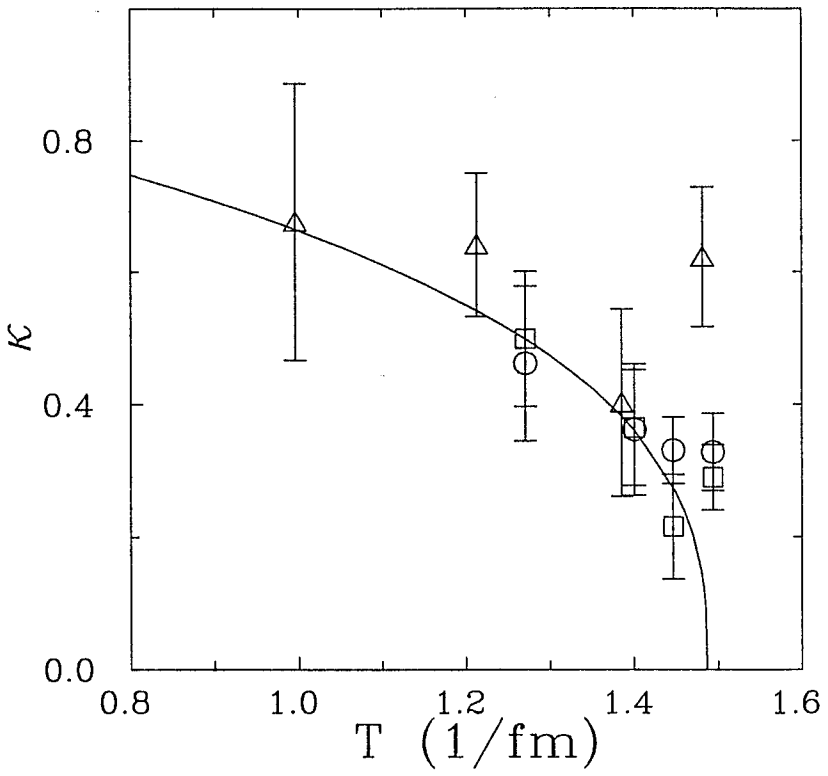

Figure 9. The plot of κ vs. T near the transition point T_c. The data were calculated on lattices, $4 \cdot 9^2 \cdot 65$ (circles), $4 \cdot 11^2 \cdot 65$ (squares) and $6 \cdot 7^2 \cdot 65$ (triangles). The solid line is the fitting function in Eq. (4.12) with $\alpha = 0.35 \pm 0.04$. The string tension κ is in the physical unit Gev/fm.

In Fig. 10 we plot the fitting function of Eq. (4.15) and our measured string tension data for $N_t = 4$. In this fugure the two data measured at $\beta = 2.30$ were excluded from fitting, which are just above the transition point, $\beta_c = 2.2985$. Again the data agree well with the fitting function. In Chapter 6 we shall use these relations to study Michael sum rules.

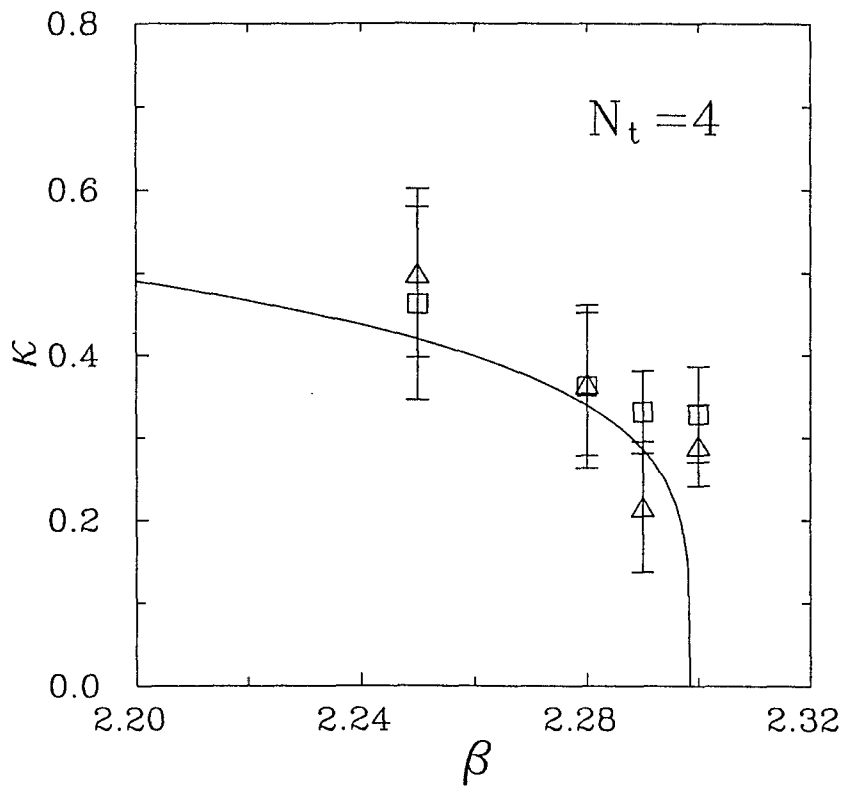

Figure 10. κ vs. β for $N_t = 4$, the transition point $\beta_c \sim 2.2985$. The data were calculated on lattices, $4 \cdot 9^2 \cdot 65$ (squares), $4 \cdot 11^2 \cdot 65$ (triangles). The solid line is the fitting function in Eq. (4.14) with $\delta = 0.22 \pm 0.03$. The string tension κ is in the physical unit Gev/fm.

CHAPTER 5

FLUX DISTRIBUTIONS

5.1 Motivations

As we discussed in Chapter 1, there are two complementary ways to obtain approximate solutions of strong coupling QCD. One is to take 3-space to be a finite volume torus and obtain semi-analytic solutions[14, 15, 17] of an effective Hamiltonian. The second is via lattice simulations. Confinement can be studied by each method in limited domains. In small physical volumes the fields are very rigid and the problem can be treated using a variational method applied to a small number of dynamical variables. In this domain the string tension is found to be zero. This result is consistent with asymptotic freedom since only short wavelength modes occur. At intermediate volumes there is a clear signal for string tension and further that it is a consequence of a tunneling amplitude between the vacua that are degenerate for small volumes. In this domain, lattice methods are also accessible and are in good agreement for quantities such as glueball masses and string tension. Lattice calculations can take over to study larger volumes where semi-analytic methods become prohibitive.

The existence of string tension in finite volumes does not imply confinement. Clearly if the volume is not large enough to allow the fields to spread out, the finite box itself may be responsible for the linearly rising potential energy between quarks. Global studies have left open the question of the volume

at which intrinsic confinement takes over[19]. In this Chapter we look at a local quantity, the flux tube profile between static quarks as a function of physical volume in SU(2) lattice gauge theory in order to elucidate this question.

M. Lüscher studied QCD in a small box, $z_g \leq 1$, with periodic boundary conditions, where the parameter z_g is defined in Eq. (1.4). He derived a low-energy effective Hamiltonian for SU(N) gauge theory in small volumes[14] (i.e. $z_g \leq 1$). Subsequently the lowest energy levels of SU(2)[15] and SU(3)[16] gauge theories in small volumes were computed by using this Hamiltonian. van Baal and Koller then found that the crucial tunneling between degenerate vacua can be obtained by imposing appropriate nonperturbative boundary conditions on the Raleigh-Ritz trial wave functions[17]. They extended the calculation of the SU(2) glueball masses up to $z_g \approx 5.0$.

Berg and Billoire[19] carried out a thorough study of glueball masses, electric flux states, and string tension for intermediate volumes ($i.e. 1 \leq z_g \leq 5$) on lattices. They provided a detailed comparison between their numerical results and the analytic results of van Baal and Koller. They chose lattice sizes $N_t \times N_s^2 \times N_z$, with

$$N_t \leq N_s \ll N_z. \tag{5.1}$$

By identifying N_z to be the time extent, one can simulate the zero temperature finite volume, $N_t N_s^2 a^3$, field theory. As we discussed in Sec. 2.4, in this case the temperature can be defined as

$$T_B = \frac{1}{N_z a}, \tag{5.2}$$

where T_B is called *box temperature* in ref.[19].

Physically, the choice of the time direction is related to interpreting Polyakov loop correlations as the $q\bar{q}$ potential; then the time direction is the

one in which the Polyakov loop closes. In our study we follow Berg and Billoire to choose Polyakov loops closed in the N_t direction and their correlations measured along the N_z direction. Then the *physical temperature* is defined to be

$$T_p = \frac{1}{N_t a}. \tag{5.3}$$

where T_p is same as the definition of T in Eqs. (2.47) and (4.1). In the following we shall keep using the physical temperature (T_p) interpretation, so we shall drop the subscript p, i.e. $T = T_p$. In the last section of this chapter we shall relate this to the box temperature (T_B) interpretation.

After a complete study in the intermediate volume region ($1 < z_g < 5$), Berg and Billoire concluded that they did not find evidence for string formation in this region, but it is expected to occur in larger volumes. The question is how to understand the string tension measured in intermediate volumes. Is the string tension just due to finite size effects? Since the string tension was calculated from correlations of Polyakov loops closed in the N_t direction, this can be considered as measuring the potential energy of a $q\bar{q}$ pair in a long rectangular box, with the volume $V = N_s^2 N_z a^3$ and at the finite temperature $T = 1/N_t a$, as shown in Fig. 11. As we know, at high temperatures, $T > T_c$, where T_c is the deconfining temperature, the $q\bar{q}$ is unconfined in the infinite volume limit (N_s, $N_z \rightarrow \infty$). However, as the transverse size N_s is made small, i.e. $r/N_s a \geq 1$, one expects the side walls of the box would squeeze the flux lines of the $q\bar{q}$ pair to form a tube although there is no intrinsic string formation in this case, as displayed in Fig. 11. In the following we will present our studies about the $q\bar{q}$ flux distributions which would support the above description.

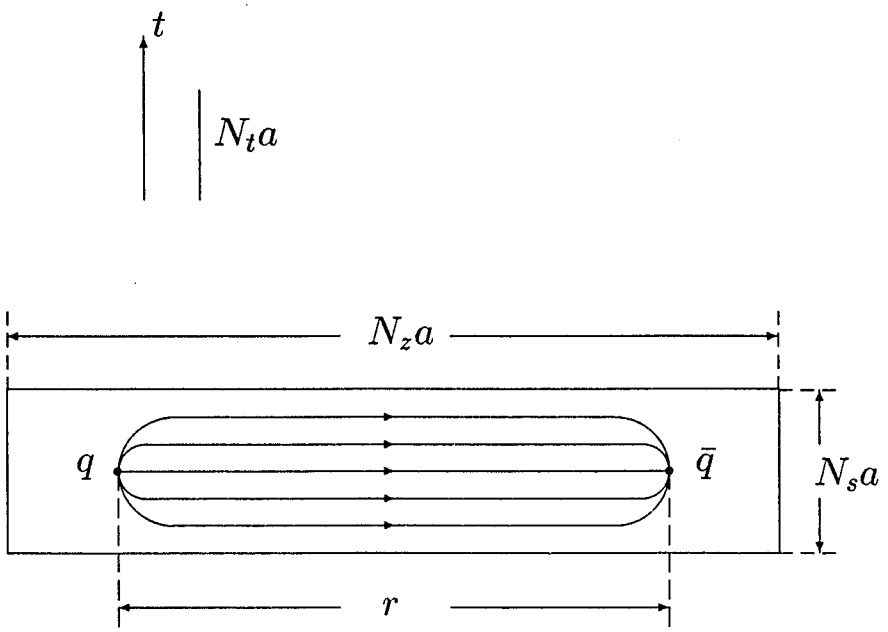

Figure 11. The $q\bar{q}$ color sources in a long rectangular box. The flux lines between the $q\bar{q}$ pair are confined by side walls and have a flux tube form.

5.2 Flux Distributions at Finite Temperatures

By calculating the quantity $f'_{\mu\nu}$ in Eq. (3.9) we measured the $q\bar{q}$ flux distributions on lattices $N_t \cdot N_s^2 \cdot N_z$ with $N_t = 4$, $N_s = 5$, 7, 9 and 11, and $N_c = 65$. We then transformed the flux data from lattice units to physical units by using the scaling relation of Eqs. (2.33) and (2.34). As we discussed in Chapter 4, $SU(2)$ gauge theory has a deconfining phase transition at the critical point, $\beta_c \approx 2.30$ for $N_t = 4$, in the infinite volume limit, i.e. N_s, $N_z \to \infty$. For $\beta < \beta_c$, the system is in the confined phase, otherwise, it is in the unconfined phase.

Since our lattices satisfy, $N_z \gg N_t$, N_s, as N_s/N_t gets large, we expect the system to approach the infinite volume limit and one should see the two phases. However, for N_s small, that is, N_s satisfying the condition,

$$N_s \simeq N_t, \qquad \text{and} \quad N_s a/r \leq 1, \tag{5.4}$$

the $q\bar{q}$ pair is in a finite box and one expects finite volume effects to be large. In the following we will study the flux distributions with $\beta > \beta_c$ and $\beta < \beta_c$ in various spacial volumes respectively.

(1). Flux Distributions with $\beta > \beta_c$

In this case the $q\bar{q}$ system approaches the unconfined phase as the volume becomes large ($N_s \to \infty$), we expect that there is no string formation. However, for a small volume one expects finite volume effects to be large.

In Fig. 12 we show some typical results of the energy density ρ_E distributions in the region of $\beta > \beta_c$ ($\beta = 2.40$), where ρ_E is defined in Eq. (3.9). They are the flux distributions on the transverse plane midway between the $q\bar{q}$ sources with fixed separation $r = 4a$, and they were measured on lattices of 4

different spatial sizes N_s=5, 7, 9, 11. For N_s small (i.e. N_s=5, 7) the transverse plane is the whole lattice. For large N_s (N_s=9, 11) the data are truncated on the margins. The signal is lost in the noise beyond the region shown.

From Fig. 12 we can compare the flux distributions in boxes of different transverse size N_s. One can clearly see for N_s small the flux density ρ_E at the edges of each plane have large values, as shown in Figs. 12 (a) and 12 (b). This implies that finite volume effects are significant when N_s is small because in small volumes flux lines of the $q\bar{q}$ sources would be squeezed dramatically by side walls of the box, so the values of ρ_E at edges are large in this case. As we increase the transverse size N_s finite volume effects become smaller, the flux density ρ_E at edges decrease rapidly to zero, as shown in Figs. 12 (c) and 12 (d).

Here we want to emphasize that the values of ρ_E at the edges of each plane are not due to the reference point in Eq. (3.9). In our flux measurement we choose the reference point $\vec{x}_R$ far from the $q\bar{q}$ sources, and we find the reference value $< P(0)P^\dagger(\vec{r})\Box_{\mu\nu}(\vec{x}_R) >$ in Eq. (3.9) is consistent with the product $< P(0)P^\dagger(\vec{r}) >< \Box_{\mu\nu} >$ within errors.

In Table 7 we list the typical values of flux densities ρ_E, ρ_A at edges of each plane in Fig. 12 and their corresponding errors. From this table one can explicitly see that the values ρ_E and ρ_A at edges decrease rapidly with N_s, as we observed from Fig. 12. However, we also notice that even in cases of large N_s (i.e. N_s=9, 11) the values of ρ_A shown are non-zero within errors. This may be caused by a number of factors. The edge of the plane is not the boundary of the lattice for cases of N_s=9, 11, the flux values may in fact vanish on the boundary of the lattice, but we did not calculate them there for

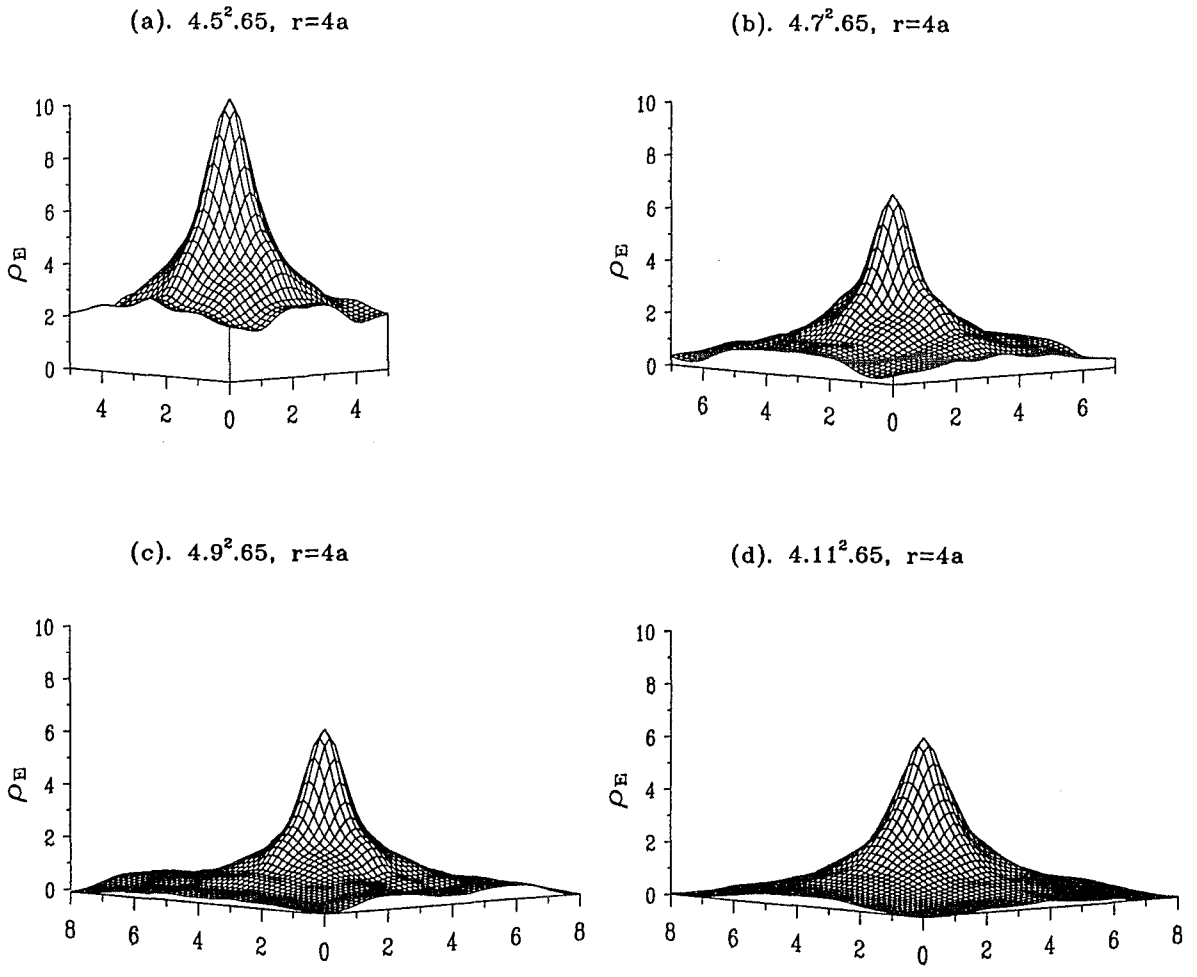

Figure 12. The energy density ρ_E flux distributions in the region of $\beta > \beta_c$. The flux data were measured on lattices $4 \cdot N_s^2 \cdot 65$ with $\beta = 2.40$ for various spatial sizes, (a) $N_s = 5$, (b) $N_s = 7$, (c) $N_s = 9$, and (d) $N_s = 11$. The data are in the physical unit Gev/fm^3.

Table 7. The typical measured flux density values (errors) of ρ_E and ρ_A in the region of $\beta > \beta_c$ on the edges of the transverse plane midway between the $q\bar{q}$, as shown in Fig. 5.2. The flux data are in the physical unit Gev/fm^3.

$4 \cdot N_b^2 \cdot 65$					
$r = 4a$	N_s	5	7	9	11
$\beta = 2.40$	ρ_E	2.5 (5)	0.86 (24)	0.11 (18)	0.31 (17)
	ρ_A	17.0 (6)	2.9 (3)	1.5 (2)	1.0 (2)

practical reasons. Also N_s is perhaps not large enough (even for $N_s = 11$), so there are still some small finite volume effects. Finally our error bars were only calculated from statistical error, the actual errors may be larger due to systematic errors.

To see the behavior of the flux distributions changing with the $q\bar{q}$ separation r, in Fig. 13 we show the ρ_A distribution on the transverse plane for 4 different separations, $r = 3a$, $4a$, $5a$ and $6a$. The flux data were measured on the lattice $4 \cdot 5^2 \cdot 65$ with $\beta = 2.40$. From this figure one can see the peak values of ρ_A decrease rapidly with the increase of r. At large r (i.e. $r = 6a$) the peak of ρ_A almost vanishes, the flux density on the plane approaches a uniform distribution.

We then calculated the center slice energy σ_E and action σ_A from our flux data, which are the energy and action stored in the transverse slice of unit thickness midway between the $q\bar{q}$ pair. The results are shown in Fig. 14. In this figure we plot the behaviors of σ_E versus. r and σ_A versus. r respectively for $\beta = 2.36$. This shows that for N_s small σ_E and σ_A do not decrease to zero as r increases. However, for N_s large (e.g. $N_s = 9$, 11), σ_E and σ_A decrease rapidly with r and become very small at large $q\bar{q}$ separations (i.e. $r = 6a$).

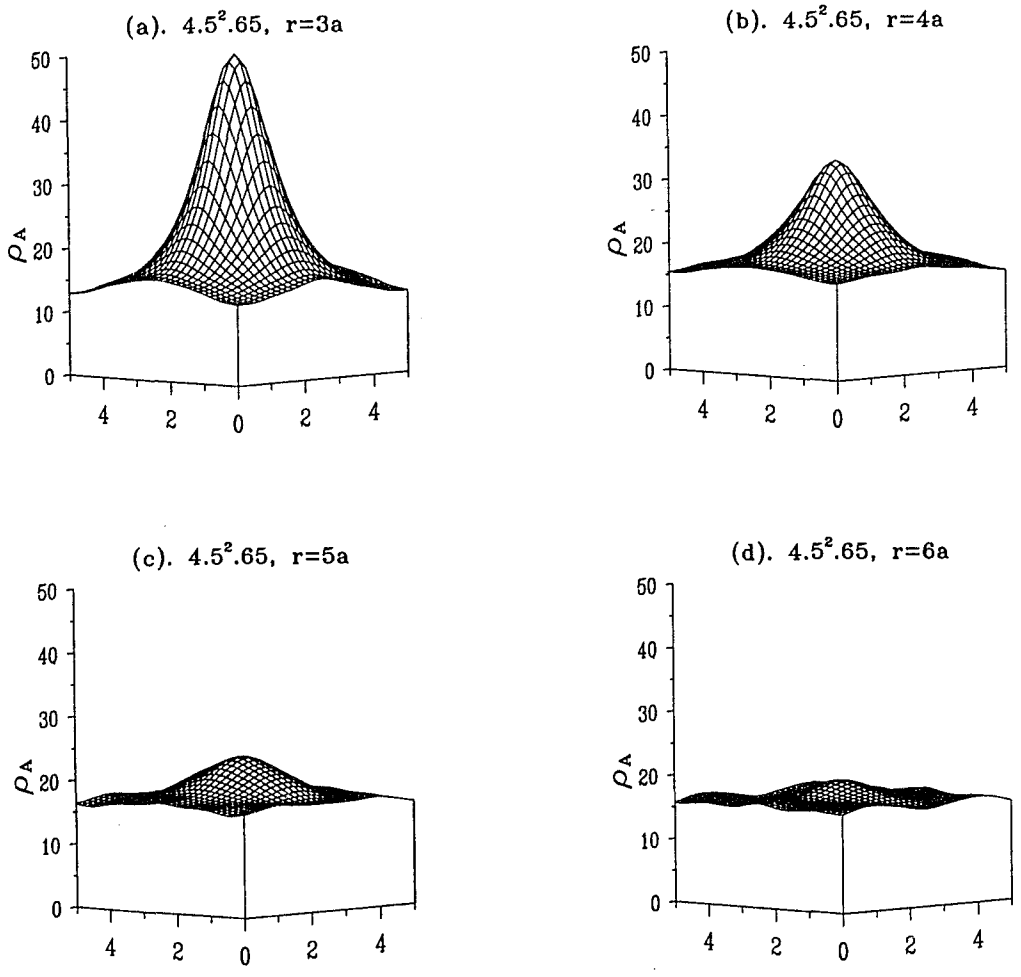

Figure 13. The action density ρ_A flux distributions in the region $\beta > \beta_c$, with the $q\bar{q}$ separations, (a) $r = 3a$, (b) $r = 4a$, (c) $r = 5a$ and (d) $r = 6a$. The data were measured on lattices $4 \cdot 5^2 \cdot 65$ with $\beta = 2.40$, and in the physical unit Gev/fm^3.

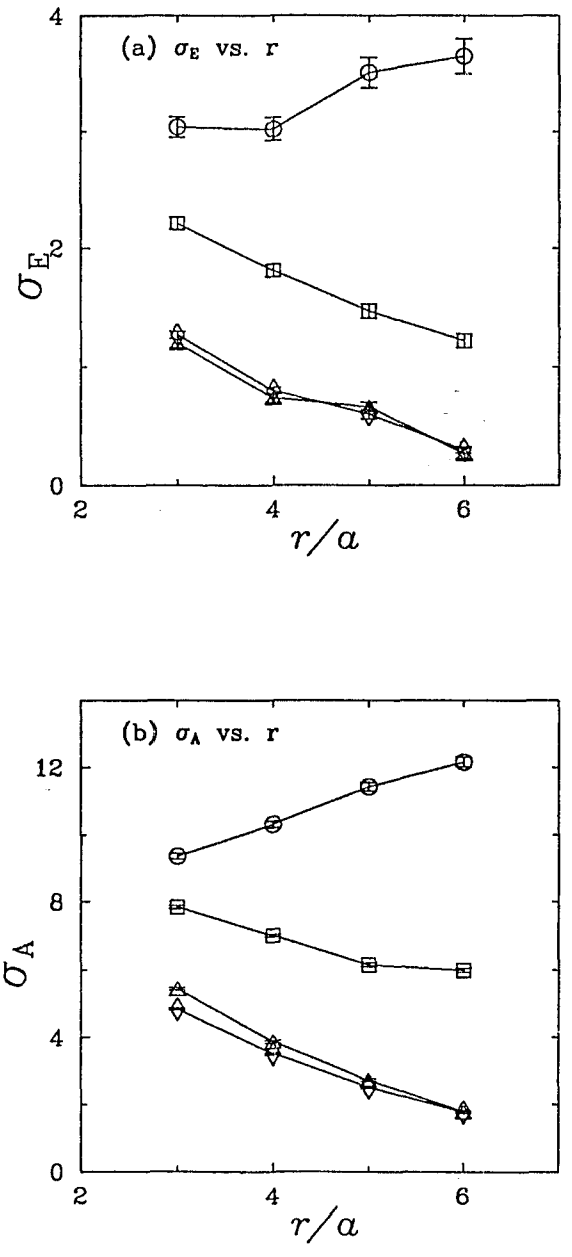

Figure 14. The center slice energy σ_E and action σ_A versus the $q\bar{q}$ separation r in the region of $\beta > \beta_c$, (a) σ_E vs. r, (b) σ_A vs. r. The data were measured on lattices $4 \cdot N_s^2 \cdot 65$ with $\beta = 2.36$ for various spatial sizes, $N_s = 5$ (circles), $N_s = 7$ (squares), $N_s = 9$ (triangles), $N_s = 11$ (diamonds). The data are in the physical unit Gev/fm.

(2). Analysis Of Finite Volume Effects For Cases $\beta > \beta_c$

To see how the finite volume effects influence $q\bar{q}$ flux distributions in a finite box, let us consider an electrostatic charge pair $+e$, $-e$ enclosed in a similar long rectangular box such as that of Fig. 11. The interaction between charges is the Coulomb interaction $V(r) \sim 1/r$. As the charge separation r becomes very large, i.e. $r/N_s a \to \infty$, one can assume that the electric field $\vec{\mathcal{E}}$ on the middle transverse plane is uniform, and can be written as

$$\mathcal{E} = \frac{\Phi}{(N_s a)^2}, \tag{5.5}$$

where Φ is electric flux through the transverse plane, which is a constant for the Coulomb interaction, and $(N_s a)$ is the transverse size of the box. So the total electric field energy on the transverse plane is

$$(\sigma_E)_C = \frac{1}{2}\mathcal{E}^2 (N_s a)^2 \sim \frac{1}{(N_s a)^2}. \tag{5.6}$$

This shows that at large charge separations the center slice energy $(\sigma_E)_C$ decreases with the behavior $(N_s a)^{-2}$ as the transverse size N_s increases, and $(\sigma_E)_C$ vanishes as $N_s \to \infty$, where the label 'C' denotes a Coulomb interaction.

Now let us return to the $q\bar{q}$ pair in the box with $\beta > \beta_c$. As we discussed in the above section, the system approaches the unconfined phase for large N_s. In this phase the $q\bar{q}$ interaction is a screened Coulomb interaction $V(r) \sim e^{-mr}/r$ with m the screening mass[12], as we discussed in Sec. 4.1. Then if the $q\bar{q}$ pair is put in a box such as that in Fig. 11, the flux Φ through the transverse plane is not a constant, but would decrease with r and N_s. So we expect that in this case the center slice energy σ_E for a $q\bar{q}$ pair would decay faster with N_s than $(\sigma_E)_C$, which has the inverse square behavior, $(\sigma_E)_C \sim (N_b a)^{-2}$, for $r \to \infty$. In Fig. 15 we plot our σ_E data versus the transverse size

N_s for large $q\bar{q}$ separation r. Our data are compared with the Coulomb behavior $(N_s a)^{-2}$ and for reference purposes the inverse quartic behavior $(N_s a)^{-4}$. The data were measured on lattices $4 \cdot N_s^2 \cdot 65$ with N_s =5, 7, 9, 11 and $\beta = 2.40$.

From Fig. 15 one can see that for large r our σ_E data appear to decay faster with N_s than the Coulomb behavior $(N_s a)^{-2}$ as expected. This shows us that the $q\bar{q}$ interaction in the unconfined phase at least contains a term that decays faster than the Coulomb interaction, such as the screened Coulomb interaction, although the data are not good enough to determine the screening mass.

In conclusion, our flux data in the region of $\beta > \beta_c$ show that in the unconfined phase there is no string formation. For a small transverse size N_s, the finite volume effects are large, the flux lines between a $q\bar{q}$ would be squeezed by side walls of the box significantly. This would result in a finite string tension.

(3). Flux Distributions with $\beta < \beta_c$

For $\beta < \beta_c$ the $q\bar{q}$ system approaches the confined phase as the volume becomes large ($N_s \rightarrow \infty$). We expect string formation would occur in this phase. To see this we need to study behaviors of the flux distributions as a function of the $q\bar{q}$ separation r.

In Fig. 16 we show the action density ρ_A distribution changing with the $q\bar{q}$ separation r. The flux data were measured on the lattice $4 \cdot 11^2 \cdot 65$ with $\beta = 2.25$. Since N_s is large (N_s=11) we deleted the margins of the transverse cross section of the lattice, as we did in Fig. 12. This figure should be compared with Fig. 13, which is for $\beta > \beta_c$. One can see Fig. 16 shows

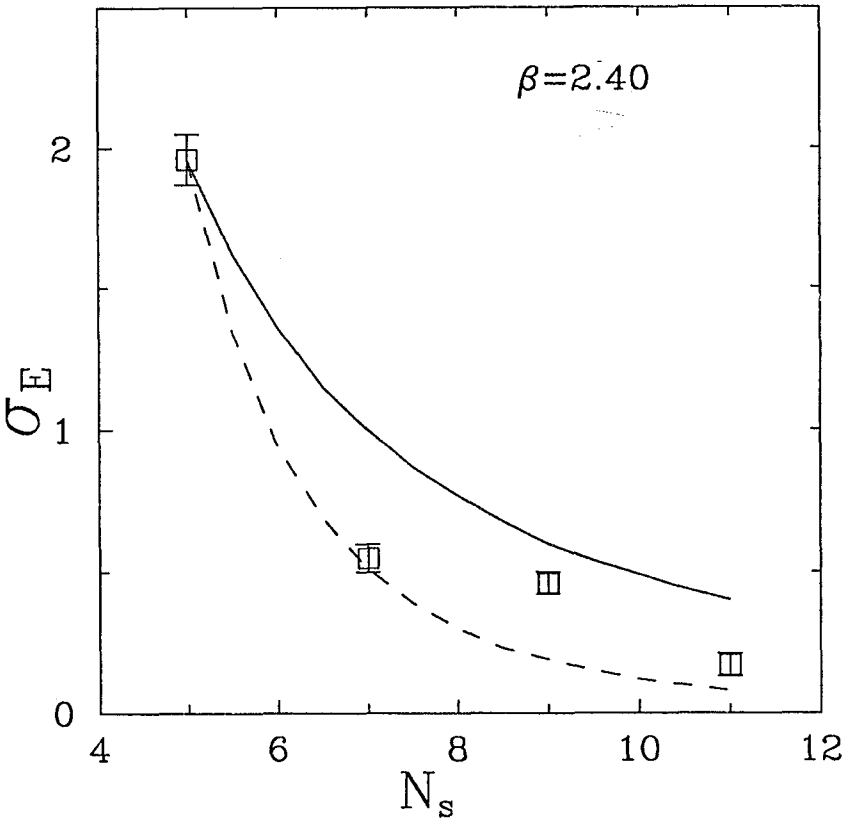

Figure 15. The plot of σ_E in the region of $\beta > \beta_c$ versus the transverse size N_s at large $q\bar{q}$ separation $r = 6a$. The solid line is the Coulomb behavior $(N_s a)^{-2}$, the dashed line is the inverse quartic behavior $(N_s a)^{-4}$, both are normalized to the data at $N_s = 5$.

significantly different behavior from Fig. 13. In Fig. 16 the peak values of ρ_A on the plane approach a finite value as r becomes large. Even at large r (i.e. $r = 6a$) this peak still exists. However, in Fig. 13 the peak of the ρ_A distribution almost disappears at $r = 6a$. So the flux distribution in Fig. 16 implies that intrinsic string formation occurs in the region of $\beta < \beta_c$. This string formation is not due to finite volume effects because these effects are small at large volumes (i.e. N_b=9, 11), as we discussed in Fig. 12 and Table 7.

We also calculated the center slice energy and action σ_E, σ_A from our flux data in the region $\beta < \beta_c$. If string formation occurs in the confined phase, for N_s large both σ_E and σ_A should approach some finite non-zero constants when $r \to \infty$. In Fig. 17 we plot the behaviors of σ_E versus. r and σ_A versus. r respectively for $\beta = 2.28$. The data were measured on lattices of various spatial sizes N_b=5, 7, 9, 11. From this figure one can see that in all cases σ_E and σ_A do not decrease with r. For each fixed N_s the values of σ_E and σ_A are almost constant as r increases. Further, for large N_s ($N_s = 9$,11), where finite volume effects are small, both σ_E and σ_A keep as finite non-zero constants as r becomes large. This behavior is totally different from that of Fig. 14, which is in the region of $\beta > \beta_c$. So Fig. 17 also implies that string formation occurs. In this figure we also notice that fluctuations of the data are large compared to the unconfined data. This is a typical behavior because confinement corresponds to disorder.

In conclusion, our flux data in the region of $\beta < \beta_c$ provide evidence for intrinsic string formation in the confined phase. This string formation is not due to finite volume effects because these effects are small as the volume becomes large (i.e. $N_s = 9, 11$).

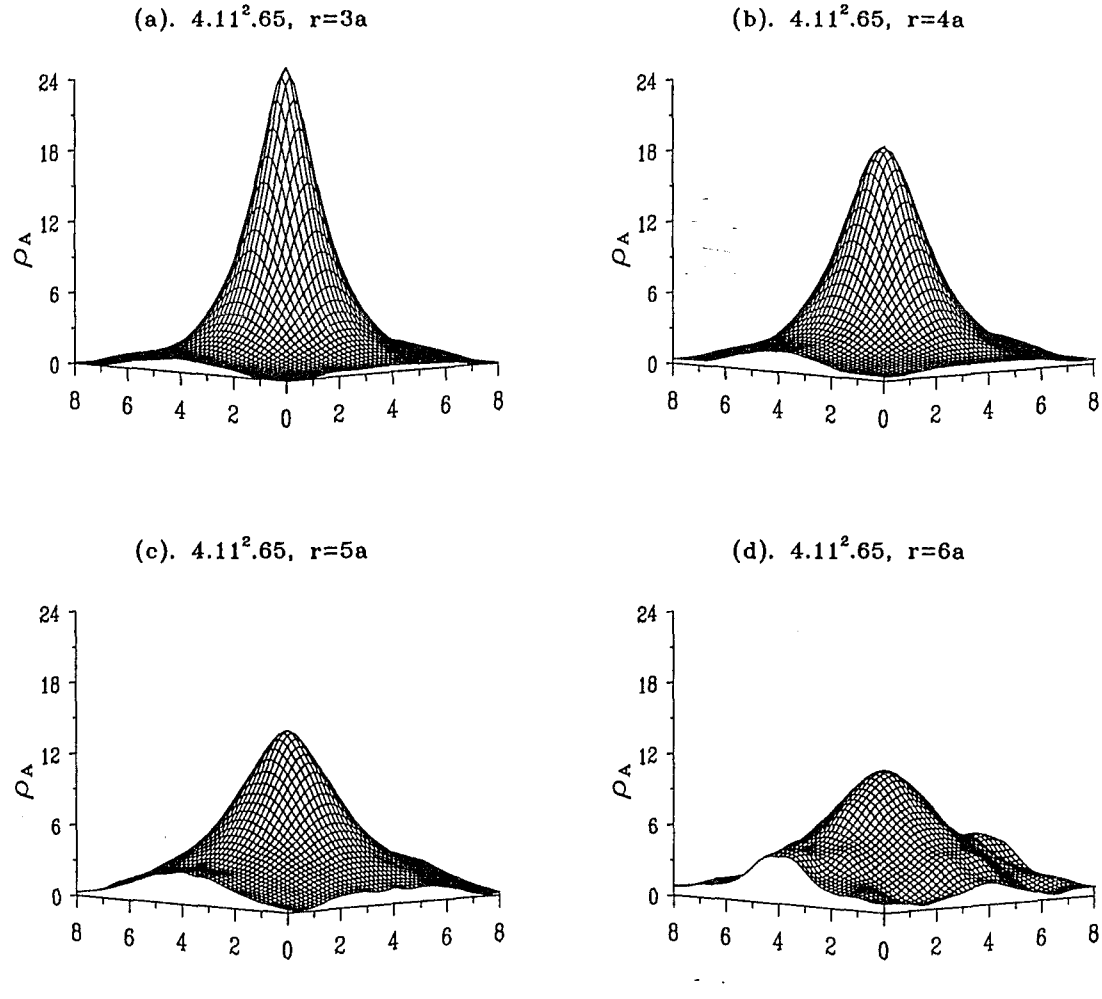

Figure 16. The action density ρ_A flux distributions in the region of $\beta < \beta_c$ for various separations (a) $r = 3a$, (b) $r = 4a$, (c) $r = 5a$ and (d) $r = 6a$. The flux data were measured on lattices $4 \cdot 11^2 \cdot 65$ with $\beta = 2.25$, and measured in the physical unit Gev/fm^3.

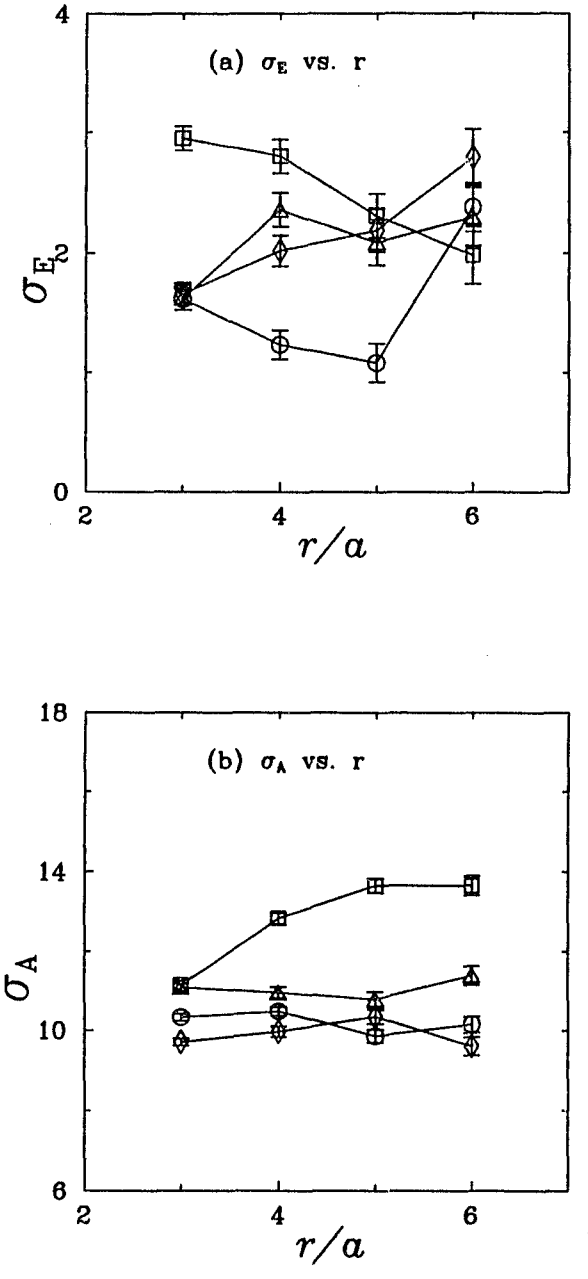

Figure 17. The center slice energy σ_E and action σ_A versus the $q\bar{q}$ separation r in the region of $\beta < \beta_c$, (a) σ_E vs. r, (b) σ_A vs. r. The data were measured on lattices $4 \cdot N_s^2 \cdot 65$ with $\beta = 2.28$ for various spatial size, $N_s = 5$ (circles), $N_s = 7$ (squares), $N_s = 9$ (triangles), $N_s = 11$ (diamonds); and are in the physical unit Gev/fm.

5.3 Implementation to Finite Volumes

As we discussed in section 5.1, we have two ways to interpret the LGT calculations. One way is to identify the shortest extent N_t of lattices to be the temporal size. This is a convenient way to study the LGT system. In previous sections we have discussed our flux data in this way. However, to compare with analytical results in finite volumes at zero temperatures, one can use another way to interpret LGT results, that is, the longest extent N_z of lattices is chosen as the time direction, so that the temperature is as low as possible. In this case Polyakov loops closed in the N_t (or N_s) direction are no longer viewed as quark sources, they are considered to be spatial operators. Quantities such as, the glueball mass and string tension, can be calculated from Polyakov loop correlations along the time direction (N_z). No matter which way we choose, quantities calculated in LGT are the same, the mathematics of the two ways are equivalent. In this section we shall look at the system in terms of this second interpretation, and reinterpret the results of previous sections.

If we choose N_z as the time direction, we are studying $SU(2)$ gauge theory in the volume $U = N_t \cdot N_s^2 \cdot a^3$ at near zero temperature $T_B = 1/N_z a$ because N_z is large. According to 't Hooft[40] the color field flux in a finite volume is quantizied. For a unit of flux along the N_t direction in the volume U the flux energy can be written as

$$E_1 = \kappa N_t a. \tag{5.7}$$

where the string tension κ can also be measured from Eq. (3.5) in LGT[19]. For convenience, instead of $z_g = m(0^+)N_s a$, as defined in Eq. (1.4) we shall use another parameter, $z_\kappa = \sqrt{\kappa}L = \sqrt{\kappa}N_s a$, to characterize the physical size of the volume, where κ corresponds to κ_t of ref.[19]. J. Koller and P. van Baal

Table 8: The correspondence of the two parameters z_g and z_κ.

small volume	intermediate volume	large volume
$z_g < 1$	$1 < z_g < 5$	$z_g > 5$
$z_\kappa < 0.24$	$0.24 < z_\kappa < 1.3$	$z_\kappa > 1.3$

used z_g in their analytical calculations[17], so that they could easily compare with the Monte Carlo results of LGT. B.A. Berg and A.H. Billoire used both z_g and z_κ parameters and other z parameters in analyses of their Monte Carlo data for convenience[19]. The parameter z_κ is equivalent to z_g. For example, from the data of ref.[19] one can see that $z_g \approx 1$ corresponds to $z_\kappa \approx 0.24$, and $z_g \approx 5$ corresponds to $z_\kappa \approx 1.3$. In Table 8 we show the correspondence of z_g and z_κ.

(1). Results in Intermediate Volumes ($0.24 < z_\kappa < 1.3$)

In this part we will show that our lattices with $\beta > \beta_c$ belong to the intermediate volume region. Since in this region our string tension data have large error bars, we just simply use the string tension data of ref.[19] to show that our lattices with $\beta > \beta_c$ satisfy $0.24 < z_\kappa < 1.3$. The data of ref.[19] are given in Table 9, which have high statistical accuracies.

From Table 9 we can see the values of string tension $\sqrt{\kappa}a$ and the parameter z_κ decrease with the increase of N_s and β. Our flux data were measured on lattices of the size $4 \cdot N_s^2 \cdot 65$ with N_s =5, 7, 9, 11 and $\beta = 2.36$ and 2.40, which are similar to the lattices in Table 9. We can estimate our string tension and values of z_κ from Table 9. For example, the estimated string tension for the lattice $4 \cdot 5^2 \cdot 65$ with $\beta = 2.36$ could be interpolated from the string

Table 9. The values of the string tension data and z_κ on lattices of size $4 \cdot N_s^2 \cdot 64$ with N_s =4, 6, 8 and $\beta = 2.36$, 2.38 and 2.41. The data are quoted from ref.[18].

$4 \cdot N_s^2 \cdot 64$				
N_s		4	6	8
$\beta = 2.36$	$\sqrt{\kappa}a$	0.2475 (18)	0.1593 (39)	0.1091 (39)
	$z_\kappa = N_s\sqrt{\kappa}a$	0.99 (1)	0.96 (2)	0.87 (3)
$\beta = 2.38$	$\sqrt{\kappa}a$	0.2424 (23)	0.1357 (44)	0.0732 (81)
	$z_\kappa = N_s\sqrt{\kappa}a$	0.97 (1)	0.81 (4)	0.59 (6)
$\beta = 2.41$	$\sqrt{\kappa}a$	0.2264 (14)	0.1314 (51)	
	$z_\kappa = N_s\sqrt{\kappa}a$	0.91 (1)	0.79 (3)	

tension measured on lattices $4 \cdot N_s^2 \cdot 64$ with N_s=4, 6 and $\beta = 2.36$. From Table 9 one can see that for N_s=5 the string tension satisfies, $0.1593 < \sqrt{\kappa}a < 0.2475$, and $0.80 < z_\kappa = \sqrt{\kappa}aN_s < 1.24$, which is in the intermediate volume region, $0.24 < z_\kappa < 1.3$, as shown in Table 8. By comparing our lattices with Table 9 in this way, we find that our lattices with $\beta = 2.36$ and 2.40 for N_s =5, 7, 9, 11 are all in the intermediate volume region, with the "*box temperature*" approaching zero, i.e. $T_B \to 0$.

As we discussed in section 5.2, for $\beta > \beta_c$ there is no intrinsic string formation. However, since finite volume effects are large when the transverse size N_s is small, this results in the observed string tension in these cases. As N_s becomes larger, finite volume effects becomes smaller, the string tension becomes smaller. This is confirmed by Table 9. Since the lattices with $\beta > \beta_c$ in our study all belong to the intermediate volume region, in these cases we find there is no intrinsic string formation, and the string tension is due to finite volume effects. In general, we expect that the results apply to the whole intermediate volume region in the zero temperature limit ($T_B \to 0$).

Table 10. Our string tension data κ and the values of the z_κ parameter on lattices of the size $4 \cdot N_s^2 \cdot 65$ with N_s =5, 7, 9, 11 and $\beta = 2.25$ and 2.28.

$4 \cdot N_s^2 \cdot 65$			
N_s	β	$\sqrt{\kappa}a$	$z_\kappa = N_s\sqrt{\kappa}a$
5	2.25	0.300 (22)	1.5 (1)
	2.28	0.251 (34)	1.3 (2)
7	2.25	0.288 (31)	2.2 (2)
	2.28	0.258 (31)	1.8 (2)
9	2.25	0.262 (84)	2.4 (8)
	2.28	0.226 (67)	2.0 (6)
11	2.25	0.307 (48)	3.4 (5)
	2.28	0.232 (64)	2.6 (7)

(2). Results in Large Volumes ($z_\kappa > 1.3$)

For $\beta < \beta_c$ we can easily extract the string tension, which is given in Table 10. In this table we also show the values of z_κ for lattices with $\beta < \beta_c$. One can see that most lattices listed in Table 10 satisfy $z_\kappa > 1.3$, with one case in the critical region, $z_\kappa \approx 1.3$ for $\beta = 2.28$ and $N_s = 5$. From Table 8 we know that lattices satisfying the condition, $z_\kappa > 1.3$, belong to the large volume region in the zero temperature limit ($T_B \to 0$). So our lattices with $\beta < \beta_c$, as listed in Table 10, are in this region.

As we discussed in section 5.2, a system with $\beta < \beta_c$ is in the confined phase in the infinite volume limit. In this case we have shown that intrinsic string formation occurs. As the transverse size N_s is made small (e.g. $N_s = 5$), we also observed some finite volume effects, as shown in Fig. 16; however, it does not change the nature of $q\bar{q}$ confinement. We have shown that the lattices with $\beta < \beta_c$ in our study all belong to the large volume region in the zero temperature limit ($T_B \to 0$). From our study we have found evidence

for intrinsic string formation in these cases, which is not due to finite volume effects. We expect that the intrinsic string formation occurs in the whole large volume region.

CHAPTER 6

MICHAEL SUM RULES AND FINITE SIZE EFFECTS

As we discusssed in last chapter, we measured the $q\bar{q}$ flux distributions at various temperatures. The flux energies are related to the potential energy $V(r)$ of the $q\bar{q}$ system by Michael sum rules[20]. To make our discussions clear, we shall briefly review the derivation of these sum rules and present our supplements and generalizations. Then we compare our flux data with the predictions from these sum rules.

6.1 Review and Generalizations of Michael Sum Rules

For a static $q\bar{q}$ system at the spatial separation r Michael sum rules states that, in the limit of zero temperatures, infinite volumes and the lattice spacing $a \to 0$, the electric and magnetic flux energies of a $q\bar{q}$ system in Minkowski space are[20],

$$E_{el}(r) = \sum_s \frac{1}{2}a^3 < \mathcal{E}^2 >= -\frac{1}{2}V(r)[\frac{\partial lna}{\partial ln\beta} - 1] - \frac{1}{2a}[\beta\frac{\partial f}{\partial \beta} - f], \tag{6.1}$$

$$E_{ma}(r) = \sum_s \frac{1}{2}a^3 < \mathcal{B}^2 >= \frac{1}{2}V(r)[\frac{\partial lna}{\partial ln\beta} + 1] + \frac{1}{2a}[\beta\frac{\partial f}{\partial \beta} + f]. \tag{6.2}$$

where the sums extends over the whole space around the $q\bar{q}$, $V(r)$ is the $q\bar{q}$ potential energy, and f/a is the self energy of the $q\bar{q}$ sources. $E_{el}(r)$ and $E_{ma}(r)$ denote the electric and magnetic parts of the flux energy, $< \mathcal{E}^2 >$ and $< \mathcal{B}^2 >$ are given by Eq. (3.13).

(1). The Action Sum Rules

To derive Eqs. (6.1) and (6.2), it is convenient to work in the transfer matrix formalism of LGT. We choose the temporal gauge[22], that is, all temporal links are trivial, $U_t(n) = e^{igaA_\mu(n)} = 1$. One remark about the temporal gauge of a finite lattice is that along a time axis one can not choose all temporal links $U_t = 1$, because of the restriction that Polyakov loop closed in the time direction is gauge invariant, which can have values other than the trivial one, $P(\vec{r}) = 1$. Therefore, on a finite lattice one can choose all temporal links to be trivial, except one link on each time axis, which can be chosen far from the operators under considerations.

Let's consider a Wilson loop W of the temporal size na and the spatial size r, as shown in Fig. 18. The time directed pathes represent the $q\bar{q}$ sources, the space directed pathes $P_r(0)$ and $P_r(n)$ create and annihilate the color field of the $q\bar{q}$ system from the vacuum. In the temporal gauge the expectation of the Wilson loop becomes,

$$< W >=< P_r(0)P_r(n) >, \tag{6.3}$$

where the expectation is evaluated in the partition function form, as defined in Eq. (2.21), i.e.,

$$< W >= \frac{\int d[U]e^{-\beta S'}W}{\int d[U]e^{-\beta S'}}, \tag{6.4}$$

with $\beta S' = S$, the action given by Eq. (3.4) for $SU(2)$, i.e. $S' = \sum(1 - \Box)$, with $\Box$ defined in Eq. (3.6), the sum is over all plaquettes on the lattice.

Using the transfer matrix approach[22, 41], as we discussed in section 2.4, and assuming a discrete spectrum for the lowest eigenstates of the

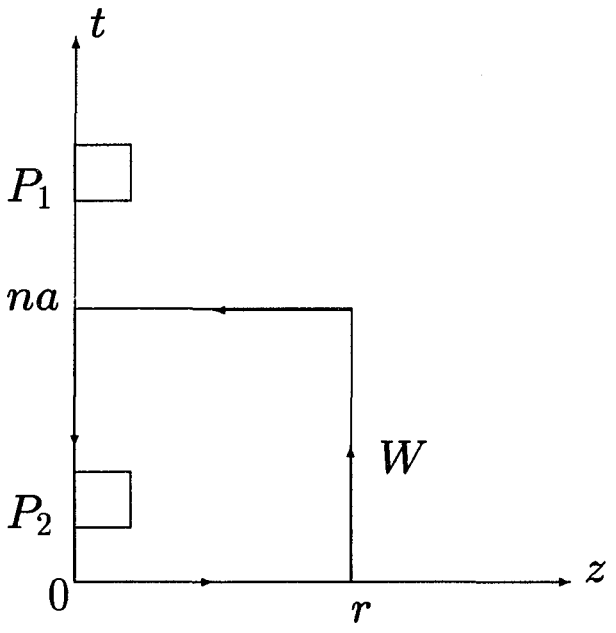

Figure 18. The Wilson loop W of the temporal size na and the spatial size r. The plaquette P_1 is outside the Wilson loop W, and the plaquette P_2 is inside the Wilson loop W.

transfer matrix, one can evaluate Eq. (6.3) as

$$\begin{aligned} < W > &= \frac{1}{Z} tr(P_r(0)\mathcal{T}_{q\bar{q}}^n P_r(n)\mathcal{T}^{N_t-n}) \\ &= \frac{1}{\sum_\alpha \lambda_\alpha^{N_t}} \sum_{\mu,\nu} < \mu|P_r|\nu, r > \lambda_\nu^n(r) < \nu, r|P_r|\mu > \lambda_\mu^{N_t-n} \\ &= \frac{1}{\sum_\alpha \lambda_\alpha^{N}} \sum_{\mu,\nu} d_{\mu\nu} d_{\nu\mu} \lambda_\nu^n(r) \lambda_\mu^{N_t-n}, \end{aligned} \tag{6.5}$$

where $\mathcal{T}_{q\bar{q}}$ is the transfer matrix projected into the $q\bar{q}$ sector of the Hilbert space, $\mathcal{T}$ is the transfer matrix without the $q\bar{q}$. $|\nu, r >$ and $|\mu >$ are the eigenstates of $\mathcal{T}_{q\bar{q}}$ and $\mathcal{T}$ respectively, and $\lambda_\nu(r)$, λ_μ are the corresponding eigenvalues, with $\lambda_\nu(r) = e^{-aE_\nu(r)}$ and $\lambda_\mu = e^{-aE_\mu}$. The coefficient $d_{\mu\nu} =< \mu|P_r|\nu, r >$. In the limit of $N_t \to \infty$, the partition function $Z = \lambda_0^{N_t}$, and in Eq. (6.5) the dominant contributions correspond to $\mu = 0$, that is,

$$< W >= \sum_\nu d_{0\nu}^2 \left(\frac{\lambda_\nu(r)}{\lambda_0}\right)^n, \qquad (\text{as } N_t \to \infty) \tag{6.6}$$

If the temporal size n of the Wilson loop W is very large ($n \to \infty$), the dominant term in Eq. (5.5) is given by $\nu = 0$,

$$< W >= d_{00}^2 \left(\frac{\lambda_0(r)}{\lambda_0}\right)^n = d_{00}^2 e^{-na(E_0(r)-E_0)}, \qquad (\text{as } N_t,\, n \to \infty) \tag{6.7}$$

where the energy of the vacuum E_0 is usually chosen to be zero, in the following we will take this choice which implies $\lambda_0 = 1$.

Now we consider the $\beta-$derivative of Eq. (6.7), that is,

$$\frac{\partial < W >}{\partial \beta} = - < WS' > + < W >< S' >= \frac{\partial}{\partial \beta}[d_{00}^2 e^{-naE_0(r)}], \tag{6.8}$$

where we have taken $E_0 = 0$, and S' is defined after Eq. (6.4).

Consider a plaquette $\Box(m)$ outside the Wilson loop W in the time direction (i.e., $0 < n < m$), e.g., the plaquette P_1 in Fig. 18, where we draw a

plaquette with a time extension. In the limit of infinite large n and infinitesimal lattice spacing, $a \to 0$, one can neglect the time extension of P_1. The contribution of P_1 to the L.H.S. of Eq. (6.8) is $< W\Box(m) > - < W >< \Box(m) >$. As $\Box(m)$ is far from W (i.e. $m-n \gg 1$), one has $< W\Box(m) > \approx < W >< \Box(m) >$, then the contribution vanishes, $< W\Box(m) > - < W >< \Box(m) > \to 0$. However, when $\Box(m)$ is close to W ($m \approx n$), one expects that this contribution does not vanish. Now let us show this explicitly,

$$
\begin{aligned}
& < W\Box(m) > - < W >< \Box(m) > \qquad (\text{for } 0 < n < m) \\
& = \frac{1}{Z} tr(P_r(0)\mathcal{T}_{q\bar{q}}^{n} P_r(n)\mathcal{T}^{m-n}\Box(m)\mathcal{T}^{N_t-m}) - < W >< \Box(m) > \\
& \xrightarrow{N_t\to\infty} \sum_{\mu,\nu} d_{0\mu}\left(\frac{\lambda_\mu(r)}{\lambda_0}\right)^n d_{\mu\nu}\left(\frac{\lambda_\nu}{\lambda_0}\right)^{m-n} < \nu|\Box(m)|0 > \\
& - \sum_{\mu} d_{0\mu}^2\left(\frac{\lambda_\mu(r)}{\lambda_0}\right)^n < 0|\Box(m)|0 >, \qquad (6.9)
\end{aligned}
$$

where in the last step we have used Eq. (6.6)

From Eq. (6.9) one can see that as $m - n \gg 1$, the dominant term of $< W\Box(m) >$ corresponds to $\nu = 0$, which would be cancelled by the product $< W >< \Box(m) >$, so one has $< W\Box(m) > - < W >< \Box(m) > \approx 0$ as $m - n \gg 1$.

However, for $m \approx n$, the term of $\nu = 0$ of the quantity, $< W\Box(m) >$, in Eq. (6.9) is cancelled by the product $< W >< \Box(m) >$. The major contribution comes from the term of $\nu = 1$. In the limit of $n \to \infty$ Eq. (6.9) becomes,

$$
\begin{aligned}
& < W\Box(m) > - < W >< \Box(m) > \qquad (\text{for } 0 < n < m) \\
& \approx \sum_{\mu} d_{0\mu}\left(\frac{\lambda_\mu(r)}{\lambda_0}\right)^n d_{\mu 1}\left(\frac{\lambda_1}{\lambda_0}\right)^{m-n} < 1|\Box(m)|0 > \\
& \xrightarrow{n\to\infty} e^{-naE_0(r)} d_{00} d_{01} {\lambda_1}^{m-n} < 1|\Box(m)|0 > . \qquad (6.10)
\end{aligned}
$$

where in the last step we have used the fact that $\lambda_0 = 1$, and the dominant term is $\mu = 0$ as $n \to \infty$. Eq. (6.10) implies that when the plaquette $\Box(m)$ is close to the Wilson loop in the time direction, it gives a contribution of the order $e^{-naE_0(r)}$, because the coefficients d_{00}, d_{01} and λ_1^{m-n} are of order of unity in this case.

Finally for the plaquette $\Box(m)$ inside the Wilson loop W in the time direction (i.e. $0 < m < n$), e.g., the plaquette P_2 in Fig. 18, its contribution to the L.H.S. of Eq. (6.8) is,

$$\begin{aligned}
&< W\Box(m) > - < W >< \Box(m) > \qquad (0 < m < n) \\
&= \frac{1}{Z} tr(P_r(0)\mathcal{T}_{q\bar{q}}^m \Box(m) \mathcal{T}_{q\bar{q}}^{n-m} P_r(n) \mathcal{T}^{N_t-n}) - < W >< \Box(m) > \\
&\overset{N_t\to\infty}{\longrightarrow} \sum_{\mu,\nu} d_{0\mu} d_{\nu 0} \left(\frac{\lambda_\mu(r)}{\lambda_0}\right)^m \left(\frac{\lambda_\nu(r)}{\lambda_0}\right)^{n-m} < \mu, r|\Box(m)|\nu, r > \\
&- < W >< \Box(m) > . \qquad (6.11)
\end{aligned}$$

In the limit of $n \to \infty$, and for cases that both m and $n - m$ are large, the dominant term of Eq. (6.11) is given by $\mu = \nu = 0$, that is,

$$\begin{aligned}
&< W\Box(m) > - < W >< \Box(m) > \qquad (0 < m < n) \\
&\approx d_{00}^2 \left(\frac{\lambda_0(r)}{\lambda_0}\right)^n [< 0, r|\Box(m)|0, r > - < 0|\Box(m)|0 >] \\
&= d_{00}^2 \left(\frac{\lambda_0(r)}{\lambda_0}\right)^n (\Box(m))_{r-0}, \qquad (6.12)
\end{aligned}$$

where we denote $(\Box(m))_{r-0} = [< 0, r|\Box(m)|0, r > - < 0|\Box(m)|0 >]$, and Eq. (6.7) is used.

From the above discussion we can conclude that for plaquettes outside the Wilson loop W in the time direction, their contributions to the L.H.S. of Eq. (6.8) can be neglected as they are far enough from W. For the Wilson loop of large temporal size, i.e., $n \to \infty$, the major contribution to the L.H.S. of

Eq. (6.8) comes from plaquettes inside W. The contribution of one plaquette inside W is given by Eq. (6.12). Summing over contributions from all such plaquettes gives the dominant term of the L.H.S. in Eq. (6.8), that is,

$$\begin{aligned} \frac{\partial < W >}{\partial \beta} &= - < WS' > + < W >< S' > \\ &= nd_{00}^2 \Big(\frac{\lambda_0(r)}{\lambda_0} \Big)^n (\sum_s \Box(m))_{r-0}, \end{aligned} \tag{6.13}$$

where the sum $\sum_s$ is over all plaquettes in the spatial volume at one fixed time value. The factor of n comes from summing equal contributions from plaquettes on each time slice. The dominant term on the R.H.S. of Eq. (6.8) is, as $n \to \infty$,

$$\frac{\partial}{\partial \beta}[d_{00}^2 e^{-naE_0(r)}] = -nd_{00}^2 e^{-naE_0(r)} \frac{\partial [aE_0(r)]}{\partial \beta}. \tag{6.14}$$

Collecting Eqs. (6.8) and (6.13), (6.14) yields,

$$-\frac{\partial aE_0(r)}{\partial \beta} = < r,0| \sum \Box |r,0> - < 0| \sum \Box |0> \equiv (\sum \Box)_{r-0}, \tag{6.15}$$

where the R.H.S. can be measured by calculating the quantity $< W\Box > / < W >$ in LGT. In the continuum limit, $a \to 0$, the R.H.S. of Eq. (6.15) becomes,

$$(\sum \Box)_{r-0} = \frac{1}{\beta} \sum_s \frac{1}{2} a^4 [< \mathcal{E}^2 >_{r-0} - < \mathcal{B}^2 >_{r-0}] = \frac{a}{\beta} A, \tag{6.16}$$

where $\vec{\mathcal{E}}$ and $\vec{\mathcal{B}}$ are the color electric and magnetic fields in Minkowski space, A is the integration of the action density over the spatial volume.

On the L.H.S. of Eq. (6.15) if we write the $q\bar{q}$ color field energy $E_0(r)$ in the form [20],

$$E_0(r) = V(r) + f(\beta)/a, \tag{6.17}$$

where $V(r)$ is the $q\bar{q}$ potential energy, f/a is the self-energy. Then we obtain the following relation from Eq. (6.15) in the continuum limit,

$$A = -\frac{\beta}{a}\frac{\partial a E_0(r)}{\partial \beta} = -\frac{\beta}{a}\frac{\partial a V(r)}{\partial \beta} - \frac{\beta}{a}\frac{\partial f}{\partial \beta}. \tag{6.18}$$

This is just the Michael's action sum rule, which can be obtained by subtracting Eq. (6.2) from Eq. (6.1) because of $A = E_{\rm el} - E_{\rm ma}$, if we assume that $V(r)$ scales and hence is independent of β.

(2). Energy Sum Rules and Their Generalizations

To derive the energy sum rules in Eqs. (6.1) and (6.2) we need to study the color electric and color magnetic fields separately. Let us consider an asymmetric lattice with the time-spacing a_t and the spatial-spacing a_s $(= a)$, and the asymmetry is $\xi = a_s/a_t$ [20]. The action for $SU(N)$ LGT becomes,

$$S_A = -\beta_t \sum \Box_t - \beta_s \sum \Box_s + const\cdot, \tag{6.19}$$

where $\Box_t$ is a plaquette with a time extent and $\Box_s$ is a space-like plaquette. In the continuum limit (a_s, $a_t \to 0$) the action must become the classical action in Eq. (2.4), that is,

$$S_A \longrightarrow \frac{1}{4}\int d^4x (F^c_{\mu\nu})^2. \tag{6.20}$$

In this limit the time-like plaquette becomes

$$\begin{aligned} \beta_t \Box_t &= \beta_t \Box_{j4} = \beta_t \frac{1}{N} tr(e^{i a_t a_s g_t F_{j4}}) \\ &\approx \beta_t (1 - \frac{1}{4N} a_t^2 a_s^2 g_t^2 (F^c_{j4})^2), \end{aligned} \tag{6.21}$$

where N is for $SU(N)$. $j = 1, 2, 3$ and c is the colour index. To get the correct continuum action of Eq. (6.20) we should require that in Eq. (6.21),

$$\frac{\beta_t}{2N} a_t^2 a_s^2 g_t^2 = a_s^3 a_t,$$

then we obtain the relation between β_t and g_t.

$$\beta_t = \frac{2N}{g_t^2}\frac{a_s}{a_t} = \frac{2N}{g_t^2}\xi. \tag{6.22}$$

Similarly one can obtain the relation between β_s and g_s,

$$\beta_s = \frac{2N}{g_s^2}\frac{a_t}{a_s} = \frac{2N}{g_s^2}\xi^{-1}. \tag{6.23}$$

In the weak coupling limit, β_s, β_t can be expanded in terms of the coupling β of the corresponding symmetric lattice [20, 42],

$$\beta_s\xi = \beta(a) + 2Nc_s(\xi) + O(\beta^{-1}), \tag{6.24}$$

$$\beta_t\xi^{-1} = \beta(a) + 2Nc_t(\xi) + O(\beta^{-1}); \tag{6.25}$$

where the coefficients $c_s(\xi)$ and $c_t(\xi)$ satisfy the conditions [20, 43],

$$\begin{aligned} c_s(\xi)|_{\xi=1} &= c_t(\xi)|_{\xi=1} = 0, \\ \frac{\partial}{\partial\xi}[c_s(\xi) + c_t(\xi)]_{\xi=1} &= (c_s' + c_t')_{\xi=1} = b_0 = 11N/48\pi^2, \end{aligned} \tag{6.26}$$

and c_s' (c_t') denotes the ξ-derivative of c_s (c_t).

With these definitions we can now study the electric and magnetic fields of the $q\bar{q}$ sources. If we consider a Wilson loop W of the size na_t in the time direction and r in the space direction on the asymmetric lattice, we can obtain a similar result as Eq. (6.7),

$$< W >= d_{00}^2 e^{-na_t E_0(r)}, \qquad (\text{as } N_t,\, n \to \infty\ ) \tag{6.27}$$

where $E_0(r)$ is the ground-state energy of the $q\bar{q}$ pair, and $< W >$ is defined by the partition function formalism in Eq. (6.4), with the action $\beta S'$ replaced by S_A in Eq. (6.19).

By taking the derivatives of Eq. (6.27) with respect to β_s and β_t respectively one can get the following relations similar to Eq. (6.15),

$$-\frac{\partial a_t E_0(r)}{\partial \beta_t} = (\sum_s \Box_t)_{r-0}, \tag{6.28}$$

$$-\frac{\partial a_t E_0(r)}{\partial \beta_s} = (\sum_s \Box_s)_{r-0}. \tag{6.29}$$

where the sum $\sum_s$ is over the whole spacial volume as before. The R.H.S. of Eqs. (6.28) and (6.29) become the total color electric and color magnetic energies of the $q\bar{q}$ pair respectively in the continuum limit ($a_s, a_t \to 0$). On the symmetric lattice ($\xi = 1$) one has,

$$\lim_{a\to 0}(\sum \Box_t)_{r-0} = \frac{1}{\beta}\sum_s \frac{1}{2}a^4 < \mathcal{E}^2 >_{r-0}, \tag{6.30}$$

$$\lim_{a\to 0}(\sum \Box_s)_{r-0} = -\frac{1}{\beta}\sum_s \frac{1}{2}a^4 < \mathcal{B}^2 >_{r-0}; \tag{6.31}$$

where $\vec{\mathcal{E}}$ and $\vec{\mathcal{B}}$ are the electric and magnetic fields in Minkowski space.

To evaluate the L.H.S. of Eqs. (6.28) and (6.29) we need to resort following relations which relate the quantities on the asymmetric lattice with the quantities of the equivalent symmetric lattice,

$$\left(\frac{\partial F(\beta_s,\beta_t)}{\partial \beta_t}\right)_{\xi=1} = \frac{1}{2}\left(\frac{\partial F}{\partial \beta} + \frac{1}{\beta}\frac{\partial F}{\partial \xi}\right)_{\xi=1}, \tag{6.32}$$

$$\left(\frac{\partial F(\beta_s,\beta_t)}{\partial \beta_s}\right)_{\xi=1} = \frac{1}{2}\left(\frac{\partial F}{\partial \beta} - \frac{1}{\beta}\frac{\partial F}{\partial \xi}\right)_{\xi=1}; \tag{6.33}$$

where $F(\beta_s, \beta_t)$ is a function of β_s, β_t. From Eqs. (6.24) and (6.25) one can see that β_s, β_t and β, ξ are two equivalent sets of variables, that is, $F(\beta_s, \beta_t) = F(\beta_s(\beta,\xi), \beta_t(\beta,\xi))$. The proof of the above relations will be given in Appendix B.

Since we can write the energy $E_0(r)$ of Eqs. (6.32) and (6.33) in the form, $E_0(r) = V(r) + f(\beta)/a$, from Eq. (6.17), then the L.H.S. of Eq. (6.28)

becomes,

$$\Big(\frac{\partial a_t E_0(r)}{\partial \beta_t}\Big)_{\xi=1} = \Big(\frac{\partial a_t V(r)}{\partial \beta_t}\Big)_{\xi=1} + \Big(\frac{\partial (f/\xi)}{\partial \beta_t}\Big)_{\xi=1}. \tag{6.34}$$

Applying Eq. (6.32) to the above equation, and using the fact that the potential $V(r)$ is independent of β in the limit of infinite lattice sizes and infinitesimal lattice spacing ($a \to 0$), one can obtain,

$$\begin{aligned}\Big(\frac{\partial a_t V(r)}{\partial \beta_t}\Big)_{\xi=1} &= \frac{1}{2}\Big(\frac{\partial a_t V(r)}{\partial \beta} + \frac{1}{\beta}\frac{\partial a_t V(r)}{\partial \xi}\Big)_{\xi=1} \\ &= \frac{1}{2}V(r)\Big(\frac{\partial a}{\partial \beta} - \frac{a}{\beta}\Big),\end{aligned} \tag{6.35}$$

where we have used $(\frac{\partial a_t}{\partial \beta})_{\xi=1} = \frac{\partial a}{\partial \beta}$ and $(\frac{\partial a_t}{\partial \xi})_{\xi=1} = -a$. Also the second term on the L.H.S of Eq. (6.34), $(\frac{\partial (f/\xi)}{\partial \beta_t})_{\xi=1}$ in Eq. (6.34), can be evaluated as,

$$\Big(\frac{\partial (f/\xi)}{\partial \beta_t}\Big)_{\xi=1} = \frac{1}{2}\Big(\frac{\partial f(\beta)}{\partial \beta} - \frac{f(\beta)}{\beta}\Big). \tag{6.36}$$

where the self-energy $f(\beta)/a$ depends on β and a. Substituting Eqs. (6.35) and (6.36) into Eq. (6.34) yields

$$\Big(\frac{\partial a_t E_0(r)}{\partial \beta_t}\Big)_{\xi=1} = \frac{1}{2}V(r)\Big(\frac{\partial a}{\partial \beta} - \frac{a}{\beta}\Big) + \frac{1}{2}\Big(\frac{\partial f(\beta)}{\partial \beta} - \frac{f(\beta)}{\beta}\Big). \tag{6.37}$$

Similarly, one can also evaluate the L.H.S. of Eq. (6.29) by applying Eq. (6.33), the result is,

$$\Big(\frac{\partial a_t E_0(r)}{\partial \beta_s}\Big)_{\xi=1} = \frac{1}{2}V(r)\Big(\frac{\partial a}{\partial \beta} + \frac{a}{\beta}\Big) + \frac{1}{2}\Big(\frac{\partial f(\beta)}{\partial \beta} + \frac{f(\beta)}{\beta}\Big). \tag{6.38}$$

From Eqs. (6.28), (6.29), (6.30), (6.31) and (6.37), (6.38) one can get the sum rules in Eqs. (6.1) and (6.2).

Now we proceed to consider the generalization of these sum rules to the finite temperature case. In the limit of finite temperature (T) and infinite

volume the potential $V(r)$ would be a function of r and T (or β) because of $T = 1/N_t a(\beta)$. For example, in the confined phase $V(r) \sim \kappa r$, with the string tension $\kappa = \kappa(\beta)$ for fixed lattice size N_t, as discussed in section 4.2. In this case one can write, $V(r) = V(r, \beta)$. Then Eq. (6.35) should be rewritten as,

$$\Big(\frac{\partial a_t V(r)}{\partial \beta_t}\Big)_{\xi=1} = \frac{1}{2}\Big(\frac{\partial a V(r,\beta)}{\partial \beta} - \frac{a}{\beta} V(r,\beta)\Big). \tag{6.39}$$

Similarly one has,

$$\Big(\frac{\partial a_t V(r)}{\partial \beta_s}\Big)_{\xi=1} = \frac{1}{2}\Big(\frac{\partial a V(r,\beta)}{\partial \beta} + \frac{a}{\beta} V(r,\beta)\Big). \tag{6.40}$$

The self-energy part $f(\beta)/a$ does not change in this case. Therefore, at finite temperature Michael sum rules in Eqs. (6.1) and (6.2) should be modified as following [44],

$$E_{el}(r) = -\frac{1}{2}\Big(\frac{\beta}{a}\frac{\partial[aV(r)]}{\partial\beta} - V(r)\Big) - \frac{1}{2a}\Big(\beta\frac{\partial f}{\partial\beta} - f\Big), \tag{6.41}$$

$$E_{ma}(r) = \frac{1}{2}\Big(\frac{\beta}{a}\frac{\partial[aV(r)]}{\partial\beta} + V(r)\Big) + \frac{1}{2a}\Big(\beta\frac{\partial f}{\partial\beta} + f\Big). \tag{6.42}$$

These modified sum rules can be obtained from Eqs. (6.1) and (6.2) by the replacement,

$$V(r)\frac{\partial a}{\partial\beta} \to \frac{\partial[aV(r)]}{\partial\beta}. \tag{6.43}$$

We expect that the modified sum rules would account for the finite temperature effects on the $q\bar{q}$ system. Although Eqs. (6.41) and (6.42) are derived by considering the Wilson loop representation of the $q\bar{q}$ pair, we expect that they can be applied in describing the flux distributions $f'_{\mu\nu}$ in Eq. (3.9), which involves the Polyakov loops, because both the Wilson loop, W, and Polyakov loops, $P(0)P^\dagger(r)$, represent a $q\bar{q}$ pair. In the following we shall use our $SU(2)$ flux data in the confined phase to check the modified Michael sum rules in Eqs. (6.41) and (6.42).

6.2 Analysis of Flux Data

In this part we shall compare our flux data with the predictions of the modified Michael sum rules in Eqs. (6.41) and (6.42).

As we mentioned in section 3.2, we used the multihit technique[32] in the flux measurements. The flux data is only good as the test charge (plaquette) is away from the $q\bar{q}$ sources (Polyakov loops). Thus we only consider the flux data on the middle transverse slice between the $q\bar{q}$ pair at large separations (i.e. $r \geq 3a$).

In the confined phase the string formation is expected to occur. As the separation r of a $q\bar{q}$ pair is large enough, the flux energy stored in the flux tube of unit length between the $q\bar{q}$ should equal to the string tension κ. In this case one can obtain the color electric and magnetic energy of the flux tube per unit length from Eqs. (6.41) and (6.42),

$$\sigma_{el} = \frac{dE_{el}(r)}{dr} = -\frac{1}{2}\left(\frac{\beta}{a}\frac{\partial[a\kappa]}{\partial\beta} - \kappa\right), \tag{6.44}$$

$$\sigma_{ma} = \frac{dE_{ma}(r)}{dr} = \frac{1}{2}\left(\frac{\beta}{a}\frac{\partial[a\kappa]}{\partial\beta} + \kappa\right). \tag{6.45}$$

The corresponding flux action is

$$\sigma_A = \sigma_{el} - \sigma_{ma} = -\frac{\beta}{a}\frac{\partial[a\kappa]}{\partial\beta}, \tag{6.46}$$

which is the integration of the action density on the transverse plane. And the corresponding flux energy is

$$\sigma_E = \sigma_{el} + \sigma_{ma} = \frac{dV(r)}{dr} = \kappa(\beta). \tag{6.47}$$

which agrees with our expectation for string formation.

Eq. (6.46) can also be obtained from the action sum rule of Eq. (6.18). The R.H.S. of Eq. (6.46) is, $\frac{\beta}{a}\frac{\partial(a\kappa)}{\partial\beta} = \kappa\frac{\partial ln a}{\partial ln\beta} + \beta\frac{\partial\kappa}{\partial\beta}$. The first term can be

estimated from the scaling relation of Eqs. (2.33) and (2.34), e.g. $\frac{\partial ln a}{\partial ln \beta} \sim -8$ for $\beta \sim 2.4$, which is consistent with the flux measurement results of ref.[28]. The second term $\beta \frac{\partial \kappa}{\partial \beta}$ can also be estimated from the fitting function in Eq. (4.15), and it is negative because κ decreases with β, as shown in Eq. (4.12). So Eq. (6.46) implies that $\sigma_A \gg \sigma_E = \kappa$ for cases we consider. Also Eqs. (6.44) and (6.45) show that the electric part of the flux energy σ_{el} is positive, but the magnetic part σ_{ma} negative, their magnitudes are of the same order with σ_{el} slightly larger. These predictions can be summarized as below,

$$\begin{aligned} \sigma_{el} &> 0 \quad \text{and} \quad \sigma_{ma} < 0, \\ \sigma_E &= \sigma_{el} + \sigma_{ma} = \kappa > 0, \\ \sigma_A &\gg \sigma_E; \end{aligned} \tag{6.48}$$

where these flux energies (action) are defined in the confined phase.

From our flux data we can calculate the values of σ_{el}, σ_{ma}, σ_E and σ_A, which are the energies (action) stored in the center slice between the $q\bar{q}$ pair. One typical result is shown in Table 11. One can see that the measured data agree with Eq. (6.48) qualitatively. However, when we compare σ_E data with the measured string tension, i.e. $\kappa = 0.499 \pm 0.102\ Gev/fm$ for $\beta = 2.25$ on the lattice $4 \cdot 11^2 \cdot 65$, as shown in Table 6, we find that the σ_E data are not good enough to make conclusions. This may be due to the fact that σ_E is obtained from the strong cancellation between two terms (i.e. σ_{el} and σ_{ma})[20], so it is difficult to measure σ_E accurately.

In the following we proceed to study the prediction of the action sum rule in Eq. (6.46). As we mentioned above, the R.H.S. of Eq. (6.46) contains two terms, the first term, $\kappa \frac{\partial ln a}{\partial ln \beta}$ was predicted by the original Michael sum

Table 11. The center slice flux energies and action of a $q\bar{q}$ pair at various separations r/a in the confined phase, which were calculated from the flux data on the lattice $4 \cdot 11^2 \cdot 65$ with $\beta = 2.25$ ($\beta_c \approx 2.30$). The data are in the physical unit Gev/fm.

$4 \cdot 11^2 \cdot 65$, $\beta = 2.25$			
r/a	3	4	5
σ_{el}	4.54 (8)	5.06 (16)	5.41 (24)
σ_{ma}	-3.26 (9)	-3.65 (14)	-3.96 (27)
σ_E	1.28 (12)	1.41 (22)	1.44 (36)
σ_A	7.80 (12)	8.70 (22)	9.37 (36)

rules in Eqs. (6.1) and (6.2), the second one, $\beta\frac{\partial\kappa}{\partial\beta}$, is a new term, which is only predicted by the modified sum rules of Eqs. (6.41) and (6.42). We expect that the second term describes finite temperature effects.

From the scaling relation $a(\beta)$ of Eq. (2.33) one can estimate the quantity,

$$-\frac{\partial lna}{\partial ln\beta} = -\frac{51}{121} + \frac{3\pi^2}{11}\beta + \frac{d_2 + 2d_3\beta}{\Lambda_L^{-1}(\beta)}\beta \tag{6.49}$$

with $\Lambda_L^{-1}(\beta)$ given by Eq. (2.34). And by using the fitting function $\kappa(\beta)$ in Eq. (4.15) one can calculate the derivative,

$$\frac{\partial\kappa}{\partial\beta} = -\frac{\kappa_0}{\beta_c}\delta(1 - \frac{\beta}{\beta_c})^{\delta-1}, \tag{6.50}$$

with the constants κ_0 and δ given by Eqs. (4.13) and (4.16).

By similar considerations that lead to Eq. (6.46), one can also obtain the prediction from the original Michael sum rules in Eqs. (6.1) (6.2). The result is

$$(\sigma_A)_0 = -\kappa\frac{\partial lna}{\partial ln\beta}, \tag{6.51}$$

which is just the first term of R.H.S. in Eq. (6.46).

Table 12. The comparison of the predictions of generalized Michael sum rules and the data of center slice action σ_A.

$N_t = 4$						
β	$\kappa(\beta)$	$-\kappa\frac{\partial lna}{\partial ln\beta}$	$-\beta\frac{\partial\kappa}{\partial\beta}$	$-\kappa\frac{\partial lna}{\partial ln\beta}-\beta\frac{\partial\kappa}{\partial\beta}$	$(\sigma_A)_{4\cdot9^2\cdot65}$	$(\sigma_A)_{4\cdot11^2\cdot65}$
2.25	0.42	3.03 (37)	4 (1)	7 (2)	12.18 (23)	8.70 (22)
2.28	0.34	2.50 (39)	9 (3)	12 (3)	10.95 (14)	9.97 (13)
2.29	0.29	2.12 (40)	17 (7)	19 (7)	10.44 (12)	9.39 (10)
$N_t = 6$						
β	$\kappa(\beta)$	$-\kappa\frac{\partial lna}{\partial ln\beta}$	$-\beta\frac{\partial\kappa}{\partial\beta}$	$-\kappa\frac{\partial lna}{\partial ln\beta}-\beta\frac{\partial\kappa}{\partial\beta}$	$(\sigma_A)_{6\cdot7^2\cdot65}$	$(\sigma_A)_{6\cdot11^2\cdot37}$
2.30	0.64	4.8 (5)	1.7 (6)	7 (1)	9.07 (89)	8.86 (1.08)
2.36	0.58	4.6 (6)	3 (1)	8 (2)	8.26 (36)	11.55 (52)
2.40	0.50	4.0 (7)	8 (4)	12 (4)	8.82 (28)	9.73 (35)
2.42	0.33	3 (1)	–	–	13.29 (25)	9.37 (25)

In Table 12 we list the predictions of Eq. (6.46) obtained by substituting Eqs. (6.49) and (6.50), and the measured σ_A data in the confined phase. The data were measured on lattices $4\cdot9^2\cdot65$, $4\cdot11^2\cdot65$, $6\cdot7^2\cdot65$ and $6\cdot11^2\cdot37$. The quantities $\kappa(\beta)$, $\beta\frac{\partial\kappa}{\partial\beta}$, $\kappa\frac{\partial lna}{\partial ln\beta}$ and σ_A have the physical unit Gev/fm. The values of string tension $\kappa(\beta)$ were estimated from Eq. (4.15). In the transition region (i.e. $\beta \sim 2.3$ for $N_t = 4$) no stable prediction can be obtained. Since in the confined phase the value of σ_A should not change with the $q\bar{q}$ separation r in the limit of $r \to \infty$, we then choose the σ_A data at a moderate value of r as the asymptotic value of σ_A ($r \to \infty$), because error bars are large at very large r. In Table 12 most σ_A data were calculated from the flux measurements of $q\bar{q}$ pair at $r = 4a$, in few cases we choose the data at $r = 3a$ or $5a$, depending on the quality of data.

In Fig. 19 we plot the predictions of Eqs. (6.46) and (6.51) respectively, and compare them with the σ_A data for the case of $N_t = 4$. From this figure we can see that our measured data are consistent with the prediction of

Eq. (6.46), but have large difference from the predictions of Eq. (6.51). Especially, in the transition region ($\beta \approx \beta_c$) Eq. (6.51) predicts that σ_A approaches zero as $\beta \to \beta_c$. However, our σ_A data have large values in this region, which agree with the predictions of Eq. (6.46). As the temperature decreases ($T \to 0$ or $\beta \to 0$), both predictions coincide, However, it is difficult to obtain data with clear signal in the small β region (i.e., $\beta < 2.25$).

We also notice that in Fig. 19 our σ_A data in the confined region ($\beta < \beta_c$) have some discrepancies with the prediction of Eq. (6.46) This may be due to finite size effects and finite lattice spacing effects of lattices, and to the large fluctuations in the confined phase, because confinement corresponds to disorder.

To compare the behaviors of σ_A in both phases, in Fig. 19 we also plot the σ_A data in the unconfined region (i.e., $\beta > \beta_c$). These data were measured at large $q\bar{q}$ separations, i.e., $r = 6a$, which still have clear signals, as shown in Table 13. Since in the unconfined phase there is no string formation, one expects that σ_A vanishes at large r. From this figure one can see that near the transition point (i.e. $\beta \sim 2.30$), our σ_A data in the unconfined region decrease rapidly with β, and becomes very small beyond the transition region. This agrees with the expectation. The fact that our σ_A data in the unconfined region do not vanish may be due to the following factors, in the transition region finite-size effects are large, beyond this region the contribution from the self-energy of the $q\bar{q}$ pair still exists, because the $q\bar{q}$ separation, $r = 6a$, is not large enough to approach the asymptotic region.

In conclusion our flux data are consistent with the prediction of the generalized sum rules, which shows explicitly that the $q\bar{q}$ flux distribution has

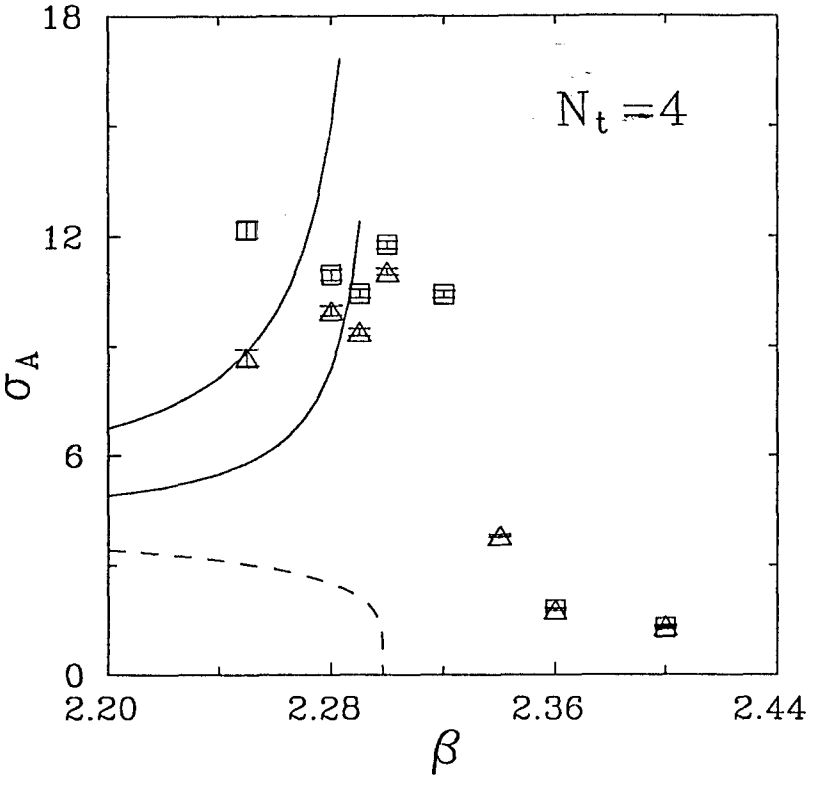

Figure 19. The plot of the predictions of σ_A vs. β of Eq.(6.46) (solid lines), and Eq.(6.51) (dashed lines). The two solid lines represent the upper and lower limits of the predictions of Eq.(6.46). The data of σ_A were measured from lattices $4 \cdot 9^2 \cdot 65$ (squares) and $4 \cdot 11^2 \cdot 65$ (triangles), which have the physical unit Gev/fm.

Table 13. The σ_A data in the unconfined phase ($\beta < \beta_c$), which were measured on lattices, $4 \cdot 9^2 \cdot 65$ and $4 \cdot 11^2 \cdot 65$. The data are in the physical unit Gev/fm.

$N_t = 4$

β	2.30	2.32	2.34	2.36	2.40
$(\sigma_A)_{4\cdot 9^2\cdot 65}$	11.77 (11)	10.40 (9)		1.78 (4)	1.28 (4)
$(\sigma_A)_{4\cdot 11^2\cdot 65}$	11.03		3.81 (4)	1.77 (3)	1.32 (4)

different behaviours in the two phases. In the confined phase the asymptotic value of the center slice action, σ_A ($r \to \infty$) has large values, however, across the transition region σ_A ($r \to \infty$) becomes very small in the unconfined phase. This agrees with our expectation that string formation occurs in the confined phase, but disappears in the unconfined phase.

SUMMARY

In this dissertation research we investigated pure $SU(2)$ gauge theory systematically using LGT method. This theory posseses the essential features of QCD which is a $SU(3)$ gauge theory, but it is much simpler for studies. It is known that QCD has different properties at different temperatures and different volumes. In this work we studied $SU(2)$ gauge theory in two limits by measuring the flux distributions of a $q\bar{q}$ pair. One is the large volume and finite temperature limit, another is the zero temperature and finite volume limit.

In the limit of infinite volume and finite temperatures we studied some general properties of the finite temperature deconfining phase transition. We find clear evidence that the string formation occurs in the confined phase, but not occur in the unconfined phase. The behavior of string tension κ with temperature is also studied, our data agree very well with the fitting function,

$$\kappa(T) = \kappa_0(1 - \frac{T}{T_c})^{\alpha} \quad (\text{for } T < T_c).$$

By choosing the time direction of lattices appropriately we can access the limit of zero temperature and finite volumes. In this limit we find that the string tension in intermediate volumes is due to finite size effects, there is no intrinsic string formation. However, in the large volume region our results support the expectation that the intrinsic string formation occurs. This elucidates the question raised by the global LGT calculations.

To check Michael sum rules with the flux data at finite temperatures, a complete derivation of the sum rules are presented, and a generalization of the sum rules is suggested to account for the finite temperature effects. We find that our flux data are consistent with the prediction of the generalized sum rules.

Our study clarified many properties of QCD, and provide strong numerical evidence for the quark confinement and the string formation. This supports the belief that QCD is the correct theory describing strong interactions, and it can explain quark confinement. This numerical study paves the way for further studies of QCD and final analytical proof of quark confinement in QCD.

Our results also confirmed that quarks are unconfined in the deconfining phase at high temperatures due to the disappearance of string formation. It is believed that quarks and gluons form the quark-gluon plasma at high temperatures, which is a new form of matter. Experiments involving high energy collisions of heavy nuclei were performed at $CERN$[50], which have shown some possible signals for the quark-gluon plasma. To get an unambiguous evidence, more detailed experimental information and higher energies are required.

So far we only studied the pure $SU(2)$ gauge theory model. To reach the real physics, we need to consider $SU(3)$ gauge theory with dynamical quarks. In the future we plan to investigate QCD in the following aspects, full QCD with dynamical quarks, the mechanism of quark confinement and properties of deconfining phase at high temperatures. We expect that by these studies strong interactions between quarks can be understood thoroughly.

REFERENCES

[1] L.H. Ryder, Elementary Particles and Symmetries, Gordon and Breach Science Publishers, (1986);
F. Halzen and A.D. Martin, Quarks and Leptons, John Wiley & Sons, (1984).

[2] D. Gross and F. Wilczek, Phys. Rev. Lett. 30 (1973), 1343;
H.D. Politzer, Phys. Rev. Lett. 30 (1973), 1346.

[3] A.M.Polyakov, Phys. Lett. B72(1978), 477.

[4] L.Susskind, Phys. Rev. D20(1979), 2610.

[5] M. Gell-Mann and Y. Ne'emann, The Eightfold Way, Benjamin, (1964).

[6] G. Zweig, CERN Report 8419/Th 412, (1964).

[7] E.D. Bloom, et al., Phys. Rev. Lett. 23 (1969), 930;
M. Breidenbach, et al., Phys. Rev. Lett. 23 (1969), 935.

[8] L.W. Jones, Rev. Mod. Phys. 49 (1977), 717.

[9] K.G. Wilson, Phys. Rev. D14 (1974), 2455.

[10] H.J.Rothe, Lattice Gauge Theories-An Introduction, World Scientific Publishing Co, (1992); and references therein.

[11] J. Wosiek, Nucl. Phys. B(Proc. Suppl.) 4 (1988), 52.

[12] J. Kuti, et al, Phys. Lett. B98 (1981), 199.

[13] G. Curci and R. Tripiccione, Phys. Lett. B151 (1985), 145.
B.A. Berg, et al, Phys. Lett. B209 (1988), 319.
B.A. Berg, et al, Phys. Rev. Lett. 62 (1989), 2433.

[14] M. Luscher, Nucl. Phys. B219 (1983), 233.

[15] M. Luscher and G. Munster, Nucl. Phys. B232 (1984), 445.

[16] P. Weisz and V. Ziemann, Nucl. Phys. B284 (1987), 157.

[17] P. van Baal and J. Koller, Ann. Phys.(NY) 174 (1987), 299.

[18] J. Koller and P. van Baal, Nucl. Phys. B302 (1988), 1.

[19] B.A. Berg and A.H. Billoire, Phys. Rev. D40(1989), 550.

[20] C. Michael, Nucl. Phys. B280 (1987),13.

[21] M. Creutz, Quarks, Gluons and Lattices, Cambridge University Press, 1983.

[22] J. Kogut, Rev. Mod. Phys. Vol.55 (1983), 775; Rev. Mod. Phys. V51 (1979), 659.

[23] L.D. Mclerran and B. Svetitsky, Phys. Rev. D24 (1981), 450. Phys. Lett. B98 (1981), 195.

[24] R. Sommer, Nucl. Phys. B306 (1988), 181.

[25] S. Perantonis, A. Huntley and C. Michael, Nucl. Phys. B326 (1989), 544.

[26] C. Michael, Phys. Lett. B283 (1992), 103.

[27] D.H. Perkins, Introduction to High Energy Physics, Addison-Wesley, (1982)

[28] R.W.Haymaker and J.Wosiek, Phys. Rev. D43 (1991), 2676.

[29] C.W. Bernard, Phys. Rev. D9 (1974), 3312;
L. Dolan and R. Jackiw, Phys. Rev. D9 (1974), 3320.

[30] M. Creutz, Letures presented at the Symposium Workshop on Lattice Gauge Theory Using Parallel Processors, Beijing, China, 21 May - 2 June, 1987, BNL-39747.

[31] B.A. Berg, A. Billoire and R. Salvador, Phys. Rev. D37 (1988), 3774.

[32] J. Wosiek and R.W. Haymaker, Phys. Rev. D36 (1987), 3297.

[33] W.H. Press, et al., Cambridge University Press, (1986).

[34] J. Engels, F. Karsch and H. Satz, Nucl. Phys. B315 (1989), 419

[35] J. Engels, J. Fingberg and M. Weber, Nucl. Phys. B332 (1990), 737.

[36] J. Engels and V.K. Mitrjushkin, Phys. Lett. B282 (1992), 415.

[37] L.D. Debbio, et al, CERN-TH. 6282/91, IFUP-TH 37/91.

[38] J. Engels, et al, Nucl. Phys. B280 (1987), 577.

[39] Y. Peng and R.W. Haymaker, Phys. Rev. D47 (1993), 5104.

[40] G.'t Hooft, Nucl. Phys. B153 (1979), 141.

[41] R.W. Haymaker, Nucl. Phys. B (Proc. Suppl.) 17 (1990), 558.

[42] A. Hasenfratz and P. Hasenfratz, Nucl. Phys. B193 (1981), 210.

[43] F. Karsch, Nucl. Phys. B205 (1982), 285.

[44] Y. Peng and R.W. Haymaker, LSUHE No. 142-1993, submitted to Phys. Rev. D.

[45] H. Gould and J. Tobochnik, An introduction to Computer Simulation Methods, Addison-Wesley Pub. Co., (1988).

[46] S.L. Adler, Phys. Rev. D23 (1981), 2901.

[47] C. Whitmer, Phys. Rev. D29 (1984), 306.

[48] F.R. Brown and T.J. Woch, Phys. Rev. Lett. 58 (1987), 2394.

[49] M. Creutz, Phys. Rev. D36 (1987), 515.

[50] M.C. Abreu, et al. (NA38 collab.), Z. phys. C38 (1988),117;
J.Y. Grossiord, et al. (NA38 collab.), Nucl. Phys. A498 (1989), 249c;
C. Baglin, et al. (NA38 collab.), Phys. Lett. 220B (1989), 471.

APPENDIX A

MONTE CARLO METHODS IN LGT

The lattice formulation reduces the Feynman path formula for the gauge theory into a multiple ordinary integral. For a finite lattice one can evaluate the partition function in Eq. (2.20) numerically. However, the dimensionality of the multiple integral is usually very large. For example, consider a 10^4 size lattice, a size fairly typical for numerical work. Such a system has 40,000 link variables (in 4-dimensional space). This high multidimensionality of the integrals makes conventional mesh techniques for numerical calculations of integrals impractical. One must seek some other methods.

Monte Carlo simulation method is just such a technique dealing with multiple integrals with high dimensionalities, which is now the dominant method in LGT calculations. In LGT physical quantities are evaluated from the expression in Eq. (2.21), which is an average over configurations with the weight of the Boltzmann factor $e^{-S(C)}$, where C represents the configurations of the system. The basic idea of Monte Carlo method is by using some algorithm one can choose a small number of configurations which are typical of thermal equilibrium in the statistical analog, then the averages of physical quantities, such as that in Eq. (2.21), can be evaluated from the set of configurations. In the following I shall briefly review some Monte Carlo simulation methods used in LGT.

A.1 Metropolis Algorithm

Since the goal of Monte Carlo simulation is to find, in a stochastic manner, a set of configurations with a probability distribution given by the Boltzmann factor,

$$P_{eq.}(C) \approx e^{-S(C)}. \tag{A.1}$$

Let's suppose in a simulation process the system be in a configuration C, then one choose a new configuration C' as a possible update to C. C' can be taken with an arbitrary trial probability $P_{T,C}(C')$. The trial change C' may depend on the previous state C.

In Metropolis algorithm one accepts C' with the conditional probability

$$P_{acc} = min\Big[1, \frac{P_{T,C'}(C)e^{-S(C')}}{P_{T,C}(C')e^{-S(C)}}\Big]. \tag{A.2}$$

Usually $P_{T,C'}(C) = P_{T,C}(C')$. So one has

$$P_{acc} = min\Big[1, \frac{e^{-S(C')}}{e^{-S(C)}}\Big]. \tag{A.3}$$

To understand how to realize the Metropolis algorithm, let's consider a simple example, the 1-dimensional integral as shown below[45].

$$< f(x) >= \frac{\int_a^b f(x)p(x)dx}{\int_a^b p(x)dx}, \tag{A.4}$$

with ($x \in [a, b]$). This is the average of the one variable function $f(x)$ with respect to the weight function $p(x)$, as shown in Figure 20.

The Metropolis procedures used in calculating the average $< f >$ in Eq. (A.4) are given below.

(1). Choose an initial value x_1 ($x_1 \in [a, b]$) arbitrarily.

(2). Choose a trial value x_t, usually x_t is chosen from a small interval around x_1 randomly, that is, $x_t \in [x_1 - \delta, x_1 + \delta]$, where the step size δ is

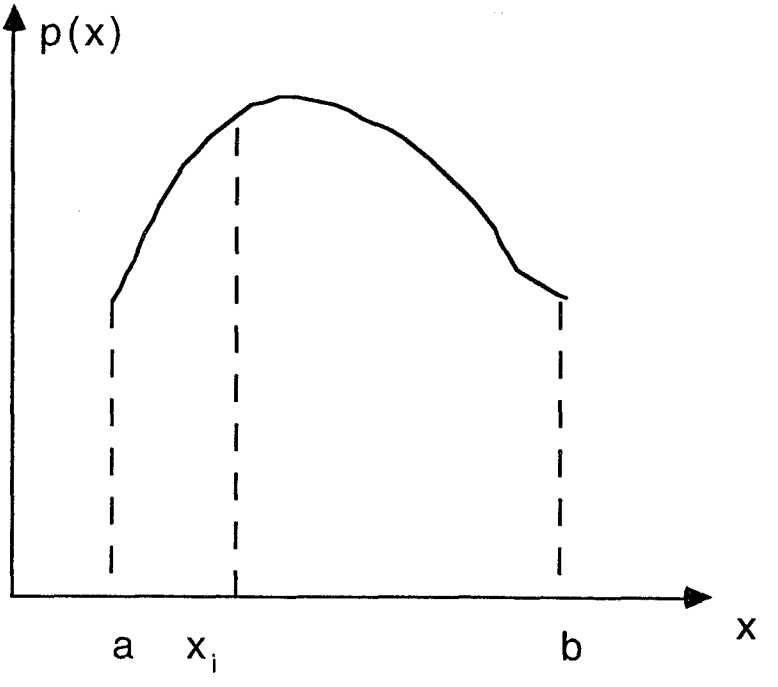

Figure 20. The weight function $p(x)$ vs. x, which is in the interval $[a, b]$. x_i is some accepted x value.

adjusted properly so that the acceptance probability of the trial value x_t is about 1/3 to 1/2.

(3). Calculate the ratio $w = p(x_t)/p(x_1)$.

if $w \geq 1$, accept the trial value x_t, that is, let $x_2 = x_t$.

if $w < 1$, call a uniform random number r in the interval $[0, 1]$.

(4). If $w < 1$, then compare w with r.

if $r < w$, accept x_t, let $x_2 = x_t$.

if $r > w$, reject x_t.

(5). Repeat steps $(2) - (4)$ many times, finally one can obtain a set of accepted x values, such as

$$\{x_1, x_2, \cdots, x_K\}.$$

where K is a large integer.

We can shown that the set of x values has the required probability distribution $p(x)$[22]. So we have the average of Eq. (A.4) can be calculated as,

$$< f(x) >= \frac{\int_a^b f(x)p(x)dx}{\int_a^b p(x)dx} = \lim_{K\to\infty} \sum_{i=1}^{K} f(x_i). \tag{A.5}$$

To apply the above procedures to the calculations in LGT, one notices that in LGT the configurations of the lattice are much more complicated than that of the above example. In LGT a particular configuration of the lattice is determined by the value of each link variable U, which is an element of the gauge group. We can denote the configuration of a lattice as $C = \{U_\mu(n)\}$, with n running through the sites of the lattice, and $\mu = 1, \cdots, 4$, the four directions of the links.

The Monte Carlo Simulation in LGT is to obtain a set of configurations, $\{C_1, C_2, \cdots, C_K\}$, with the correct Boltzmann distribution $e^{-S(U)}$, where

$S(U)$ is the action of the LGT as defined in Eq. (3.4). To obtain a new accepted configuration C_{i+1} from the old configuration C_i, one must update all link variables of the lattice, usually we call this process to be one *sweep.*

The procedures of the conventional Metropolis algorithm in LGT are given below.

(1). Updating link variable U

Suppose one need to update the link variable U, one choose a trial value,

$$U' = UH, \tag{A.6}$$

where H is a random element of the gauge group, and is chosen with a probability $P(H)$. We require that the probability for its inverse H^{-1} is the same, that is,

$$P(H) = P(H^{-1}). \tag{A.7}$$

Usually the element H is randomly selected from a table, Eq. (A.7) is insured by having the table contain the inverse of each of its elements. Eq (A.7) implies that the trial probability in Eq. (A.2) satisfies

$$P_{T,U}(U') = P_{T,U'}(U). \tag{A.8}$$

So the acceptance probability for the trial value U' is

$$P_{acc} = min[1, e^{-(S'-S)}], \tag{A.9}$$

where $S' = S(U')$ is the action with the trial value U' assigned to the link to be updated, and $S = S(U)$ is the action with the link of the old value U. This can be realized by following the analogous procedures of steps (3) and (4) of

the above example for the calculation of $< f(x) >$, that is, we can use the procedure below.

Calculate the ratio

$$w = e^{-S'}/e^{-S} = e^{-(S'-S)}. \tag{A.10}$$

If $w \geq 1$, we accept the trial value U'. If $w < 1$, we conditionally accept U' by calling a uniform random number r in the interval [0,1]; if $r < w$ we accept U', otherwise, we reject it.

(2). Updating a configuration C

To update a configuration C of the lattice, we apply the above procedures to each link of the lattice. After we finish updating one link U, we then go to update the next link until we finish updating all links of the lattice. This gives us a new accepted configuration C' of the lattice.

(3). Generate a set of configurations

If we repeat the above steps many times, we obtain a set of accepted configurations,

$$\{C_1, C_2, \cdots, C_K\}.$$

We can also show that these states satisfy the correct Boltzmann distribution $e^{-S(C)}$[22]. Therefore, the average of a physical quantity $< H >$ in Eq. (2.21) can be calculated as

$$\begin{aligned} < H > &= Z^{-1} \int (dU) H(U) e^{-S(U)} \\ &= \lim_{K \to \infty} \frac{1}{K} \sum_{i=1}^{K} H(C_i). \end{aligned} \tag{A.11}$$

A.2 Heat Bath Algorithm

This algorithm is a kind of variation of general Metropolis algorithm discussed above. In this method when one updates a link variable U, one takes the trial element U' with a probability of the Boltzmann factor,

$$P_{T,U}(U') \propto e^{-S(U')}, \tag{A.12}$$

with all other links fixed.

In this case the ratio of trial probabilities satisfies the condition,

$$\frac{P_{T,U'}(U)}{P_{T,U}(U')} = \frac{e^{-S(U)}}{e^{-S(U')}}. \tag{A.13}$$

Then according to Eq. (A.2) the acceptance probability $P_{acc.}$ of the trial element U' is just

$$P_{acc.} = 1. \tag{A.14}$$

Therefore, in the heat bath algorithm the trial change is always accepted. The procedures of this algorithm have been given by ref.[21] in details.

A.3 Over-Relaxation Algorithm

This method is also a variation of general Metropolis algorithm discussed above. The basic idea of the over-relaxation was first introduced by S.L. Adler[46] and C. Whitmer[47]. The generalization of this idea to LGT was done by F.R. Brown, et al.[48] and M. Creutz[49].

The idea of the over-relaxation method in LGT can be described as following[49].

When one updates a link variable U of the lattice, one picks a trial change U' for the link U, such that in a region of the phase space of the link

variable U the trial element U' is as far as possible from the old value U while not paying a severe energy penalty. This is done by approximately locating the locus of the minimum energy (or action) for the link variable U, and then selecting the trial element U' on the "opposite" side of the old value U, as shown in Fig. 21.

In Fig. 21 we show one locus of the minimum of the action $S(U(\omega))$ in the phase space of U, where ω is the phase factor of the link variable $U(\omega) = \exp(i\tau_j\omega_j)$ $(j = 1, 2, \cdots, n_g)$, as defined in Eq. (2.6). For simplicity we assume that all the phase factors ω_j are fixed except one of them, i.e. $\omega_k = \omega$. Then the link value to be updated can be rewriten as $U = const.\exp(i\tau_k\omega_U)$, and the action S is just a function of ω, $S = S(\omega)$. Near the minimum point $\omega = \omega_g$ the action $S(\omega)$ can be approximated by a quadratic function of $(\omega - \omega_g)$, i.e.,

$$S(\omega) \approx c_1(\omega - \omega_g)^2 + c_2(\omega - \omega_g) + c_3, \tag{A.15}$$

with c_1, c_2, c_3 the coefficients.

Suppose $\omega = \omega_U$ be the phase factor of the link value U to be updated, then one chooses the trial element U' such that its phase factor ω' is on the "opposite" side of ω_U about the minimum point $\omega = \omega_g$ of the action, that is,

$$\omega' \approx \omega_g + (\omega_g - \omega_U) = 2\omega_g - \omega_U, \tag{A.16}$$

as shown in Fig. 21.

So the trial element U' can be chosen as

$$U' = const.e^{i\tau_k\omega'} \approx const.e^{i\tau_k(2\omega_g - \omega_U)} \approx g_0U^{-1}g_0, \tag{A.17}$$

with $U^{-1} = const.\exp(-i\tau_k\omega_U)$ and $g_0 = const.\exp(i\tau_k\omega_g)$. So U^{-1} is the inverse of the old element U, g_0 is the element corresponding to the minimum of the action.

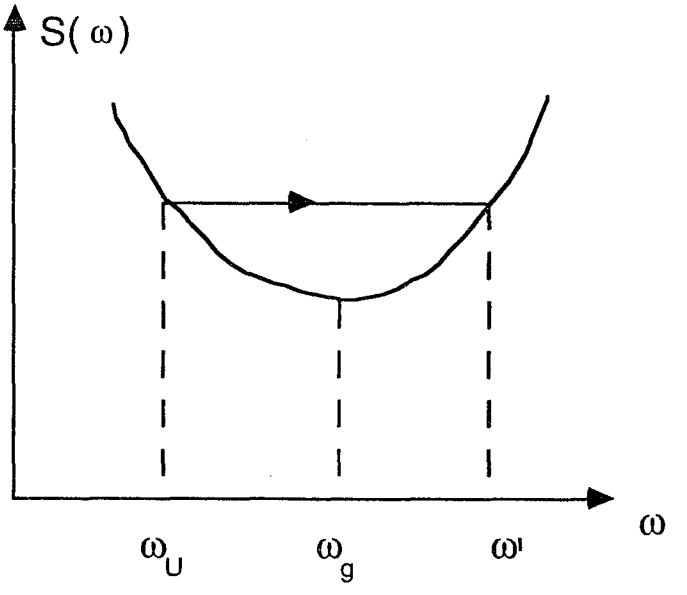

Figure 21. The locus of the minimum of the action $S(U)$ in the phase space of the link variable U. Here ω_U is the phase factor of the link value U to be updated, ω' is the phase factor of the trial value U', and ω_g is the phase factor of the element g_0 which minimizes the action S.

Now we can write down the procedures for the over-relaxation method in LGT.

(1). To update a link U, one choose an element g_0 which approximately minimize the action $S(U)$ with all other links fixed, then one constructs the trial element,

$$U' = g_0 U^{-1} g_0. \tag{A.18}$$

Then one uses the Metropolis procedures in Eq. (A.10) to decide if the trial element U' is accepted or rejected.

(2). Repeat the above step for all links of the lattice to finish one sweep. If one repeats many sweeps, one can obtain a set of accepted configurations with the correct Boltzmann distribution.

To be more specific about the selection of the element g_0, let's consider the action in Eq. (3.4). We can rewrite it in the form,

$$S(U) = S_0 - \beta/N Re[Tr(UM)], \tag{A.19}$$

where the second term contains the link U under consideration, while the first term is the remaining part of the action, M is the sum of the six staples coupling to U, as shown in Fig. 22.

A natural choise of g_0 is

$$g_0 = Proj.(M^{-1}), \tag{A.20}$$

which is the inverse of a group element obtained by projecting M onto the gauge group. In particular, for $U(1)$ and $SU(2)$ LGT, the matrix M is proportional to a group element, say g_M. Then we choose

$$g_0 = g_M^{-1}, \tag{A.21}$$

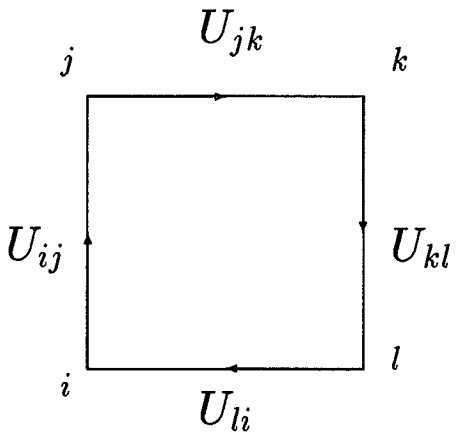

Figure 22. One 'staple' M_{jkli} that couples with the link U_{ij}, where $M_{jkli} = U_{jk}U_{kl}U_{li}$.

and the trial element $U' = g_0 U^{-1} g_0$. In this case one can easily show that

$$S(U') = S(U), \tag{A.22}$$

because of the relations,

$$Tr(U' g_M) = Tr(g_M^{-1} U^{-1} g_M^{-1} g_M) = Tr(g_M^{-1} U^{-1}), \tag{A.23}$$

and

$$Re[Tr(U g_M)] = Re[Tr(g_M^{-1} U^{-1})]. \tag{A.24}$$

Again one has that the trial probability of choosing U' equals that of choosing U, that is, $P_{T,U}(U') = P_{T,U'}(U)$, because $U = g_0 U_t^{-1} g_0$ and $U_t = g_0 U^{-1} g_0$. Therefore, from Eq. (A.2) one has the acceptance probability for the trial element U' is just

$$P_{acc.} = 1. \tag{A.25}$$

The trial change is always accepted in the over-relaxation method of $U(1)$ and $SU(2)$ LGT.

APPENDIX B

PROOF OF A RELATION

To prove Eqs. (6.32) and (6.33), we notice that Eqs. (6.24) and (6.25) implies that β_s, β_t and β, ξ are two equivalent sets of variables, that is, $F(\beta_s, \beta_t) = F(\beta_s(\beta, \xi), \beta_t(\beta, \xi))$, then we take the partial derivatives of F with respect to β and ξ respectively, one has

$$\left(\frac{\partial F}{\partial \beta}\right)_\xi = \left(\frac{\partial F}{\partial \beta_t}\right)_{\beta_s}\left(\frac{\partial \beta_t}{\partial \beta}\right)_\xi + \left(\frac{\partial F}{\partial \beta_s}\right)_{\beta_t}\left(\frac{\partial \beta_s}{\partial \beta}\right)_\xi, \tag{B.1}$$

$$\left(\frac{\partial F}{\partial \xi}\right)_\beta = \left(\frac{\partial F}{\partial \beta_t}\right)_{\beta_s}\left(\frac{\partial \beta_t}{\partial \xi}\right)_\beta + \left(\frac{\partial F}{\partial \beta_s}\right)_{\beta_t}\left(\frac{\partial \beta_s}{\partial \xi}\right)_\beta. \tag{B.2}$$

From Eqs. (6.24) and (6.25) one can get that if β is large enough ($\beta \to \infty$),

$$\begin{aligned}
\left(\frac{\partial \beta_t}{\partial \beta}\right)_{\xi=1} &= \left(\frac{\partial \beta_s}{\partial \beta}\right)_{\xi=1} = 1; \\
\left(\frac{\partial \beta_s}{\partial \xi}\right)_{\xi=1} &= -\beta + 2Nc'_s|_{\xi=1}, \\
\left(\frac{\partial \beta_t}{\partial \xi}\right)_{\xi=1} &= \beta + 2Nc'_t|_{\xi=1}.
\end{aligned} \tag{B.3}$$

where N denotes for $SU(N)$, and c' the ξ-derivative of c. Substituting Eqs. (B.3) into Eqs. (B.1) and (B.2) yields

$$\left(\frac{\partial F}{\partial \beta}\right)_{\xi=1} = \left(\frac{\partial F}{\partial \beta_t}\right)_{\xi=1} + \left(\frac{\partial F}{\partial \beta_s}\right)_{\xi=1}, \tag{B.4}$$

$$\left(\frac{\partial F}{\partial \xi}\right)_{\xi=1} = \left[\frac{\partial F}{\partial \beta_t}(\beta + 2Nc'_t) + \frac{\partial F}{\partial \beta_s}(-\beta + 2Nc'_s)\right]_{\xi=1}. \tag{B.5}$$

F. Karsch has studied the coefficients c_s and c_t[43]. His results show that the derivatives $c_s'|_{\xi=1}$, $c_t'|_{\xi=1}$ vanish for sufficient large lattice coupling β. For example, as $\beta \geq 2.2$, the values of $c_s'|_{\xi=1}$ and $c_t'|_{\xi=1}$ of $SU(2)$ LGT are about 0.1, which is much less than the values of β. So in the case of large β Eqs. (B.4) and (B.5) become

$$\left(\frac{\partial F}{\partial \beta}\right)_{\xi=1} = \left(\frac{\partial F}{\partial \beta_t}\right)_{\xi=1} + \left(\frac{\partial F}{\partial \beta_s}\right)_{\xi=1}, \tag{B.6}$$

$$\left(\frac{\partial F}{\partial \xi}\right)_{\xi=1} = \beta\left(\frac{\partial F}{\partial \beta_t}\right)_{\xi=1} - \beta\left(\frac{\partial F}{\partial \beta_s}\right)_{\xi=1}. \tag{B.7}$$

After carrying out some simple algebra, we can obtain Eqs. (6.32) and (6.33).

VITA

The author was born in Augest 22, 1964 in Chongqing, China. He attended Nankai Middle School in Chongqing, then did undergraduate work in Physics at Tsinghua University, Beijing, China, and got a BS degree there in 1986. He came to Louisiana State University in Fall, 1986, and got his MS degree in Physics in 1987. He then joined the Lattice Gauge Theory group of Professor Haymaker to work for his PhD in 1988.

DOCTORAL EXAMINATION AND DISSERTATION REPORT

Candidate: Yingcai Peng

Major Field: Physics

Title of Dissertation: Phase Transitions and Flux Distributions of SU(2) Lattice Gauge Theory

Approved:

Richard Hazard
Major Professor and Chairman

Daniel Fogel
Dean of the Graduate School

EXAMINING COMMITTEE:

Joseph Callaway

Lai-Him Chan

Detlev Koester

[illegible]

Rajiv K. Kalia

Tessa E. Conner

Date of Examination:

April 6, 1993